NASA/TM—2016-219136

Materials Characterization of Electron Beam Melted Ti-6Al-4V

Susan L. Draper, Bradley A. Lerch, and Jack Telesman
Glenn Research Center, Cleveland, Ohio

Richard E. Martin
Cleveland State University, Cleveland, Ohio

Ivan E. Locci and Anita Garg
University of Toledo, Toledo, Ohio

Andrew J. Ring
Ohio Aerospace Institute, Brook Park, Ohio

September 2016

NASA STI Program . . . in Profile

Since its founding, NASA has been dedicated to the advancement of aeronautics and space science. The NASA Scientific and Technical Information (STI) Program plays a key part in helping NASA maintain this important role.

The NASA STI Program operates under the auspices of the Agency Chief Information Officer. It collects, organizes, provides for archiving, and disseminates NASA's STI. The NASA STI Program provides access to the NASA Technical Report Server—Registered (NTRS Reg) and NASA Technical Report Server—Public (NTRS) thus providing one of the largest collections of aeronautical and space science STI in the world. Results are published in both non-NASA channels and by NASA in the NASA STI Report Series, which includes the following report types:

- TECHNICAL PUBLICATION. Reports of completed research or a major significant phase of research that present the results of NASA programs and include extensive data or theoretical analysis. Includes compilations of significant scientific and technical data and information deemed to be of continuing reference value. NASA counter-part of peer-reviewed formal professional papers, but has less stringent limitations on manuscript length and extent of graphic presentations.

- TECHNICAL MEMORANDUM. Scientific and technical findings that are preliminary or of specialized interest, e.g., "quick-release" reports, working papers, and bibliographies that contain minimal annotation. Does not contain extensive analysis.

- CONTRACTOR REPORT. Scientific and technical findings by NASA-sponsored contractors and grantees.

- CONFERENCE PUBLICATION. Collected papers from scientific and technical conferences, symposia, seminars, or other meetings sponsored or co-sponsored by NASA.

- SPECIAL PUBLICATION. Scientific, technical, or historical information from NASA programs, projects, and missions, often concerned with subjects having substantial public interest.

- TECHNICAL TRANSLATION. English-language translations of foreign scientific and technical material pertinent to NASA's mission.

For more information about the NASA STI program, see the following:

- Access the NASA STI program home page at http://www.sti.nasa.gov

- E-mail your question to help@sti.nasa.gov

- Fax your question to the NASA STI Information Desk at 757-864-6500

- Telephone the NASA STI Information Desk at 757-864-9658

- Write to:
  NASA STI Program
  Mail Stop 148
  NASA Langley Research Center
  Hampton, VA 23681-2199

NASA/TM—2016-219136

Materials Characterization of Electron Beam Melted Ti-6Al-4V

Susan L. Draper, Bradley A. Lerch, and Jack Telesman
Glenn Research Center, Cleveland, Ohio

Richard E. Martin
Cleveland State University, Cleveland, Ohio

Ivan E. Locci and Anita Garg
University of Toledo, Toledo, Ohio

Andrew J. Ring
Ohio Aerospace Institute, Brook Park, Ohio

National Aeronautics and
Space Administration

Glenn Research Center
Cleveland, Ohio 44135

September 2016

Level of Review: This material has been technically reviewed by technical management.

Available from

NASA STI Program
Mail Stop 148
NASA Langley Research Center
Hampton, VA 23681-2199

National Technical Information Service
5285 Port Royal Road
Springfield, VA 22161
703-605-6000

This report is available in electronic form at http://www.sti.nasa.gov/ and http://ntrs.nasa.gov/

Materials Characterization of Electron Beam Melted Ti-6Al-4V

Susan L. Draper, Bradley A. Lerch, and Jack Telesman
National Aeronautics and Space Administration
Glenn Research Center
Cleveland, Ohio 44135

Richard E. Martin
Cleveland State University
Cleveland, Ohio 44115

Ivan E. Locci and Anita Garg
University of Toledo
Toledo, Ohio 43606

Andrew J. Ring
Ohio Aerospace Institute
Brook Park, Ohio 44142

Abstract

An in-depth material characterization of Electron Beam Melted (EBM) Ti-6Al-4V material has been completed on samples fabricated on an ARCAM A2X EBM machine. The specimens were fabricated under eight separate builds with the material divided into two lots for material testing purposes. Hot Isostatic Pressing (HIP) was utilized to close porosity from fabrication and also served as a material heat treatment to obtain the desired microstructure. The changes in the microstructure and chemistry from the powder to pre-HIP and post-HIP material have been analyzed. Several nondestructive evaluation (NDE) techniques were utilized to characterize the samples both before and after HIP. The test matrix included tensile, high cycle fatigue, low cycle fatigue, fracture toughness, and fatigue crack growth at cryogenic, room, and elevated temperatures. The mechanical properties of the EBM Ti-6Al-4V are compared to conventional Ti-6Al-4V in the annealed condition. Fractography was performed to determine failure initiation site. The EBM Ti-6Al-4V had similar or superior mechanical properties compared to conventionally manufactured Ti-6Al-4V.

Introduction

In cooperation with the United States Air Force (USAF) to advance technologies for in-space propulsion systems, NASA Glenn Research Center has generated a material database for EBM Ti-6Al-4V. Ti-6Al-4V is a widely used titanium alloy in the aeronautic and aerospace industries due to its combination of low weight, high strength, and corrosion resistance (Refs. 1 and 2). While Ti-6Al-4V has been manufactured by electron beam melting for a number of years (Refs. 3 and 5), a complete set of microstructure and corresponding mechanical properties from cryogenic to elevated temperatures is needed to provide data for component design. The ultimate goal is to use additive manufacturing (AM) to produce a Ti-6Al-4V gimbal cone for the RL10 rocket engine. Additive manufacturing enables a reduction in component ordering lead-time and a reduction in cost compared to the currently forged and machined Al alloy component as additive manufacturing allows for direct manufacture from powder with little machining required.

Electron beam melting (EBM) was selected as the additive manufacturing technique. EBM has the advantages of operating in a vacuum to reduce oxygen pick-up and reduced residual stresses due to fabrication performed at powder-bed temperatures above the α' martensitic transformation temperature of

575 °C (Refs. 6 and 7). Both EBM and SLM enable near-net or net shape production, high material yield, and increased part complexity with reduced machining. The main disadvantage to EBM, compared to selective laser melting (SLM), is the typically rougher final part finish. The material property database generated under this study was on machined, smooth samples. The effect of as-fabricated surface finish on material properties was not investigated, but it is expected it to have a detrimental effect on properties, particularly fatigue.

Material and Test Procedure

Metallographic and mechanical test samples were procured from the Department of Energy's Kansas City Plant at the National Secure Manufacturing Center (NSMC). The specimens were fabricated by an Arcam A2X EBM machine under eight separate builds with the material divided into two lots for material testing purposes. This machine has been dedicated to Ti-6Al-4V and no other composition has ever been in the chamber. Arcam AB supplied all Ti-6Al-4V powder used in the fabrication of parts. Samples were fabricated oversized to allow for machining. The samples were fabricated using EBM Control Software Version 3.2.132 using the standard Arcam Ti6Al4V 50 μm Theme Version 3.2.121 (Ref. 4). Specimen cubes and cylindrical bars were fabricated vertically with the stress axis parallel to the build direction for the majority of the specimens. A small build of horizontal, cylindrical samples was also fabricated to check for build orientation effects. The cylindrical bars utilized for tensile, low cycle fatigue, and high cycle fatigue testing had a 15.2 mm diameter and were 104 mm long. The fracture toughness and fatigue crack growth specimens had dimensions of 34.3 by 33 by 12 mm and 34.3 by 33 by 5.7 mm, respectively. The layouts of builds 1 through 4 are shown in Figures 1 to 5. Builds 1_1, 1_2, and 4, fabricating the tensile/fatigue bars, were scanned in quadrants, halves, or sections in order to eliminate an Arcam error called "smoking the gun". Dividing the build into quadrants or sections resolved the issue as the beam scanned a smaller area and then moved to the next section. Build 2, after removal from the Arcam, is shown in Figure 5.

A powder sample was taken from the Arcam chamber after every build to analyze the variation in chemistry from build to build and compared to Arcam powder certification for that particular powder lot. Metal analysis was performed by inductively coupled plasma—atom emission spectroscopy on the powder, as-built samples and after HIP samples. Carbon analysis was done by combustion–extraction technique, using induction furnace and carbon detection as CO_2 by an infrared cell. Nitrogen and oxygen contents were measured by inert gas fusion. Powder size was measured on loose powder as well as polished powder cross sections. Powder size and microstructural feature measurements are given with error bars representing 95 percent confidence intervals.

Two samples were examined in the as-fabricated condition but all mechanical test samples were hot isostatically pressed (HIP) to close internal porosity. The 99.998 percent pure Argon was used to minimize oxidation of parts during HIP. All mechanical test specimens were machined to final dimensions with 1.6 μm surface finish and were not tested with the EBM surface finish in-place.

Nondestructive evaluation (NDE) techniques were used to characterize as manufactured samples before and after HIP as well as in the final machined state. In particular, micro-focus computed tomography (CT) was utilized for internal examination of the samples and fluorescent penetrant inspection to identify any surface indications present in the final machined samples. CT was also used to examine any potential indications at the subsequent fracture locations. Since penetrant inspection did not reveal any significant indications, discussion will focus on the CT inspection. CT data was collected and processed using a commercially available system manufactured by North Star Industries. The system utilizes a microfocus x-ray source (XWT-225-SE, X-RAY Worx GmbH) and a flat panel digital x-ray detector (Dexela 2923, PerkinElmer, Inc.) for acquiring the radiographs (Fig. 6(a)). Test samples were mounted in a fixture to allow scanning of 6 samples at a time (Fig. 6(b)). The fixture was mounted on a rotating stage with a source to object distance of 160 mm and a source to detector distance of 760 mm to provide a magnification factor of approximately 4.6. In order to improve resolution, data collection was confined to the reduced gauge section of the tensile samples. Inspection was conducted by collecting

radiographs every 0.2° through a 360° rotation. The acquired radiographs are then processed using a back projection algorithm to produce volumetric CT data with a voxel resolution of approximately 16.5 μm. Image analysis of the CT data sets was performed by examination of the cross-section slices generated.

As-fabricated and HIP'd samples were sectioned for metallographic analysis at the bottom, middle, and top section of the builds. Samples were examined optically and with a scanning electron microscope (SEM) in the as-polished condition and after immersion etching with Kroll's Reagent. Transmission electron microscope (TEM) was also performed on a HIP'd sample. Pole figures were generated on samples built parallel and transverse to the test direction to determine sample texture. After testing, samples were sectioned and their fracture surfaces were examined both optically and in the SEM to determine fracture initiation sites.

Tensile tests were conducted in strain control using a strain rate of 1×10^{-4} s^{-1} at –196, –101, 20, and 149 °C. If strain exceeded 20 percent, the sample was unloaded to zero load and then loaded to failure in stroke control at an equivalent strain rate. Dynamic modulus was run at room temperature using ASTM Standard E1876-07—"Standard Test Method for Dynamic Young's Modulus, Shear Modulus, and Poisson's Ratio by Impulse Excitation of Vibration".

High Cycle Fatigue (HCF) tests were conducted in load control at a frequency of 20 Hz. Tests were run using a sinusoidal waveform at several load ratios, R_σ, of –1, 0.1, and 0.5. Test temperatures were –196, 20, and 149 °C. Note that the test frequency at –196 °C was 30 Hz. Ten million cycles was the runout value for the long-term tests. A few runout samples were additionally loaded at higher stresses to produce failure. Low Cycle Fatigue (LCF) test were performed in fully reversed ($R_\varepsilon = -1$), strain control using a triangular waveform. Tests were run between total strain limits at a cyclic frequency of 0.5 Hz. The same three test temperatures were used. The crack origin(s) on every sample was identified using optical microscopy and for most samples SEM.

Fracture toughness testing was performed in accordance with ASTM E1820, to determine K_{IC} or J_{IC} as appropriate. CT specimen geometry with width parameter W = 2.54 cm and thickness b = 0.95 cm was used. Knife-edges for crack mouth opening displacement (CMOD) gage were integral with the notch geometry, in line with the loading axis. The notch was placed on the top surface of the cube with the notch parallel to the build direction. Testing was performed on an MTS servohydraulic 44.5 kN capacity load frame. Precracking crack length was monitored by Direct Current Potential Difference (DCPD) and fracture crack length by compliance using Fracture Tech Associates' (FTA) fatigue crack growth and fracture toughness test software, respectively. Specimen sides were polished to aid in optical measurement of crack progression. A fatigue precrack was induced in each specimen at a constant maximum stress intensity of 17.6 MPa√m and a load ratio of R = 0.1. Fatigue precracks were grown to a total crack length of approximately 1.2 cm. After precracking, EDM was used to machine side grooves into each specimen giving a net 20 percent reduction in thickness. Specimens were tested in displacement control, using a series of unloading slopes throughout the test to determine crack length from compliance and develop a resistance curve. After testing, each specimen was heat tinted at 315 °C for 1 hr to mark the final crack length before fracturing specimens completely and measuring through-thickness crack lengths on a travelling microscope. Data analysis was performed using FTA's Non-Linear Fracture Toughness (NLFT) Analysis software.

Fatigue crack growth rate testing was performed in accordance with ASTM E647. Compact tension (CT) geometry specimens with a width parameter W = 2.54 cm were used, sharing similar dimensions to the fracture toughness specimens for ease of test setup. The notch was placed on the top surface of the cube with the notch parallel to the build direction. CT specimen thickness was 0.318 cm. Testing was performed using MTS servohydraulic 44.5 and 89 kN capacity load frames. Specimen sides were polished to aid in optical measurement of crack progression. A fatigue precrack was induced in each specimen at a relatively low stress intensity, typically at K_{max} = 7.6 MPa √m and a load ratio of R = 0.1. Fatigue precracks were grown to a total crack length of approximately 0.66 cm. After precracking, specimens were heat tinted at 315 °C for 1 hr while being held at mean load. Each specimen was removed and crack length measured optically on a travelling microscope. Specimens were reinstalled in the loading clevis and tested in K-control at various loading conditions. Testing was performed with load ratios of R = 0.1,

0.5, and 0.7. Positive K-gradients up to 0.138 mm^{-1} were used for the characterization of the Paris regime, and a K-gradient of –0.08 mm^{-1} was used for threshold tests. Testing was performed at temperatures of 20 and 149 °C. Cryogenic –196 °C testing was completed by Metcut Research Inc. Specimens were fractured after test completion and optical measurements of precrack and crack lengths were taken with a travelling microscope. Data processing was performed using FTA's Fatigue Crack Growth Rate (FCGR) Analysis software. Linear corrections were made to adjust direct current potential drop crack length measurements to optical measurements. Data points were filtered down to provide a data point for every 0.010 cm of crack growth.

Thermal diffusivity (α) was measured using the laser flash technique (ASTM E1461). The thermal diffusivity and specific heat samples were first measured from room temperature to –150 °C and then measured from room temperature to 150 °C. The two results were combined to create the final thermal diffusivity curve. The below room temperature measurements were first measured in air. Then the measurement chamber was placed under a vacuum and back filled with helium. The sample was measured at room temperature in the helium environment and the difference applied to the lower temperatures. The above room temperature measurements were all measured in air with no changes during the measurements. The results were not corrected for changes in thickness with respect to temperature.

Bulk density (ρ) values were calculated from the sample's geometry and mass. Specific heat (C_p) was measured using differential scanning calorimeters. Thermal conductivity (λ) values were calculated as a product of these quantities, i.e., $\lambda = \alpha \bullet C_p \bullet \rho$. A dual push-rod dilatometer was used to measure linear thermal expansion following ASTM standard E228. The samples were first measured from room temperature to –150 °C and then measured from room temperature to 150 °C. Both tests were conducted in a dual push-rod dilatometer with sapphire used as the standard. The measurements were performed in a helium environment with a heating rate of 1.5 °C per minute.

Results

Chemistry

Chemical composition of powder taken from the Arcam machine after every build was analyzed as well as the chemistry of an as-built and after hot isostatic press sample. Powder was added to the EBM machine as needed and blended with remaining powder. The results are given in Tables I and II and compared to the Arcam certification of the supplied powder and also the ASTM specification for a Ti-6Al-4V sample fabricated by a powder fusion method (ASTM F2924). The oxygen content of the powder was above the ASTM standard limit even though the Arcam certification of the powder was well within the oxygen limits. Ti-6Al-4V powder is recycled in the Arcam system; however, Arcam has determined that oxygen pick-up is not due to the storage or recycling of powder but due to the presence of water vapor in the EBM chamber (Ref. 8). Arcam has recommended practices for minimizing the oxygen pick-up during a build. The oxygen level from the powder to the as-fabricated sample was maintained and was not increased significantly due to HIP. All other elements were within the specification range. However, various inclusions were found at fracture initiation sites that were not detected by chemical analysis. The volume fractions of these elements were low and were absent in the powder sample used for chemical analysis.

Nondestructive Evaluation (NDE)

Fluorescent penetrant inspection (FPI) was performed on all of the tensile and fatigue samples. The only FPI indications were in the shank areas, which would not affect the test results. Therefore, none of the samples were rejected based on FPI. Figure 7 shows an example of CT results for a test sample in the as manufactured condition and following HIP. In the as-manufactured state, the sample contained a population of porosity that was readily detected. Following HIP, CT was able to confirm closure of the

porosity. The sample also contained a high density indication that remained following the HIP process. High-density indications were scattered throughout the samples with nearly every sample having at least one indication. Several high cycle fatigue samples initiated failure at inclusions that corresponded to these high density indications. The volume fraction of inclusions was estimated at 0.04 percent.

Microstructure

Ti-6Al-4 V is classified as an α-β alloy. The α is a hexagonal-close-packed (hcp) crystal structure up to 980 °C, above which it transforms to β, a body-centered-cubic (bcc) crystal structure. The processing and heat treatment of the alloy determines the α/β microstructure and the resulting mechanical properties of the alloy. During cool down from the melt in the EBM machine, α phase first nucleates at prior β grain boundaries and then develops into Widmanstätten laths and lamellar colonies.

Powder samples were examined in the SEM and an example is shown in Figure 8. The powders' surfaces were fairly smooth and uniform in size. Powder size distribution was measured on loose powder samples from builds 1_1 and 1_2 representing lot 1 powder and builds 5 and 6 representing lot 2 powder. Powder size averaged 60±3 μm for lot 1 powder and 59±2 μm for lot 2 powders with the range in powder size from 17 to 122 μm. Error bands represent 95 percent confidence intervals. The microstructure of the powder was examined on powder mounted in epoxy and polished. Pores were observed internal to the powder particles as shown in Figure 8(b). The pores are most likely a result of Argon entrapped in the powder during powder processing. The average pore diameter was 21.4±5.7 μm and ranged from 6 to 59 μm for powder from build 1_2. Build 6 powder had pores averaging 18.9±3.5 μm, with a range from 4 to 49 μm. The microstructure of the as-received powder is shown in Figure 8(c).

Optical images of EBM samples revealed porosity in the as-fabricated condition. Porosity was also observed in NDE images. Pores have been known to originate from entrapped argon inside the powder particles from the manufacturing process (Refs. 9 and 10). The porosity was present in all sections of the samples, top, gage, and bottom, an example of which is shown in Figure 9(a). The porosity averaged 33±4 μm and ranged from 7 to 106 μm, larger than the porosity observed in the powder samples. This may indicate a coalescence of the entrapped Ar during fabrication or may be due to the larger number of pores measured in fabricated samples. After etching with Kroll's Reagent, the fine grain α/β lamellar microstructure became visible, shown in Figure 9(b). The microstructure is predominantly α phase (light in optical images and dark in scanning electron microscope (SEM) images). The lamellar structure is not well defined in the as-fabricated condition. Columnar prior—β grains grew during fabrication in the z-direction, perpendicular to the build plane, Figure 9(c).

The hot isostatic pressure (HIP) temperature used for the EBM samples was below the β transus temperature for Ti-6Al-4V. The microstructure coarsened slightly during HIP and the microstructure was more defined, Figure 10. The microstructure is made up of columnar prior β grains with a transformed α + β microstructure. The columnar microstructure is best observed in optical micrographs of longitudinal, etched samples, Figure 11. The EBM processing theme utilized 50 μm thick layers. The build layers are not visible in the microstructure but the prior β grains extend beyond several build layers. Transmission electron microscopy was utilized to verify the presence of the α and β phases and determine their orientation relationship, Figure 12. In this area, the microstructure was a lamellar α/β with the [1010]α parallel to [111]β and {0001} α parallel to {110} β, the same orientation relationship as conventionally manufactured Ti-6Al-4V.

The microstructural features important to mechanical properties for Ti-6Al-4V are prior beta grain size, colony size, and lath thickness. There were no primary α grains present in the EBM microstructure. The prior β grain size, outlined with α phase, in the transverse direction averaged 82±9 μm for a lot 1 sample and a similar 91±11 μm for a lot 2 sample. The prior beta grain extends in the z or build direction but was not defined enough to enable a measurement. A typical Ti-6Al-4V lamellar microstructure has uniform colonies with all the α/β lathes going in the same direction. The EBM microstructure had the orientation of the lathes changing frequently, often within a few lathes.

Five random orientation lines were drawn on five micrographs from each sample and the average line length of the distance with similarly orientated lathes is given as the colony size in Table III. The colony size was not significantly different for lot 1 and 2 samples but did change slightly depending on location within the sample. The colony size was similar at the bottom and gage section of the samples but was smaller at the top of the build, Table III. The horizontal samples had a significantly larger colony size compared to the vertical samples. The alpha lamellar thickness was measured on a minimum of five micrographs for each sample. The lot 1 and 2 samples had consistent lath thickness with averages ranging from 1.7 to 1.9 μm. The horizontal samples had a significantly larger alpha lath thickness, averaging 2.8±0.2 μm. The electron beam would have significantly longer continuous scans for the horizontal samples compared to the vertical samples, which may have affected the cooling rate. The cooling rate is the most critical parameter in determining the width of the α-lamellae in the lamellar structure and the extent of the α-layer at β grain boundaries (Ref. 11). A slower cooling rate for the horizontal samples could have caused the larger colony size and lath thickness.

X-ray diffraction was used to determine the presence of texture in the samples. Pole figures, shown in Figure 13(a) for a lot 1 sample, show a fiber texture with hexagonal base planes of the α phase orientated perpendicular to the growth direction. Lot 2 samples had no preferred orientation as shown in Figure 13(b). The horizontal samples had coexisting (100), (002), and (101) α – fiber texture with all 3 fiber axes parallel to the build direction (Fig. 14). A fiber texture has rotational symmetry about the EBM beam axis. The only known difference in the fabrication of lot 1 and lot 2 samples was in how the builds were sectioned, Figures 1 and 4. Lot 1 was fabricated in quadrants with a quadrant having generally a 5 by 4 or 4 by 5 array of samples. Lot 2 was built in sections with each section having an array of 3 by 3 samples. Each quadrant or section was built before moving to the next one.

Tensile

The dynamic moduli were measured to be E = 118 GPa, G = 45.7 GPa, and ν = 0.29. These samples were built in the z direction and therefore Young's modulus, E_Z, is also taken in the z direction.

Multiple tensile samples were run at each temperature and build configuration. Results for samples tested at room temperature are shown in Figure 15. Builds from lot 1 and 2, as well as samples from the horizontal build, are shown. Within a given lot, good reproducibility of tensile properties was obtained. The elastic modulus, 0.2 percent offset yield strength (YS) and ultimate tensile strength (UTS) were higher for lot 1 samples than lot 2 samples; however, the failure strain and reduction of area (RA) were generally equal between lots 1 and 2 with the exception of one lot 2 sample tested at room temperature that failed at an inclusion. The horizontal samples (indicated with an 'H') had a similar strength to lot 2 samples but had lower ductility, averaging 13.4 percent failure strain. Tensile properties are given in Table IV.

MMPDS-07 (Ref. 2) cites A-basis values for annealed extrusions of Ti-6Al-4V as having an UTS of 896 MPa and failure strains of 10 percent. All of the AM samples exceeded these values with the exception of the one RT sample that failed at an inclusion. Note that values for conventionally cast Ti-6-4 (which may be more applicable to the AM material since both processes melt and solidify the alloy) are even lower than for the extruded material. The ductility of the EBM material was above the A-basis values for annealed extrusions even with oxygen levels above the ASTM limit.

The effect of temperature on tensile properties is shown in Figures 16 and 17. The horizontal samples were only tested at room temperature. As the temperature increased, the YS and UTS decreased and the ductility increased. Even at –196 °C, the failure strain was nearly 10 percent and the fracture surfaces exhibited ductility as shown in Figure 18. The difference in strength between lot 1 and 2 samples was consistent over the entire temperature range. The strain to failure exceeded 20 percent from 20 to 149 °C for the vertical samples, with the exception of one RT sample (186). Tensile properties are shown in Table IV for all temperatures and samples. Figure 17 depicts the failure strain and RA as a function of temperature and lot, where the error bars equal ± one standard deviation. The increasing ductility as a

function of temperature can be observed on the fracture surfaces. Tensile failures initiated both at the surface and internally. The horizontal samples had a texture to the fracture surface, Figure 18(c).

Tensile fracture surfaces with inclusions are shown in Figure 19. Sample 65, tested at RT, failed at a Si inclusion; however, the tensile properties of sample 65 were not affected. Sample 115, also tested at RT, had an Nb inclusion on the fracture surface, but the Nb inclusion was not the fracture initiation site. Sample 186, mentioned above, was the only sample in which the tensile properties were affected by an inclusion. Sample 186 from lot 2 failed at 9.8 percent, well below the average of 20.8 percent for other vertical RT samples. A low-density inclusion, on the order of 40 μm long, initiated failure, Figure 19(c). Energy dispersive spectroscopy (EDS) analysis shows the inclusion contained Si, Al, O, and Ca. Sample 78 had a W particle on the fracture surface but not at the initiation site. The W could be coming off of the electron beam filament during melting.

The high strength of the EBM material is likely due to its refined lamellar microstructure with colony sizes on the order of 10 μm compared to 20 to 500 μm for conventionally manufactured lamellar microstructures (Refs. 12 and 13). The difference in strength between lots 1 and 2 could not be explained by the microstructure. The various microstructural features were examined and measured without a significant difference being detected between the two lots of material, Table III. The difference in strength between lots 1 and 2 can only be explained by the difference in texture. The (002) fiber texture has been shown to increase the strength of Ti-6Al-4V (Refs. 1, 14, and 15). The samples were fabricated within days of each other using the same build parameters; however, the builds were sectioned slightly differently. Lot 1 samples were built in quadrants and halves (Fig. 1), with arrays of 4 by 5 samples fabricated per quadrant/half, whereas lot 2 was fabricated in sections with arrays of 3 by 3 samples in each section (Fig. 4). Lot 1 thus had a longer scan length per section compared to lot 2. Arcam has studied the effect of array size on tensile strength and found no difference in tensile strength between samples built in a 3 by 3 compared to a 5 by 5 array (Ref. 4). It is not clear why lot 1 had a fiber texture and lot 2 had a random texture. The fracture surfaces were also examined and with the exception of sample 186, nothing was observed to affect the tensile properties. The difference in strength for the horizontal samples could be explained by the larger colony size and alpha lath thickness. Slip length is effectively controlled by the colony size. Larger colonies allow for longer slip and slightly lower strengths. Additionally, the alpha phase present at the prior beta grain boundaries was perpendicular to the tensile axis. The orientation of the alpha phase could be causing both the lower ductility and the observed texture on the fracture surfaces.

High Cycle Fatigue

The HCF results are shown in Tables V to VII for temperatures of 20, 149, and –196 °C, respectively and are grouped in the table by load ratio. Included in the tables is the lot number. Note that the ‘H’ indicates samples taken from a horizontal build. The location of the crack origin is listed in the last column.

The data are plotted in the next several figures. In Figures 20 to 23 the results at 20 °C are plotted as maximum stress, σ_{max}, versus fatigue life, N_f. Figure 20 displays the data for the fully-reversed case ($R_\sigma = -1$). Only samples from lot 1 were tested under these conditions. Four of these tests were runouts having reached at least ten million cycles. The remaining samples represent specimen failures (complete separation). The sample numbers are plotted to the left of the symbols for easy reference. All of these samples initiated at the surface with the exception of sample 114 which initiated internally, 1280 μm from the sample surface. This sample was previously runout at a load ratio of 0.5 and a maximum stress of 716 MPa. Similarly, sample 4 was first runout at a stress of 483 MPa and then boosted to a maximum stress of 635 MPa and run until failure at 39,108 cycles. Two of the samples, 27 and 58, both failed at 100 μm diameter Nb-inclusions at the surface. The observation of Nb and other types of inclusions found at HCF initiation sites is discussed later in the paper. With the exception of samples 58 and 84, all of the other tests would appear to fall on a smooth curve with an asymptote (fatigue limit) at 550 MPa.

For a load ratio of 0.1 the data are plotted in Figure 21 and again only lot 1 samples were run under this condition. Two samples achieved the ten million-cycle limit, all others failed. Most of the samples lie on a smooth curve with an apparent fatigue limit of approximately 600 MPa. Two of the samples (21 and 121) had smaller lives and both had Nb inclusions at their surface initiation site. The remainder of the samples all failed at internal initiations.

Test results for the highest mean stress ($R_\sigma = 0.5$) are shown in Figure 22. Tested under this set of conditions were lots 1, 2 and three samples taken from the horizontal build direction (H). Four of the tests were runouts, three from lot 1 and one sample from H. Samples from the horizontal build had the longest lives. Samples from lot 2 exhibit the shortest lives and those from lot 1 fell in between. It appears that the fatigue limit is about 700 MPa for lot 1 and 650 MPa for lot 2, which is consistent with the slightly smaller UTS for lot 2 samples. Four of the samples (39, 60, 184, and 202) had much shorter lives than the main grouping and these samples had initiations sites on the surface of the samples. All others failed from internal initiation sites. Of those failing from internal initiation sites, samples 63, 72, H12, 133 and 145, have completely contained internal cracks and tend to fail at higher lives. This means that the fatigue crack never broke the plane of the gauge surface until tensile overload occurred.

A summary of the results from 20 °C is given in Figure 23. Also plotted in this figure are HCF data on conventionally manufactured, annealed Ti-6-4 samples tested at NASA for an ASTM E466 round robin. These samples were also conducted at 20 Hz and in the same test rig. They are shown by filled, black circles in the figure. Additionally, there are three curves that were taken from MMPDS-07 (Ref. 2) for annealed Ti-6-4 at three equivalent mean stresses (0, 324, and 483 MPa). These mean stresses are similar to those used with the additive manufactured material.[1] These samples were machined from a 32 mm diameter bar and tested at 30 Hz. The UTS for this material was 945 MPa and is 100 MPa lower than the lowest value exhibited by the AM material. The lines in Figure 23 were reconstructed from the best-fit equations based on equivalent stresses in the MMPDS chapter on Ti-6-4. Data for the three load ratios ($R_\sigma = -1$, 0.1, and 0.5) are plotted with specific colors; black for R = –1, orange for 0.1, and green for 0.5. It is shown that the additive manufactured samples are superior to both the ASTM and MMPDS data. The exception is for the one AM sample (58) that failed at a Nb-inclusion, and even that sample is well within the scatter from the MMPDS data. The MMPDS, R = –1, fit does not quite represent the fatigue limit for that material properly and examination of the original data suggest that the limit is at approximately 350 MPa, significantly lower than that exhibited (550 MPa) by the AM material. This is understandable since the UTS for the lot 1 material is 1130 MPa and for the MMPDS is only 945 MPa. While the ASTM data are scarce at the high life regime, it appears that their limit is ≤400 MPa, again less than that experienced by the AM material.

At R = 0.1 the AM data lie completely above the fit line from MMPDS. The fatigue limits from both are similar, but the AM has much longer lives (as much as two orders of magnitude at intermediate lives) for the same maximum stresses. Even the two samples (21 and 121) that failed prematurely from Nb-inclusions had longer lives than those taken from MMPDS.

Finally, at a load ratio of 0.5, the AM samples show equivalent or better lives than the MMPDS fit, especially at higher stresses. The fatigue limits for the AM samples are similar to those from MMPDS or perhaps even a bit (6 percent) lower for lot 2 and the horizontal build. However, the data are sparse in this regime. At the higher stress levels (>700 MPa) the data from R = 0.1 and 0.5 are very similar indicating a smaller influence of mean stress on life.

At test temperatures of 149 °C (Table VI) samples from lots 1 and 2 were tested. A fewer number of tests were conducted compared to the 20 °C test temperature. All data are plotted in Figure 24 and exhibit the typical maximum stress-life ranking as a function of mean stress. The data again indicate that at similar stresses those samples from lot 1 have a slightly longer life than those from lot 2. There are four samples, all from lot 2, that are runouts. These points imply fatigue limits of 400, 550, and 650 MPa for

[1]The tests from MMPDS were conducted using a constant mean stress, not a constant load ratio as was done with both the AM and ASTM E466 samples.

the load ratios of –1, 0.1 and 0.5, respectively. From the limited data, the fatigue limits at 149 °C are equal to those at 20 °C at R = 0.5, and lower at the other two load ratios.

It appears that those samples that initiated at internal sites had longer lives than those initiating on the surface of the sample. Although there is not a one-to-one comparison to depict this, samples 36 and 57 do show this trend in Figure 24. Sample 57 (initiated internally) had a life of 1.7 million cycles at a maximum stress of 620 MPa, whereas at a lower stress of 550 MPa sample 36 (surface initiation) had a shorter life of 0.5 million cycles. Furthermore, two of the samples tested at R = 0.5 (1 and 76) initiated internally at defects which did not appear to shorten the life. All of the fully-reversed (R = –1) samples failed on the surface of the samples, although there are only three of these tests. One of the fully reversed tests was a runout, and the other two (110 and 193) had shortened lives due to adiabatic heating. This was observed by a large and localized temperature rise before failure. One of these samples was observed glowing immediately before breakage and the other had an oxidized band on the gage surface surrounding the failed region. Figure 25 compares all of the tests at 149 °C to the MMPDS fits at 20 °C. The AM material has similar fatigue lives as those from the MMPDS source not taking the temperature difference into account. At this temperature the UTS of the AM materials is equivalent to the UTS from the MMPDS material at 20 °C. Hence one would expect the fatigue lives to agree with one another.

Tests conducted at –196 °C are listed in Table VII and shown in Figure 26. There is a slight separation of data with respect to the loading ratio but it is less distinct than at the other two temperatures. As expected the maximum stress values at this temperature are approximately 50 percent higher than those at 20 °C for equivalent fatigue lives. The UTS at this temperature is 1660 MPa. The few samples taken from the horizontal build and tested at R = 0.5 are interspersed within the data. There appears to be minimal differences among the lots, although such a comparison can only be made at a load ratio of 0.5. Most of the samples failed from internal initiation sites and 20 percent of these initiated at inclusions. The inclusions did not appear to affect the fatigue lives. The few samples that did fail from the surface tended to have lower lives, particularly for the fully-reversed tests. Of these tests, two samples (12 and 51) initiated in the grips at the threads, although this did not seem to reduce the life of these samples.

The HCF data are summarized according to load ratio in the next plots. Data from all temperatures are plotted for each mean stress. The fully-reversed tests are shown in Figure 27 and have a slight ranking based on test temperature with the lowest temperature yielding the longest, stress-equivalent, life. The two data points on the left of Figure 27 (at lives ≤ 1000 cycles) experienced the adiabatic heating. Data for the other two mean stresses are given in Figures 28 and 29. The lives are dependent on test temperature to a greater degree than for the fully-reversed condition. This is especially true in the shorter life regime.

Typical HCF fracture surfaces are shown in Figure 30 for each test temperature and some specific initiation sites are shown in Figure 31. As mentioned previously, the initiation points could be either surface or internal. Fatigue striations were observed at higher magnifications. High cycle fatigue tested samples had a greater tendency to fail at inclusions compared to tensile or low cycle fatigue samples. The inclusions provided a stress concentration to initiate the cracks at low stress levels. The largest, most prevalent inclusions were Nb particles (Fig. 31(a)). The composition was pure Nb, no other elements were detected by EDS analysis. The particles were round, ranged from 60 to 100 μm in diameter, and appeared to be from prior powder particles. The source of the Nb was not determined. The ARCAM machine used is dedicated to fabricating Ti-6Al-4V and had never had a different composition of powder in the machine. The only powder that was used was purchased from ARCAM. Other inclusions found on the fracture surfaces were Si (Fig. 31(b)), TiC, and Al_2O_3. A few samples also had failures initiate at areas that had chemistries slightly off the baseline, usually EDS analysis indicated slightly low Al levels.

Examination of the fracture surface allowed the identification of the crack initiation site. A short description is given in the last column of Tables V to VII. Most, but not all, of the samples at R = 0.1 and 0.5 contained some anomaly at their initiation site. The defects were categorized into five types: porosity, Nb particles, TiC particles, Si particles, and other, which included Al-containing particles (probably Al_2O_3), prior powder particles, and unknown (not investigated with SEM). The distribution of these types

and their maximum dimension is given in Table VIII. The average particle size was approximately 80 μm with a standard deviation of 25 μm. The category of unknown defects had twice this standard deviation in sizes, but many of these defects were estimated using a poorer resolution optical scope to save time and hence more scatter is expected. The crack origin of four samples contained one to several very small pores with the maximum measured size of 20 μm. This implies that the HIP process performed as expected and closed most of the porosity resulting from the build.

Examination of samples containing defects at their origins revealed that the defects made no noticeable difference in the HCF lives. Consequently, one type of defect was not more severe than another type with regard to degrading the life of the samples. This is not unexpected since the size of the defects is relatively small. A study in gamma TiAl (Ref. 16) indicated that any defect smaller than a cross-sectional area of 0.1 mm^2 (equal to a linear size of 350 μm) had no detrimental effect on fatigue life for this brittle and notch sensitive material. Between the smaller defect sizes observed in this study and the higher ductility in Ti-6-4 we would not expect these flaws in AM Ti-6-4 to degrade life. However, there was a significant impact on the fatigue lives that was related to the location of the origin. Samples that initiated on the surface or near surface of the sample experienced lower life than those that initiated internally. For example in Figure 31(a), sample 121 tested at 20 °C failed at a surface connected Nb particle. As shown in Figure 21 this sample had a 3-4x shorter life than the other samples with internal initiation sites. Figure 31(b) depicts an internal initiation site in sample 76. This sample exhibited a very long life as shown in Figure 24 in spite of its 150 μm long Si inclusion. It can be observed in Figure 31(b) that the circular area of crack growth is fully contained within the sample and only breaks the surface plane in the final overload. Thus, the fatigue crack was not influenced by the surrounding atmosphere. Prior work has shown that environment influences cracking in titanium alloys. Ritchie (Ref. 17) and Gao (Ref. 18) have shown the crack growth rates in Ti-6-4 at high frequencies are faster in water vapor than in vacuum. Gao demonstrated that the growth rates increased as a function of the partial pressure of water vapor in the system. Geathers (Ref. 19) showed that small cracks initiated and grew more quickly in Ti-6242 in laboratory air versus vacuum. All of these authors associated the environmental effect with an interaction with water vapor, either resulting in hydrogen embrittlement or some oxidation effect at the crack tip. Thus exposing the crack to the ambient environment as experienced by surface initiation flaws in this study would explain the lower fatigue lives during HCF.

A visual comparison was made of the sample HCF lives to the build location (shown in Figs. 1 and 4). It was thought that certain build locations might exhibit consistently lower lives than others. No obvious correlation was discovered. Moreover, it was thought that certain build locations may encourage the formation of inclusions or certain types of inclusions. Again no specific correlation was found. This implies that given the specific build patterns used here, defects were random throughout the builds. Nonetheless, certain inclusions should not have appeared in this material at all (such as Nb) and better care should be taken in maintaining powder cleanliness.

To summarize, neither build location nor defect size or type had an influence on the fatigue life. The only factors to alter fatigue life were surface connected initiation sites and lot build, the latter is suspected to be a result of the build's UTS resulting from various textures.

Low Cycle Fatigue

The low cycle fatigue (LCF) data are shown in Table IX for the 20 °C tests. The LCF tests were conducted in strain control between total strain limits. All three lots of material were tested under these conditions and are plotted in Figure 32 as a function of the maximum stress, similar to those of the HCF tests. The reversed s-shaped fatigue curve shown by the data in this figure is typical of that observed in most metallic materials (Ref. 20). All three lots of material fall generally on the same life curve, until at high stresses where lot 1 separates from the other two lots. Moreover, at the high stresses there is much scatter in the fatigue lives as an apparent stress plateau is reached. The stress plateaus roughly agree with the proportional limits (PL) from each lot as shown by the dashed lines. Also shown in Figure 32 are the HCF data from R = –1 and 20 °C. These data are equivalent to those of the LCF tests at intermediate

lives, although the HCF lives are slightly longer. This could be a test frequency effect since the HCF tests were conducted at 20 Hz compared to only 0.5 Hz for the LCF test. The tensile tests were conducted at a still slower strain rate equivalent frequency of 0.01 Hz. Ti-6-4 has been shown to be time and rate dependent, even at room temperature (Ref. 21), showing significant creep and relaxation at 20 °C (Refs. 22 and 23). The fatigue limits show the largest difference, as the LCF limits appear to be 50 to 150 MPa lower than those from the HCF tests. Both the LCF and HCF data are replotted in Figure 33 as a function of total strain range. All data, LCF, HCF and all lots, fall on one smooth curve having an approximate fatigue limit at 0.75 percent strain range. It should be noted that all but one of the LCF tests failed by multiple edge-initiated sites around the circumference of the sample, an example of which is shown in Figure 34. Sample 162 failed from an internal location where the microstructure contained some Si, Figure 35.

LCF data from a test temperature of 149 °C are shown in Table X and plotted as a function of maximum stress in Figure 36. For this set of conditions there is a slight difference (≈3X) between lot 1 and 2 over the entire life regime shown, where lot 1 has longer lives. The stress plateau in the short life regime agrees very well with the temperature and lot dependent proportional limit in spite of the load rate difference. The HCF data are also plotted for these test conditions and they fit remarkably well with the LCF data and do not exhibit a frequency effect similar to what was observed at 20 °C. Even the two samples that experienced adiabatic heating fit with the LCF response. All of these data are plotted as a function of strain range in Figure 37 and show excellent agreement over the life regime. The only two exceptions are the samples that experienced adiabatic heating. They have a much lower strain range per given life. The real strain range for these samples is probably higher and localized in the region of adiabatic shear. LCF initiation sites at 149 °C occurred at both internal and surface locations. Two of the internal initiation sites contained Si in the microstructure similar to that shown in Figure 35. Of the surface initiated samples, multiple surface initiation sites were common.

Test data for tests at –196 °C are given in Table XI and plotted in Figure 38. Again both lots show equivalent life behavior except at the short life regime where they separate from one another in accordance with their proportional limits. The HCF data for the –196 °C temperatures show good agreement with the LCF data. Good agreement is also observed in Figure 39 for lives based on a strain range basis. There is no evidence in this strain-based plot of an influence of either lot or frequency. LCF cracks at –196 °C generally initiated at the surface, as shown in Figure 40, but a few internal initiation sites were also observed.

The LCF lives are plotted in Figures 41 and 42 for all temperatures based on the maximum stress and strain range, respectively. Figure 41 shows that there is little difference between the 20 and 149 °C data particularly at lower lives. The –196 °C data however lies at much higher stresses per given life than the other two temperatures. It appears in Figure 42 that the two higher temperatures have identical lives on a strain range basis. At –196 °C there is a slight difference as indicated by a shallower slope to its fatigue curve.

Finally for completeness, all fatigue data for the R = –1 loading conditions and the MMPDS fit are shown versus maximum stress (Fig. 43) and strain range (Fig. 44). The data appear to be self-consistent and behave as expected. Moreover, on a strain range basis there is little difference observed amongst the temperatures. Hence Figure 44 could be used as a master curve for this material under fully-reversed conditions. It can also be observed in both of these figures, as well as many of the previous figures, that the AM material has equivalent or better fatigue properties than the conventionally manufactured material.

Fatigue Crack Growth Rate (FCGR)

FCGR tests were performed at temperatures of –196, 20, and 149 °C at load ratios of R = 0.1, 0.5, and 0.7. The test matrix is shown in Table XII. Indicated in the table is the specimen ID, location in the build, test temperature, load ratio R and the test type. To fully characterize the FCG behavior, tests were

performed so that the crack growth data encompassed various regions of the crack growth curves while also allowing for an overlap of data from region to region.

The complete data set of all the fatigue crack growth test results is shown in Figure 45, while the data is separated into various categories in Figures 46 to 49. Figure 46 presents the room temperature fatigue crack growth response as a function of the load ratio, R. The fatigue crack growth data trends shown in the figure are typical of R ratio behavior that occurs for most metallic alloys. The R = 0.1 exhibits lower crack growth rates in terms of the applied stress intensity range than the tests performed at the R ratios of 0.5 and 0.7. Also as expected, the threshold stress intensity range (ΔKth) for R = 0.1 was higher than for the other R ratios. The R = 0.7 condition exhibited the lowest ΔKth in line with expectations. The room temperature fatigue crack growth data at the three load ratios is replotted in terms of maximum applied stress intensity, Kmax in Figure 47. As shown, the onset of Stage 3 crack growth behavior occurs for all three load ratios at a Kmax of approximately 41.8 MPa√m as manifested by the upswing in the fatigue crack growth curves. A comparison of fatigue crack growth response of additive manufacturing produced Ti-6-4 to conventionally produced Ti-6-4 at room temperature for similar R ratios is shown in Figure 48. As shown in the figure, the AM Ti-6-4 is very similar to the solution treated and over aged (STOA) Ti-6-4 (Ref. 17). Note that the FCG response for STOA is very similar to that of the annealed state. One point of difference is that the threshold for annealed Ti-6-4 at an R of 0.1 is approximately 10 MPa√m (Ref. 2), which is higher than either the thresholds for the STOA or the AM samples.

Cryogenic fatigue crack growth testing exhibited significant scatter and noise. In order to establish fatigue crack growth trends a number of test repeats were performed. Several of these tests were performed at large stress intensity gradients in an effort to characterize larger regions of the response curve and reduce the amount of liquid nitrogen expended. Figure 49 shows variation among the four tests performed to characterize the same region of R = 0.1 response. As shown, while the fatigue crack growth data is repeatable in the Stage 2, Paris regime, there is substantial variability in the threshold stress intensity. Thus only a range of ΔKth values can be established based on these tests as is also shown in Figure 49.

Comparison of the measured fatigue crack growth response at the three temperatures at R = 0.1 and R = 0.7 is shown correspondingly in Figures 50 and 51. As shown in these two figures, the fatigue crack growth rates for a given R ratio are fairly similar between the three temperatures especially in the Stage 2 Paris regime.

Fractographic examination for selected specimens at the three test temperatures was performed. Representative fractographs are shown in Figure 52 from tests performed at R = 0.1. As shown, the failure mode is similar at all three temperatures. The influence of the underlying microstructure is evident as the crack growth closely followed the Ti-6-4 alpha-beta structure.

Fracture Toughness

Fracture toughness tests were performed in accordance with ASTM E1820, which gives provisions for J-integral regression analysis as well as linear elastic plane-strain fracture toughness determination. Specimens were additively manufactured in batches of 12 arranged in a 3 by 4 array on the build table (Fig. 2). Table XIII summarizes the results of the fracture toughness testing.

Room temperature testing provided valid results for both analyses, while 149 °C tests were only valid using J-integral analysis and –196 °C did not produce valid results for either methodology. The cryogenic tests had little stable crack extension before brittle fracture. While not meeting all validity criteria, the linear elastic plane-strain analysis can provide reasonable values for fracture toughness for these tests.

The fracture toughness results are also shown in Figure 53 as a function of test temperature and the location of the specimen within the additive manufacturing build plate. As shown both in this figure as well in Table XIII, the fracture toughness values varied substantially as a function of temperature and showed little variation with regards to the location within each build. The average measured fracture toughness (KIC or KQ) was approximately 31 MPa√m at the –196 °C test temp, 60 MPa√m at RT and 120 MPa√m at 149 °C. The measured elasto-plastic fracture toughness values (JIC or JQ) are also shown

in Table XIII and also increase substantially as the test temperature is increased. It should be noted that no relationship was found between the measured fracture toughness, which varied substantially as a function of temperature, and the measured fatigue crack growth behavior in the Stage II, Paris regime that showed very little differences as a function of temperature, but does appear to agree with the Stage III values.

Thermal Analysis

The density of the thermal analysis samples, after the HIP cycle, was 4.414 g/cm^3, close to the material property database density listing of 4.43 g/cm^3 for conventional Ti-6Al-4V (Ref. 24). The thermal diffusivity, specific heat, thermal conductivity, and thermal expansion results are listed in Tables XIV to XVIII and plotted in Figures 54 to 57. The mean coefficients of expansion were calculated from the thermal expansion data and are listed in Table XVIII and plotted in Figure 58. The data for each lot of material were nearly identical. A few handbook (Refs. 2 and 24) data points are listed in Tables XIV to XVI for comparison. The CTE plot is consistent with conventionally manufactured Ti-6Al-4V but with more scatter. The large change in CTE at room temperature is due to the measuring technique and the resolution of the measuring device. Below room temperature, the measurement chamber is placed under a vacuum and then back filled with helium while above room temperature, measurements are taken in air.

Summary

An in-depth material characterization of Electron Beam Melted (EBM) Ti-6Al-4V material has been completed on Ti-6Al-4V samples fabricated on an ARCAM A2X EBM machine. The specimens were fabricated under eight separate builds with the material divided into two lots for material testing purposes. Chemical analysis of the powder, taken from the Arcam machine before every build, had oxygen levels above ASTM limits. The high oxygen level was also present in the fabricated samples. Hot Isostatic Pressing (HIP) was utilized to close porosity from fabrication and also served as a material heat treatment to obtain the desired microstructure. The microstructure is made up of columnar prior β grains, a transformed α + β microstructure. Transmission electron microscopy was utilized to verify the presence of the α and β phases and determine their orientation relationship. The microstructure was quantified as far as prior beta grain size, colony size and alpha lath thickness and length, with all microstructural features being very refined compared to conventionally manufactured material. This refined microstructure resulted in higher strength compared to conventionally manufactured material. A significant difference in tensile and fatigue strength was observed between the two lots of samples that could only be attributed to fiber texture being present in lot 1, the higher strength lot. A few horizontal samples, fabricated with their loading axis perpendicular to the build growth direction, were mechanically tested and their strengths were similar to lot 2 samples. Even with oxygen levels above ASTM standards, the tensile ductility of the AM Ti-6-4 exceeded S-basis values for annealed Ti-6-4 extrusions.

High cycle fatigue tests showed that the additive manufactured samples had superior strength compared to both ASTM and MMPDS data at room temperature. Increasing the load ratio resulted in higher fatigue limits. At higher stress levels (>700 MPa), the data from R = 0.1 and 0.5 were similar indicating a smaller influence of mean stress on life. At test temperatures of 149 °C, a typical maximum stress-life ranking as a function of mean stress was observed with fatigue limits of 400, 550, and 650 MPa for the load ratios of –1, 0.1, and 0.5, respectively. The fatigue limits at 149 °C were equal to those at 20 °C at R = 0.5, and lower at the R = 0.1 and –1. At similar stresses, samples from lot 1 have a slightly longer life than those from lot 2. At 149 °C, the UTS of the AM materials is equivalent to the UTS from the MMPDS material at 20 °C resulting in similar fatigue lives for the AM material at 149 °C as the MMPDS material at 20 °C. At a cryogenic test temperature of –196 °C, there is a slight separation of data with respect to the loading ratio but it is less distinct than at the other two temperatures. As expected, the maximum stress values at this temperature are approximately 50 percent higher than those at 20 °C for

equivalent fatigue lives. Crack initiation of the high cycle fatigue samples occurred at both the surface and from internal sites with samples having internal initiations tending to have longer lives than those initiating on the surface of the sample. High cycle fatigue tested samples had a higher tendency to fail at inclusions compared to tensile or low cycle fatigue samples. The inclusions provided a stress concentration to initiate the cracks at low stress levels. The largest, most prevalent inclusions were Nb particles, which appeared to be prior powder particles.

Low cycle fatigue properties are consistent with the HCF properties as data in both life regimes fall onto a smooth curve. The LCF properties are a function of powder lot and correlate with the resulting tensile strength of the lot, the higher the strength the higher the fatigue life. When the fatigue data are plotted on a strain range basis, these data collapse onto one curve irrespective of powder lot. While inclusions were certainly present in the LCF samples, fatigue cracking initiated at the sample surface and usually at multiple sites around the circumference of the sample.

As with the fatigue properties, the fatigue crack growth response of AM Ti-6-4 was similar to conventionally manufactured Ti-6-4 and showed typical R ratio behavior. The fatigue crack growth rates for a given R ratio were similar among the three test temperatures of –196, –20, and 149 °C. Fractography showed that the crack growth closely followed the Ti-6-4 alpha-beta structure. The fracture toughness of AM Ti-6-4 varied substantially as a function of temperature with the fracture toughness increasing with temperature, as expected. The thermal properties of AM Ti-6-4 were comparable to conventionally manufactured material.

Conclusions

EBM Ti-6-4 had equivalent or superior properties compared to conventionally manufactured material over the temperature range investigated. The high strength of the material is attributed to the refined microstructure. While defects were present in the material, the size of the defects initiating fatigue cracks was too small to adversely affect the cyclic lives. Powder cleanliness is a potential problem as unexpected elements were found as inclusions. It is recommended that critical components be HIPed after manufacturing to eliminate porosity and homogenize the microstructure. Moreover we anticipate a degradation in fatigue life due to the as-built surface finish compared to a well-machined (and/or polished) surface. The excellent mechanical properties of HIP'ed EBM Ti-6Al-4V should be sufficient to design and manufacture aerospace components.

References

1. Donachie, M.J., *Titanium – A Technical Guide*, Second Edition, ASM, Materials Park, OH, 2000.
2. *Metallic Materials Properties Development and Standardization Handbook (MMPDS-07)*, Chapter 5 – Titanium Alloys, April 2012, Copyright 2012 Federal Aviation Administration, licensed to Battelle Memorial Institute, 505 King Avenue, Columbus, OH 43201.
3. Facchini, L., Magalini, E., Robotti, P., and Molinari, A.: "Microstructure and Mechanical Properties of Ti-6Al-4V Produced by Electron Beam Melting of Pre-Alloyed Powders," Rapid Prototyping Journal, Vol. 15, No. 3, (2009), pp. 171–178.
4. Svensson, M., MSV083_Material Properties of EBM- Manufactured Ti6Al4V – ELI with 50 μm layer, EBM Control 3.2 SP1 and Scan Length Dependency, Arcam AB, March 2012.
5. Frazier, William. "Metal Additive Manufacturing: A Review." J. of Materials Engineering and Performance, 23(6) (2014): 1917–1928.
6. Xu, W., Brandt, M., Sun, S., Elambasseril, J., Liu, Q., Latham, K., Xia, K., Qian, M. "Additive manufacturing of strong and ductile Ti-6Al-4V by selective laser melting via insitu martensite decomposition." Acta Materialia, 85 (2015) 74–84.
7. Ahmed, T.; Rack, H.J. "Phase transformations during cooling in α+β titanium alloys. Mater. Sci. Eng. A 243 (1998) 206.

8. Ackelid, Ulf; personal communication, 2016.
9. Murr, L.E. et al: “Characterization of titanium aluminide alloy components fabricated by additive manufacturing using electron beam melting,” Acta Materialia 58 (2010) 1887–1894.
10. Karlsson, J., Snis, A., Engqvist, H., Lausmaa, J.: “Characterization and comparison of materials produced by Electron Beam Melting (EBM) of two different Ti-6Al-4V powder fractions.” J. of Materials Processing Technology 213 (2013) 2109–2118.
11. Lütjering, G.: “Influence of processing on microstructure and mechanical properties of (α+β) titanium alloys.” Mat. Science and Eng. A243 (1998) 32–45.
12. Nalla, R.K., Boyce, B.L., Campbell, J.P., Peters, J.O., Ritchie, R.O.: “Influence of microstructure on High-Cycle Fatigue of Ti-6Al-4V: Bimodal vs. Lamellar Structures.” Metallurgical and Materials Transactions A. 33A (2002) 899–918.
13. Lütjering, G., Albrecht, J.: “Influence of cooling rate and β grain size on the tensile properties of (α+β) Ti-Alloys.” Titanium ’95:Science and Technology, Proceedings of the Eighth World Conference on Titanium, edited by P.A. Blenkinsop, W.J. Evans, and H.M. Flower, The Institute of Materials (1995) p. 1163–1170.
14. Al-Bermani, S.S., Blackmore, M.L., Zhang, W., Todd, I: “The origin of microstructural diversity, texture, and mechanical properties in electron bean melted Ti-6Al-4V.” Metallurgical and Materials Transactions A 41A (2010) 3422–3434.
15. Siemiatin, S.L., Bieler, T.R.: “Effect of texture and slip mode on the anisotropy of plastic flow and flow softening during hot working of Ti-6Al-4V.” Metallurgical and Materials Transactions A 32A (2001) 1787–1799.
16. Draper, S.L., et al: “Durability Assessment of Gamma TiAl – Final Report, NASA/TM—2004-212303.
17. Ritchie, R.O., Davidson, D.L., Boyce, B.L., Campbell, J.P., and Roder, O., “High-cycle fatigue of Ti–6Al–4V, Fatigue Fract Engng Mater Struct 22, 1999, pp. 621–631.
18. Gao, S.J., Simmons, G.W. and Wei, R.P., “Fatigue Crack Growth and Surface Reactions for Titanium Alloys Exposed to Water Vapor, Materials Science and Engineering, Vol. 62, 1984, pp. 65–78.
19. Geathers J., Torbet C.J., Jones J.W., Daly, S., “Investigating environmental effects on small fatigue crack growth in Ti–6242S using combined ultrasonic fatigue and scanning electron microscopy,” International Journal of Fatigue vol. 70, 2015, pp. 54–162.
20. Schijve, J., Fatigue Crack Growth under Variable-Amplitude Loading, ASM Handbook, Fatigue and Fracture, Vol. 19, 1996, ASM, Materials Park, OH, p111.
21. B.A. Lerch and S.M. Arnold, “Viscoelastic Response of the Titanium Alloy Ti-6-4: Experimental Identification of Time and Rate-Dependent Reversible and Irreversible Deformation Regions,” NASA/TM—2014-216584, April, 2014.
22. Wapniarsky, S.; Rotem, A.I.; and Rosen, A.: Creep of Ti-6Al-4V Titanium Alloy at Room Temperature. Strength of Metals and Alloys (ICSMA 9); Proceedings of the 9th International Conference, Technion—Israel Institute of Technology, Haifa, vol. 1, 1991, pp. 437–442.
23. Evans, W.J., “Stress Relaxation and Notch Fatigue in Ti-6Al-4V,” Scripta Metallurgica, 1987, vol. 21, pp. 1223–1227.
24. Boyer, R., Welsch, G., Collings, E.W.: *Materials Properties Handbook: Titanium Alloys*, ASM International (1994).

TABLE I.—POWDER AND AS-FABRICATED CHEMISTRY, wt%

Sample	Ti	Al	V	C	O	N	Fe	Cr	Si
Powder 1_1	Bal.	6.65	4.02	0.009	0.21	0.022	0.12	0.007	0.008
Powder 1_2	Bal.	6.67	4.04	0.009	0.24	0.024	0.12	0.007	0.008
Powder 2	Bal.	6.57	3.98	0.008	0.23	0.022	0.13	0.008	0.01
Powder 3	Bal.	6.58	3.97	0.010	0.25	0.024	0.13	0.007	0.009
Powder 4	Bal.	6.62	3.99	0.009	0.23	0.023	0.13	0.008	0.009
Powder 5	Bal.	6.59	3.98	0.008	0.24	0.020	0.13	0.007	0.007
Powder 6	Bal.	6.62	4.02	0.010	0.24	0.021	0.13	0.007	0.009
Arcam cert.	Bal.	6.4	4.0	0.01	0.12	0.02	------	------	------
ASTM F2924	Bal.	5.5 to 6.75	3.5 to 4.5	Max. 0.08	Max. 0.2	Max. 0.05	Max. 0.30	Max. 0.1	Max. 0.1

TABLE II.—POST HIP CHEMISTRY, wt%

Sample	Ti	Al	V	C	O	N	Fe	Cr	Si
Lot 1 bottom	Bal.	6.57	4.05	0.009	0.24	0.021	0.10	0.006	0.010
Lot 1 gage	Bal.	6.49	3.99	-----	0.23	0.021	0.11	0.007	0.011
Lot 1 top	Bal.	6.33	3.98	0.009	0.22	0.020	0.10	0.006	0.01
Lot 2 bottom	Bal.	6.37	4.13	0.009	0.27	0.021	0.10	0.006	0.009
Lot 2 gage	Bal.	6.32	4.08	-----	0.25	0.022	0.10	0.006	0.009
Lot 2 top	Bal.	6.43	4.11	0.010	0.24	0.021	0.11	0.007	0.011
Horizontal	Bal.	6.62	4.07	0.011	0.26	0.022	0.15	0.007	0.015

TABLE III.—MICROSTRUCTURAL CHARACTERIZATION

Sample	Orientation (in relation to EBM growth axis)	Location	Colony size, μm	α lath thickness, μm	Prior β grain size, μm
Lot 1	Transverse	Bottom	7.1±0.4	----------	----------
Lot 1	Transverse	Gage	7.7±0.5	1.9±0.1	----------
Lot 1	Transverse	Top	6.3±0.4	1.9±0.1	----------
Lot 1	Longitudinal	Gage	----------	----------	82±9
Lot 2	Transverse	Bottom	7.0±0.4	----------	----------
Lot 2	Transverse	Gage	6.8±0.4	1.9±0.1	----------
Lot 2	Transverse	Top	5.9±0.4	1.7±0.1	----------
Lot 2	Longitudinal	Gage	----------	----------	91±11
Horizontal	Longitudinal	Gage	11.1±0.7	2.8±0.2	----------
Horizontal	Transverse	Grip	13.6±1.0	2.8±0.2	----------

TABLE IV.—TENSILE PROPERTIES

Sample	Build	Ez, GPa	Proportional limit, MPa	0.02% yield, MPa	0.2% yield, MPa	Ultimate strength, MPa	Failure strength, MPa	Failure strain, percent	RA, percent
–196 °C									
25	1-1-2	129	1530	1534	1702	1744	1671	10.9	20
43	1-1-2	126	1582	1582	1696	1731	1695	8.1	13
105	1-2-2	126	1579	1583	1695	1733	1682	9.8	17
122	2-4-1	124	1407	1416	1555	1608	1607	5.8	6.5
170	2-4-5	121	1452	1455	1549	1605	1565	12.2	18
191	2-4-9	120	1478	1478	1589	1646	1633	8.8	12
–101 °C									
28	1-1-1	128	1272	1283	1336	1394	1289	14.0	26
55	1-1-4	124	1243	1258	1324	1387	1301	14.3	22
95	1-2-2	127	1266	1276	1339	1406	1356	12.4	19
147	2-4-3	121	1180	1187	1243	1300	1274	13.1	18
160	2-4-4	119	1191	1196	1237	1287	1238	13.7	22
198	2-4-8	122	1117	1160	1244	1304	1208	15.7	27
20 °C									
16	1-1-2	125	------	------	------	------	------	------	------
65	1-1-4	124	974	998	1028	1126	1000	21.5	30
67	1-1-4	122	980	1000	1025	1122	998	21.0	31
115	1-2-1	126	967	992	1024	1140	1014	20.7	30
135	2-4-2	118	908	929	960	1042	962	20.2	28
173	2-4-6	118	914	935	965	1051	960	20.7	29
186	2-4-6	118	928	941	972	1048	1027	9.8	11
H1	------	118	865	896	958	1058	970	13.6	12
H3	------	119	831	866	950	1057	992	13.2	14
H11	------	118	866	901	977	1081	1064	14.4	13
149 °C									
34	1-1-2	118	745	788	813	948	676	18.1	49
78	1-1-3	117	768	798	819	941	627	22.0	55
86	1-2-2	117	792	804	817	944	834	18.2	43
141	2-4-1	111	701	722	747	841	576	22.0	58
153	2-4-5	113	689	730	760	854	753	17.1	50
183	2-4-9	113	729	749	775	861	540	21.1	39

TABLE V.—HCF TESTS AT 20 °C

Maximum Stress, σ_{max} MPa	Minimum Stress, σ_{min} MPa	Mean Stress, σ_m MPa	Life, N_f	Sample	Lot	crack origin
$R_\sigma = -1$						
483	-420	0.7	10,000,000	4	1	runout
635	-635	2.6	39,108	4	1	grip, surface
622	-620	0.6	52,032	20	1	surface
587	-586	0.7	123,795	27	1	surface at Nb inclusion
550	-548	0.8	10,000,000	37	1	runout
496	-497	-0.4	10,000,000	47	1	runout
587	-585	0.9	30,712	58	1	surface at Nb inclusion
688	-692	-2.0	32,868	75	1	surface
534	-535	0.0	102,065	84	1	surface
536	-536	0.4	12,024,109	11	1	runout
567	-567	0.0	1,412,254	92	1	grip, surface
562	-564	-0.9	336,510	114(2)	1	internal
758	-759	-0.5	15,760	119	1	surface
$R_\sigma = 0.1$						
964	94.2	529	120,531	15	1	internal
618	58	338	331,422	21	1	surface at Nb inclusion
689	67.8	378	839,032	40	1	internal porosity
908	88.4	498	205,163	45	1	internal
551	54.3	303	10,000,000	54	1	runout
621	61.8	341	22,328,131	64	1	internal
587	58.5	323	10,000,000	73	1	runout
758	74.7	416	101,215	121	1	surface at Nb inclusion
826	79.2	452	297,443	97	1	internal
655	64.7	360	6,034,945	117	1	internal
$R_\sigma = 0.5$						
689	344	516	11,000,000	7	1	runout
717	357	537	3,671,511	26	1	internal
827	413	620	161,157	39	1	surface inclusion
773	384	578	2,311,370	42	1	internal
800	399	599	955,282	60	1	surface inclusion
881	439	660	3,654,457	63	1	internal
965	476	721	761,035	72	1	internal
662	331	496	10,000,000	93	1	runout
882	441	661	2,054,429	104	1	surface
716	355	536	10,000,000	114	1	runout
661	331	496	10,000,000	H12	H	runout
828	463	646	2,585,750	H12(2)	H	internal
773	431	602	4,489,262	H9	H	surface
964	481	722	261,700	H7	H	surface
689	343	516	5,916,964	129	2	internal particle
771	384	577	838,484	133	2	internal
855	428	642	1,854,431	145	2	internal
964	480	722	138,729	155	2	internal
661	331	496	8,252,663	163	2	internal
745	373	559	2,999,634	168	2	internal
909	450	680	242,307	174	2	internal
772	386	579	121,354	184	2	surface
965	467	716	246,239	196	2	internal
717	359	538	88,279	202	2	particle at surface

TABLE V.—IHCF TESTS AT 149 °C

Maximum Stress, σ_{max} MPa	Minimum Stress, σ_{min} MPa	Mean Stress, σ_m MPa	Life, N_f	Sample	Lot	crack origin
$R_\sigma = -1$						
484	-480	2.2	127,422	44	1	surface
551	-552	-0.6	142,669	107	1	surface at Nb inclusion
763	-776	-6.5	981	110	1	adiabatic heating
414	-413	0.2	10,000,000	151	2	runout
482	-484	-0.8	51,668	201	2	surface at Nb inclusion
690	-697	-3.2	320	193	2	adiabatic heating
$R_\sigma = 0.1$						
550	45	297	541,630	36	1	surface at Nb inclusion
620	61	341	1,674,714	57	1	internal
757	74	416	17,661	81	1	surface
482	48	265	10,000,000	143	2	runout
551	54	303	10,000,000	171	2	runout
689	68	378	1,686,265	181	2	internal at Nb Particle
$R_\sigma = 0.5$						
772	386	579	2,961,594	1	1	internal
828	402	615	97,752	8	1	surface
963	471	717	26,468	23	1	internal
716	357	537	5,810,681	76	1	internal
689	353	521	3,124,622	157	2	internal
758	378	568	900,788	123	2	internal
897	442	670	106,657	137	2	internal
654	327	491	10,000,000	176	2	runout

TABLE VII.—HCF TESTS AT –196 °C

Maximum Stress, σ_{max} MPa	Minimum Stress, σ_{min} MPa	Mean Stress, σ_m MPa	Life, N_f	Sample	Lot	crack origin
$R_\sigma = -1$						
630	-630	0.0	160,462	12	1	threads
552	-552	0.0	94,639	29	1	surface
630	-630	0.0	2,234,180	32	1	surface at Nb inclusion
552	-552	0.0	11,750,626	41	1	runout
758	-758	0.0	98,609	51	1	threads
758	-758	0.0	4,552,669	61	1	internal
896	-896	0.0	16,081	79	1	internal
690	-690	0.0	51,155	89	1	surface
827	-827	0.0	927,136	101	1	internal
517	-517	0.0	10,636,540	112	1	runout
$R_\sigma = 0.1$						
621	62	342	3,603,715	9	1	surface
690	69	380	10,002,345	18	1	runout
758	76	417	2,930,641	24	1	internal
586	59	323	4,332,806	33	1	internal
552	55	304	10,063,185	48	1	runout
758	76	417	2,965,297	56	1	internal
965	97	531	718,507	70	1	internal
1241	124	683	29,528	90	1	internal
1103	110	607	19,524	94	1	internal
862	86	474	1,024,629	108	1	internal
$R_\sigma = 0.5$						
690	345	518	2,972,413	14	1	internal
552	276	414	10,163,400	17	1	runout
607	303	455	10,500,542	31	1	runout
827	414	621	2,595,774	49	1	internal
1103	552	828	31,977	52	1	surface
896	448	672	405,970	69	1	internal
965	483	724	956,186	85	1	internal
1172	586	879	394,388	99	1	internal
621	310	466	10,001,513	102	1	runout
1379	690	1035	127,995	116	1	internal
1034	517	776	435,974	H5	H	surface
1207	603	905	41,828	H8	H	internal
690	345	518	10,102,711	H2	H	runout
1379	690	1035	20,094	126	2	internal
965	483	724	697,049	139	2	internal
621	310	466	10,169,351	142	2	runout
1172	586	879	137,851	148	2	internal
827	414	621	9,324,523	152	2	surface
724	362	543	11,496,187	159	2	runout
552	276	414	10,001,999	165	2	runout
1379	690	1035	327,548	178	2	surface
676	338	507	10,531,419	187	2	runout
1103	552	828	302,179	199	2	internal

TABLE VIII.—DEFECT SIZE AT CRACK ORIGIN

Defect type	Number observed	Average size, μm	Std. Dev., μm
pores	4	12.8	6.1
Nb	8	84.5	29.3
TiC	14	78.1	20.3
Si	2	127.5	----
other	17	90	53.2

TABLE IX.—LCF TESTS AT 20 °C

Sample #	Total strain range, $\Delta\varepsilon_t$, mm/mm	Life, Nf, cycles	First cycle, N=1					Half-life, $N_f/2$				
			Modulus (GPa)	Maximum stress, σ_{max}, MPa	Maximum strain, ε_{max}, percent	Minimum stress, σ_{min}, MPa	Minimum strain, ε_{min}, percent	Modulus (GPa)	Maximum stress, σ_{max}, MPa	Maximum strain, ε_{max}, percent	Minimum stress, σ_{min}, MPa	Minimum strain, ε_{min}, percent
Lot 1												
10	0.0100	30243	124	630	0.506	-642	-0.513	126	620	0.496	-633	-0.507
22	0.0076	105495	126	479	0.382	-488	-0.386	126	477	0.381	-470	-0.377
30	0.0128	6945	125	801	0.643	-822	-0.654	127	784	0.631	-808	-0.645
35	0.0253	809	124	1153	1.313	-1175	-0.870	120	894	1.267	-1011	-1.263
53	0.0304	477	124	1161	1.563	-1292	-1.532	116	895	1.518	-996	-1.517
59	0.0354	242	124	1168	1.817	-1318	-1.787	116	887	1.770	-988	-1.769
80	0.0278	651	124	319	0.260	-270	-0.216	116	886	1.393	-988	-1.390
96	0.0328	407	125	1163	1.694	-1327	-1.659	115	890	1.642	-998	-1.638
106	0.0176	2788	125	1074	0.880	-1086	-0.875	124	915	0.882	-964	-0.877
118	0.0227	1145	125	1171	1.238	-1203	-1.145	120	905	1.141	-1009	-1.133
Lot 2												
124	0.0076	209644	120	457	0.382	-465	-0.383	122	475	0.382	-442	-0.379
136	0.0100	43863	120	603	0.508	-625	-0.511	122	596	0.496	-606	-0.502
130	0.0127	10591	119	755	0.640	-803	-0.655	122	744	0.630	-785	-0.644
146	0.0254	822	120	1075	1.291	-1189	-1.286	116	841	1.269	-928	-1.267
156	0.0304	596	119	1089	1.562	-1227	-1.535	112	841	1.522	-925	-1.518
162	0.0355	225	120	1094	1.811	-1256	-1.786	112	831	1.774	-921	-1.774
167	0.0279	692	118	1064	1.422	-1190	-1.407	113	830	1.394	-912	-1.394
180	0.0330	180	119	1090	1.688	-1242	-1.659	113	855	1.651	-950	-1.649
192	0.0177	2681	120	1031	0.883	-1067	-0.881	121	854	0.882	-907	-0.886
194	0.0226	1248	119	1077	1.203	-1173	-1.161	117	836	1.130	-916	-1.135
Horizontal												
H4	0.0100	30496	121	609	0.508	-633	-0.512	123	582	0.497	-625	-0.499
H6	0.0203	822	119	1052	1.070	-1098	-1.028	119	827	1.015	-907	-1.019
H10	0.0304	260	120	1080	1.552	-1196	-1.533	115	857	1.521	-932	-1.523

TABLE X.—LCF TESTS AT 149 °C

Sample #	Total strain range, $\Delta\varepsilon_t$, mm/mm	Life, Nf, cycles	First cycle, N=1					Half-life, N_f/ 2				
			Modulus (GPa)	Maximum stress, σ_{max}, MPa	Maximum strain, ε_{max}, percent	Minimum stress, σ_{min}, MPa	Minimum strain, ε_{min}, percent	Modulus (GPa)	Maximum stress, σ_{max}, MPa	Maximum strain, ε_{max}, percent	Minimum stress, σ_{min}, MPa	Minimum strain, ε_{min}, percent
Lot 1												
71	0.0355	298	117	932	1.791	-1079	-1.787	110	778	1.770	-873	-1.776
83	0.0279	650	118	924	1.435	-1087	-1.404	112	783	1.392	-900	-1.396
62	0.0255	698	117	927	1.299	-1037	-1.282	111	776	1.267	-879	-1.279
120	0.0228	591	118	919	1.154	-1034	-1.157	115	777	1.139	-891	-1.143
111	0.0329	497	119	933	1.666	-1110	-1.661	111	795	1.643	-895	-1.644
68	0.0304	672	117	926	1.552	-1057	-1.535	109	781	1.516	-870	-1.521
38	0.0099	32180	120	600	0.505	-617	-0.518	120	592	0.488	-591	-0.506
50	0.0127	8748	118	743	0.640	-784	-0.656	118	679	0.632	-705	-0.639
98	0.0177	3016	118	907	0.966	-963	-0.906	115	734	0.878	-798	-0.887
19	0.0077	214003	117	444	0.381	-455	-0.386	118	457	0.383	-443	-0.382
Lot 2												
138	0.0128	9464	114	720	0.640	-753	-0.649	113	637	0.635	-663	-0.642
190	0.0331	257	113	877	1.668	-991	-1.639	107	740	1.653	-826	-1.662
172	0.0304	392	112	868	1.553	-982	-1.530	107	725	1.522	-801	-1.518
182	0.0277	793	113	890	1.430	-992	-1.405	109	732	1.394	-804	-1.375
175	0.0356	506	113	879	1.788	-1001	-1.783	104	728	1.775	-803	-1.787
185	0.0176	3252	112	859	0.959	-897	-0.906	110	669	0.881	-719	-0.878
150	0.0253	1089	113	859	1.299	-950	-1.279	109	708	1.267	-777	-1.262
197	0.0227	1532	112	865	1.160	-938	-1.150	109	701	1.141	-762	-1.131
131	0.0100	25420	113	571	0.507	-586	-0.509	115	543	0.495	-590	-0.507
125	0.0076	173014	113	434	0.388	-442	-0.383	115	436	0.383	-431	-0.379

TABLE XI.—LCF TESTS AT –196 °C

Sample #	Total strain range, $\Delta\varepsilon_t$, mm/mm	Life, Nf, cycles	First cycle, N=1					Half-life, N_f/ 2				
			Modulus (GPa)	Maximum stress, σ_{max}, MPa	Maximum strain, ε_{max}, percent	Minimum stress, σ_{min}, MPa	Minimum strain, ε_{min}, percent	Modulus (GPa)	Maximum stress, σ_{max}, MPa	Maximum strain, ε_{max}, percent	Minimum stress, σ_{min}, MPa	Minimum strain, ε_{min}, percent
Lot 1												
3	0.0200	5066	125	1240		-1292		125	1187		-1294	
6	0.0150	43468	126	926		-954		126	912		-969	
13	0.0250	1179	125	1509		-1704		125	1511		-1662	
46	0.0170	27128	125	1028		-1091		125	1045		-1097	
74	0.0180	9092	125	1131		-1132		125	1136		-1132	
77	0.0220	2446	124	1321		-1434		124	1309		-1392	
88	0.0275	759	126	1620		-1818		125	1620		-1747	
103	0.0300	747	123	1682		-1820		122	1669		-1820	
109	0.0350	77	119	1774		-1726		117	1764		-1687	
113	0.0325	149	123	1764		-1820		120	1764		-1693	
Lot 2												
127	0.0170	30082	120	999		-1031		120	994		-1036	
132	0.0200	4698	121	1160		-1251		121	1158		-1254	
144	0.0250	1744	120	1438		-1557		120	1426		-1556	
154	0.0300	185	121	1571		-1817		121	1590		-1713	
158	0.0350	59	118	1639		-1626		116	1653		-1607	
166	0.0325	84	119	1639		-1820		119	1645		-1731	
169	0.0275	1070	119	1544		-1679		119	1517		-1651	
177	0.0180	5495	121	1074		-1089		121	1084		-1077	
188	0.0230	4876	121	1342		-1421		121	1360		-1403	
200	0.0300	467	121	1611		-1809		119	1609		-1729	

TABLE XII.—FATIGUE CRACK GROWTH TEST MATRIX

Sample #	Lot	Build	Location In Build	Load ratio, R	Test Type
-196 °C					
FCG 13	1	3	side edge	0.7	Paris Region
FCG 22	1	3	middle	0.7	Decreasing K, threshold test
FCG 12	1	3	side edge	0.5	Decreasing K, threshold test and Paris Region
FCG 7	1	3	middle	0.1	Decreasing K, threshold test and Paris Region
FCG 2	1	3	top edge	0.1	Decreasing K, threshold test and Paris Region
FCG 19	1	3	middle	0.1	Decreasing K, threshold test and Paris Region
FCG 3	1	3	top edge	0.1	Decreasing K, threshold test and Paris Region
FCG 6	1	3	middle	0.1	Decreasing K, threshold test and Paris Region
FCG 30	2	6	top edge	0.7	Decreasing K, threshold test
FCG 32	2	6	corner	0.7	Paris Region
FCG 35	2	6	middle	0.1	Paris Region
20 °C					
FCG 5	1	3	side edge	0.7	Paris Region
FCG 14	1	3	middle	0.7	Decreasing K, threshold test
FCG 20	1	3	side edge	0.7	Decreasing K, threshold test
FCG 23	1	3	middle	0.7	Stage III Paris Region
FCG 4	1	3	corner	0.5	Paris Region
FCG 11	1	3	middle	0.5	Decreasing K, threshold test
FCG 17	1	3	side edge	0.5	Decreasing K, threshold test
FCG 26	1	3	bottom edge	0.5	Stage II-III Paris Region
FCG 1	1	3	Corner	0.1	Decreasing K, threshold test
FCG 10	1	3	middle	0.1	Paris Region
FCG 16	1	3	side edge	0.1	Stage I-II Paris Region
FCG 27	1	3	bottom edge	0.1	Stage III Paris Region
FCG 29	2	6	Corner	0.7	Decreasing K, threshold test
FCG 33	2	6	side edge	0.7	Paris Region
FCG 39	2	6	middle	0.7	Paris Region
FCG 37	2	6	side edge	0.1	Paris Region
149 °C					
FCG 8	1	3	side edge	0.7	Decreasing K, threshold test
FCG 9	1	3	side edge	0.7	Paris Region
FCG 15	1	3	middle	0.1	Paris Region
FCG 25	1	3	corner	0.7	Stage II-III Paris Region
FCG 31	2	6	top edge	0.7	Decreasing K, threshold test
FCG 34	2	6	middle	0.7	Paris Region
FCG 36	2	6	side edge	0.1	Paris Region

TABLE XIII.—FRACTURE TOUGHNESS RESULTS

20 °C								
Sample #	**Lot**	**Build**	**Location in Build**	**J_Q [J/cm^2]**	**Valid J_Q as J_{IC}**	**K_{JIC} [MPa sqrt(m)]**	**K_Q [MPa sqrt(m)]**	**Valid K_{IC}**
FT-2	1	2	top edge	3.31	yes	66.0	60.97	yes
FT-4	1	2	side edge	3.55	yes	68.5	61.47	yes
FT-9	1	2	side edge	4.03	yes	73.0	62.66	yes
FT-11	1	2	bottom edge	3.48	yes	67.8	62.01	yes
FT-13	2	5	corner	3.27	yes	65.6	59.96	yes
FT-17	2	5	middle	3.14	yes	64.4	59.67	yes
FT-21	2	5	side edge	3.04	yes	63.4	57.72	yes
FT-23	2	5	bottom edge	3.47	yes	67.6	62.23	yes
149 °C								
Sample #	**Lot**	**Build**	**Location in Build**	**J_Q [J/cm^2]**	**Valid J_Q as J_{IC}**	**K_{JIC} [MPa sqrt(m)]**	**K_Q [MPa sqrt(m)]**	**Valid K_{IC}**
FT-3	1	2	corner	12.72	yes	126.5	87.53	no
FT-5	1	2	middle	10.61	yes	115.5	88.05	no
FT-7	1	2	side edge	12.00	yes	122.9	90.98	no
FT-12	1	2	corner	11.43	yes	119.9	89.61	no
FT-15	2	5	corner	12.22	yes	123.9	89.80	no
FT-18	2	5	side edge	10.84	yes	116.8	89.46	no
FT-20	2	5	middle	9.89	yes	111.5	81.94	no
FT-22	2	5	corner	12.12	yes	123.5	88.05	no
-196 °C								
Sample #	**Lot**	**Build**	**Location in Build**	**J_Q [J/cm^2]**	**Valid J_Q as J_{IC}**	**K_{JIC} [MPa sqrt(m)]**	**K_Q [MPa sqrt(m)]**	**Valid K_{IC}**
FT-1	1	2	corner	0.81	no	31.6	32.09	no
FT-6	1	2	side edge	0.82	no	31.4	32.09	no
FT-8	1	2	middle	0.80	no	31.2	31.54	no
FT-10	1	2	corner	0.67	no	28.7	30.33	no
FT-14	2	5	top edge	0.00	no	0.0	30.66	no
FT-16	2	5	side edge	0.63	no	28.2	31.76	no
FT-19	2	5	side edge	0.76	no	31.3	32.20	no
FT-24	2	5	corner	0.74	no	30.5	30.77	no

TABLE XIV.—THERMAL DIFFUSIVITY

Temperature, °C	Diffusivity Lot 1, cm^2/sec	Diffusivity Lot 2, cm^2/sec	Diffusivity handbook (Ref. 24), cm^2/sec
–150	0.02780	0.02785	
–125	0.02769	0.02749	
–100	0.02753	0.02748	
–75	0.02763	0.02745	
–50	0.02776	0.02756	
–25	0.02805	0.02784	
0	0.02846	0.02843	
23	0.02914	0.02893	0.027
50	0.02983	0.02987	
75	0.03075	0.03068	
100	0.03139	0.03088	
125	0.03167	0.03163	
150	0.03257	0.03284	

TABLE XV.—SPECIFIC HEAT

Temperature, °C	Specific heat Lot 1, J/Kg•K	Specific heat Lot 2, J/Kg•K	Specific heat (Refs. 2 and 24), J/Kg•K
–150	337.6	343.3	-----
–145	353.7	360.9	-----
–140	368.9	376.1	-----
–135	382.6	389.9	-----
–130	395.3	402.2	414.5
–125	406.8	413.0	-----
–120	417.2	422.9	-----
–115	427.0	431.3	-----
–110	435.9	439.3	-----
–105	443.9	446.1	-----
–100	451.2	452.3	-----
–95	457.9	457.9	-----
–90	463.9	463.0	-----
–85	469.5	467.7	-----
–80	474.5	472.1	-----
–75	479.2	476.2	-----
–70	483.5	480.1	-----
–65	487.4	483.8	-----
–60	491.0	487.3	-----
–55	494.4	490.8	-----
–50	497.6	4941	-----
–45	500.5	497.3	502
–40	503.3	500.4	-----
–35	506.0	503.4	-----
–30	508.6	506.4	-----
–25	511.1	509.2	-----
–20	513.5	512.0	527
–15	515.9	514.7	-----
–10	518.2	517.2	-----
–5	520.5	519.7	-----
0	522.7	522.0	-----
5	525.0	524.3	-----
10	527.2	526.4	-----
15	529.4	528.4	-----
20	531.5	530.3	544
25	533.6	532.1	-----
30	535.6	533.8	-----
35	537.6	535.4	-----
40	539.5	537.0	-----
45	541.3	538.7	-----
50	542.9	540.4	-----
55	543.4	543.3	-----
60	545.5	545.0	-----
65	547.3	546.8	-----
70	548.8	548.4	-----
75	550.5	550.0	-----
80	552.2	551.8	-----
85	554.0	553.7	-----
90	555.7	555.4	-----
95	557.2	557.1	569
100	558.7	558.7	-----
105	560.4	560.4	-----
110	562.4	562.1	-----
115	563.9	563.6	-----
120	565.6	565.0	-----

Table XV.—Concluded.

Temperature, °C	Specific heat Lot 1, J/Kg•K	Specific heat Lot 2, J/Kg•K	Specific heat Refs. 2 and 24, J/Kg•K
125	567.0	566.5	-----
130	568.5	567.7	-----
135	569.9	569.4	-----
140	571.2	570.6	-----
145	572.9	572.6	-----
150	574.7	574.5	-----

TABLE XVI.—THERMAL CONDUCTIVITY CALCULATIONS

Sample	Temp. °C	Density, gm/cm^3	Specific heat, J/Kg*K	Diffusivity, cm^2/s	Thermal conductivity, W/cm*K	Thermal conductivity, W/cm*K (Ref. 24)
Lot 1	–150	4.4142	337.6	0.02780	0.0143	-------
	–125	4.4142	406.8	0.02769	0.04972	-------
	–100	4.4142	451.2	0.02753	0.05484	-------
	–75	4.4142	479.2	0.02763	0.05845	-------
	–50	4.4142	497.6	0.02776	0.06098	-------
	–25	4.4142	511.1	0.02805	0.06329	-------
	0	4.4142	522.7	0.02846	0.06568	-------
	23	4.4142	532.8	0.02914	0.06854	0.068
	50	4.4142	542.9	0.02983	0.07149	-------
	75	4.4142	550.5	0.03075	0.07473	-------
	100	4.4142	558.7	0.03139	0.07742	0.075
	125	4.4142	567.0	0.03167	0.07927	-------
	150	4.4142	574.7	0.03257	0.08264	-------
Lot 2	–150	4.4308	343.3	0.02785	0.04236	-------
	–125	4.4308	413.0	0.02749	0.05031	-------
	–100	4.4308	452.3	0.02748	0.05507	-------
	–75	4.4308	476.2	0.02745	0.05793	-------
	–50	4.4308	494.1	0.02756	0.06034	-------
	–25	4.4308	509.2	0.02784	0.06282	-------
	0	4.4308	522.0	0.02843	0.06577	-------
	23	4.4308	531.3	0.02893	0.06812	-------
	50	4.4308	540.4	0.02987	0.07152	-------
	75	4.4308	550.0	0.03068	0.07477	-------
	100	4.4308	558.7	0.03088	0.07645	-------
	125	4.4308	566.5	0.03163	0.07940	-------
	150	4.4308	574.5	0.03284	0.08360	-------

TABLE XVII.—THERMAL EXPANSION RESULTS

Temperature, °C	Lot 1, cm/cm	Lot 2, cm/cm
–150	–0.001352	–0.001323
–145	–0.001324	–0.001289
–140	–0.001291	–0.001261
–135	–0.001257	–0.001233
–130	–0.001227	–0.001198
–125	–0.001186	–0.001162
–120	–0.001155	–0.001126
–115	–0.001119	–0.001090
–110	–0.001081	–0.001052
–105	–0.001048	–0.001013
–100	–0.001009	–0.000980
–95	–0.000971	–0.000946
–90	–0.000930	–0.000906
–85	–0.000894	–0.000869
–80	–0.000852	–0.000828
–75	–0.000811	–0.000791
–70	–0.000766	–0.000752
–65	–0.000726	–0.000712
–60	–0.000680	–0.000671
–55	–0.000639	–0.000631
–50	–0.000599	–0.000585
–45	–0.000553	–0.000544
–40	–0.000513	–0.000504
–35	–0.000472	–0.000463
–30	–0.000431	–0.000422
–25	–0.000391	–0.000382
–20	–0.000347	–0.000338
–15	–0.000302	–0.000293
–10	–0.000261	–0.000247
–5	–0.000216	–0.000212
0	–0.000175	–0.000166
5	–0.000130	–0.000121
10	–0.000084	–0.000081
15	–0.000044	–0.000040
20	0.000000	0.000000
25	0.000045	0.000046
30	0.000090	0.000092
35	0.000135	0.000137
40	0.000180	0.000182
45	0.000224	0.000232
50	0.000269	0.000276
55	0.000319	0.000321
60	0.000364	0.000366
65	0.000409	0.000411
70	0.000453	0.000455
75	0.000498	0.000500
80	0.000545	0.000547
85	0.000593	0.000589
90	0.000640	0.000642
95	0.000688	0.000685
100	0.000736	0.000732
105	0.000778	0.000780
110	0.000826	0.000828
115	0.000874	0.000870
120	0.000921	0.000918
125	0.000964	0.000961

Table XVII.—Concluded.

Temperature, °C	Lot 1, cm/cm	Lot 2, cm/cm
130	0.001013	0.001010
135	0.001063	0.001059
140	0.001113	0.001104
145	0.001157	0.001154
150	0.001202	0.001199

TABLE XVIII.—MEAN COEFFICIENTS OF EXPANSION RESULTS

Temperature, °C	Lot 1, μm/μm °C	Lot 2, μm/μm °C
–150	7.9582	7.7851
–145	8.0270	7.8157
–140	8.0689	7.8840
–135	8.1154	7.9568
–130	8.1856	7.9885
–125	8.1837	8.0153
–120	8.2550	8.0440
–115	8.2936	8.0748
–110	8.3229	8.0957
–105	8.3882	8.1108
–100	8.4160	8.1700
–95	8.4463	8.2343
–90	8.4620	8.2404
–85	8.5174	8.2853
–80	8.5269	8.2834
–75	8.5375	8.3352
–70	8.5205	8.3642
–65	8.5441	8.3787
–60	8.5065	8.3951
–55	8.5323	8.4136
–50	8.5619	8.3614
–45	8.5169	8.3802
–40	8.5501	8.4021
–35	8.5893	8.4280
–30	8.6364	8.4590
–25	8.6939	8.4970
–20	8.6885	8.4672
–15	8.6297	8.3769
–10	8.7224	8.2566
–5	8.6468	8.4991
0	8.7903	8.3491
5	8.6868	8.0992
10	8.4799	8.1131
15	8.8869	8.1546
25	9.0663	9.2702
30	9.0663	9.2702
35	9.0286	9.1640
40	9.0098	9.1109
45	8.9985	9.2845
50	8.9909	9.2291
55	9.1323	9.1894
60	9.1100	9.1597
65	9.0925	9.1366
70	9.0786	9.1181
75	9.0672	9.1029
80	9.0885	9.1211
85	9.1233	9.0742
90	9.1531	9.1808
95	9.1789	9.1361
100	9.2015	9.1613
105	9.1609	9.1835
110	9.1820	9.2032
115	9.2015	9.1668
120	9.2178	9.1853

Table XVIII.—Concluded.

Temperature, °C	Lot 1, µm/µm °C	Lot 2, µm/µm °C
125	9.1842	9.1532
130	9.2126	9.1829
135	9.2453	9.2169
140	9.2753	9.2052
145	9.2618	9.2355
150	9.2494	9.2240

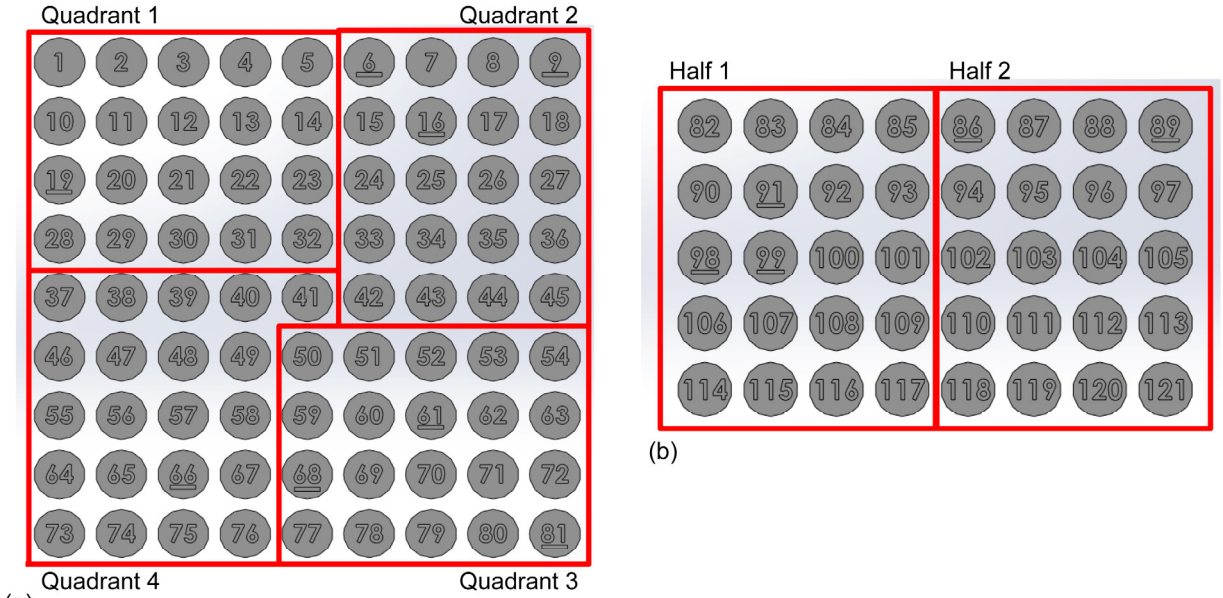

Figure 1.—Lot 1 tensile and fatigue samples built vertically over 2 builds with (a) build 1_1 using 4 quadrants and (b) build 1_2 using 2 halves. The build, or z-direction, is out of the plane of the paper.

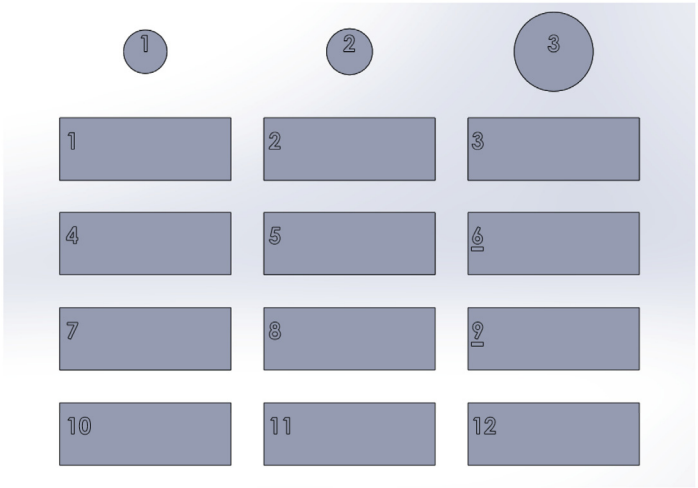

Figure 2.—Build 2 fabricated lot 1 thermal analysis and fracture toughness samples. The same layout was used for lot 2 fracture toughness samples number 13 to 24 in build 5. The build or z-direction is out of the plane of the paper.

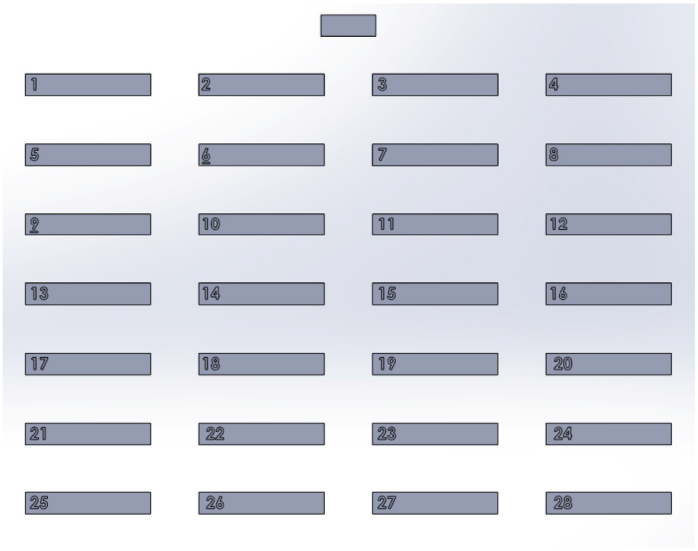

Figure 3.—Build 3 fabricated lot 1 dynamic modulus and fatigue crack growth samples. The same layout was used for build 7 for lot 2 fatigue crack growth samples number 29 to 56. The build or z-direction is out of the plane of the paper.

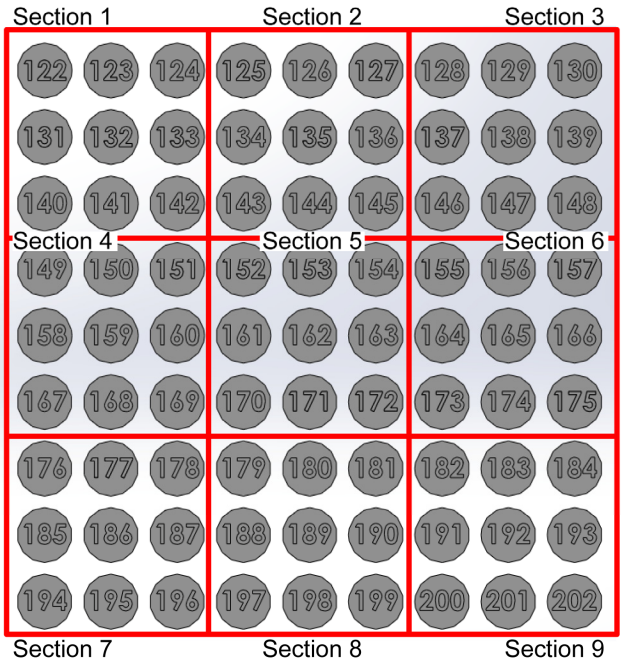

Figure 4.—Lot 2 tensile and fatigue samples built vertically using 9 sections. The build or z-direction is out of the plane of the paper.

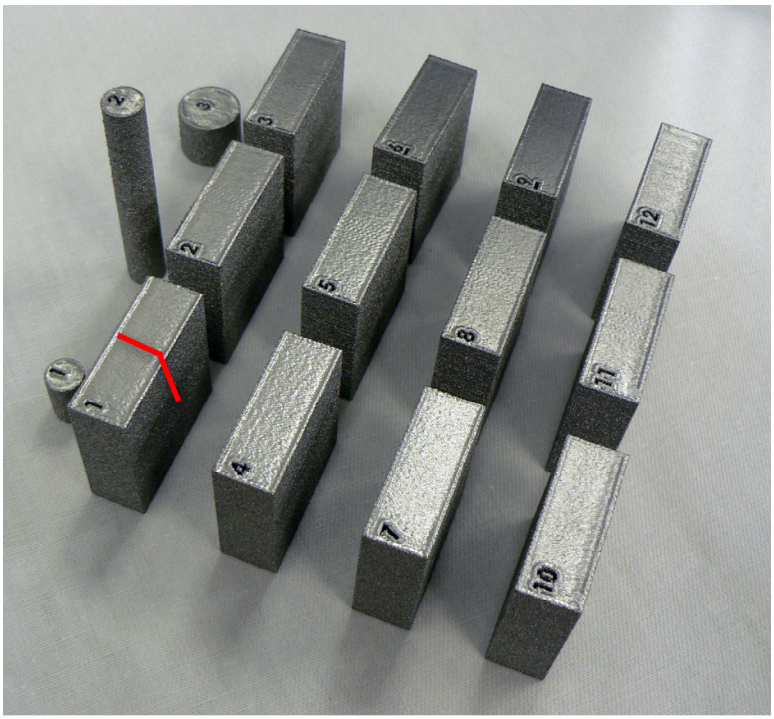

Figure 5.—Build 2 after removal from Arcam. Red lines indicate notch directions for fracture toughness and FCG samples.

(a)

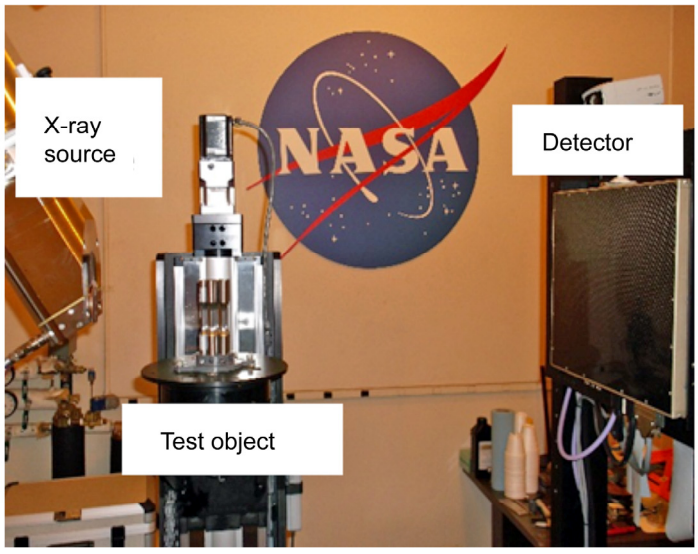

(b)

Figure 6.—(a) Micro-focus computed tomography (CT) system with a fixture mounted on a rotating stage allowing (b) 6 samples to be scanned simultaneously.

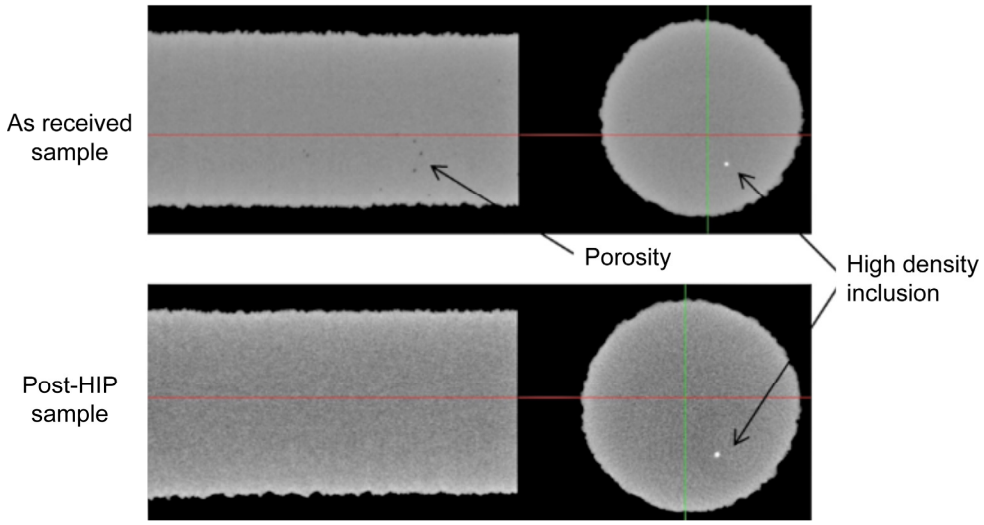

Figure 7.—CT image of Ti-6-4 sample before and after HIP.

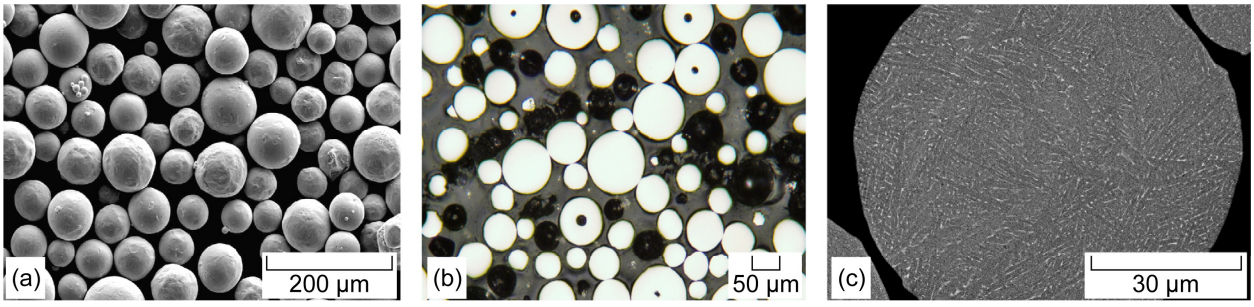

Figure 8.—(a) SE image of loose Arcam Ti-6Al-4V powder. (b) Cross-sectional view of polished powder. (c) Higher magnification BSE image of powder.

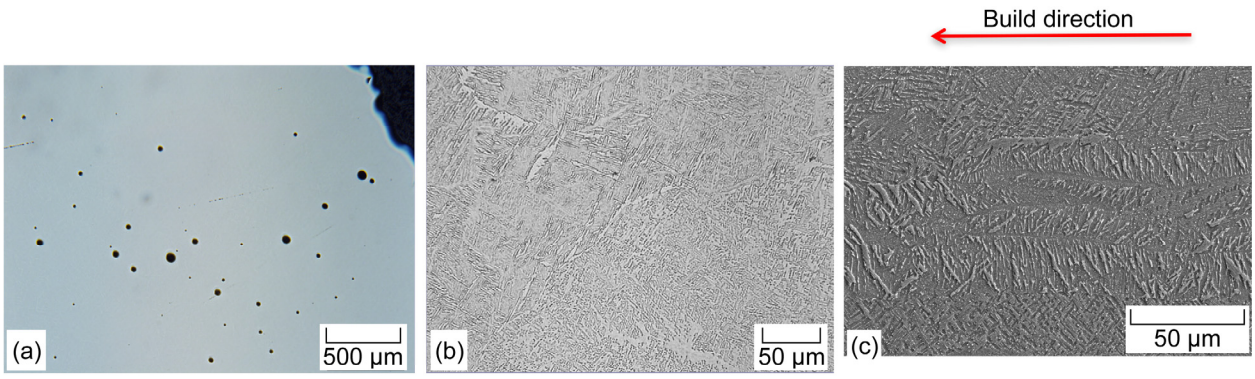

Figure 9.—(a) Optical image of unetched and (b) etched as-fabricated sample in the direction transverse to the build showing porosity and microstructure before HIP. (c) SEM image of an as-fabricated sample in the longitudinal, direction showing prior beta grain size elongated in growth direction.

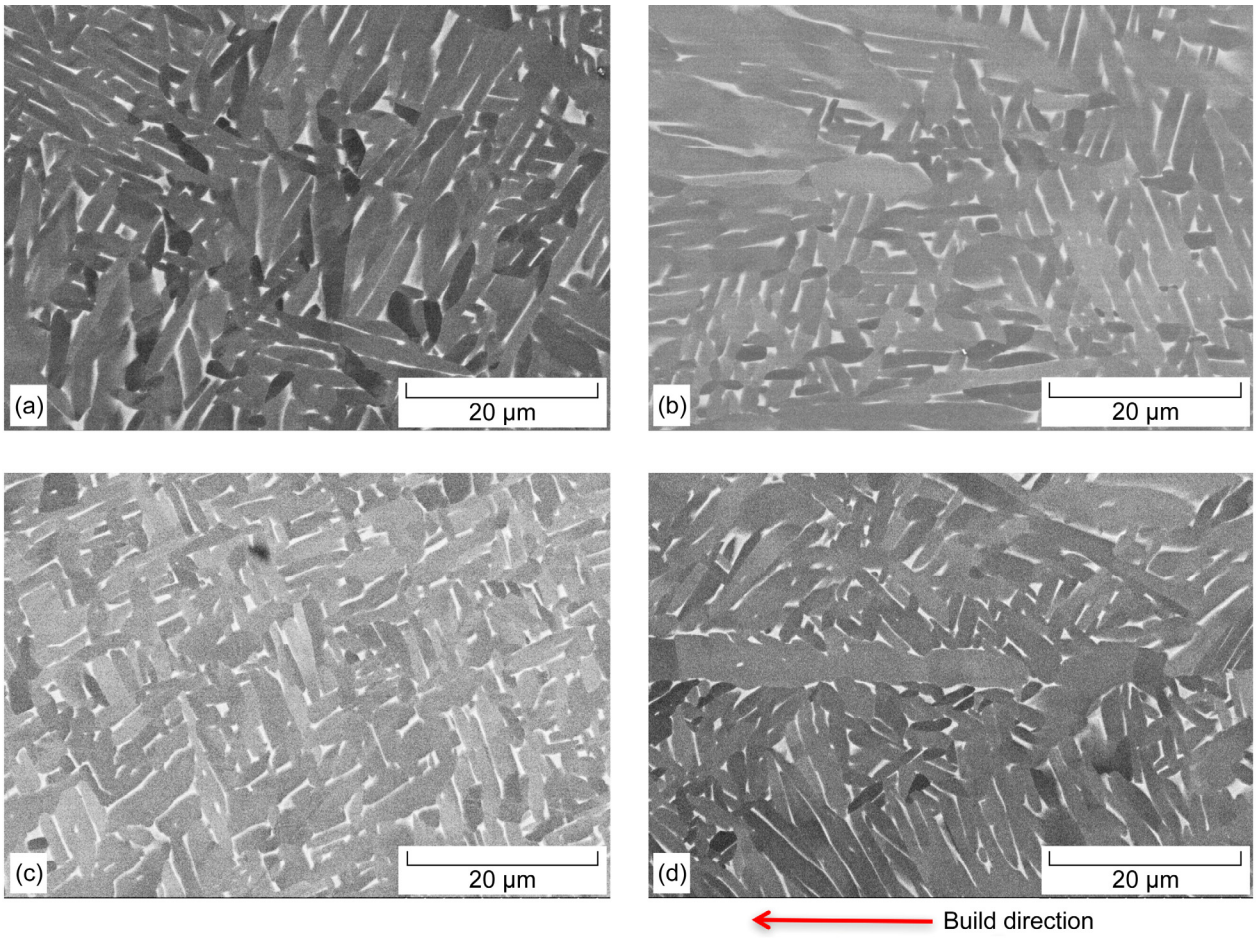

Figure 10.—BSE images of HIP'd microstructure from lots 1 and 2 in (a,c) transverse and (b,d) parallel to growth direction.

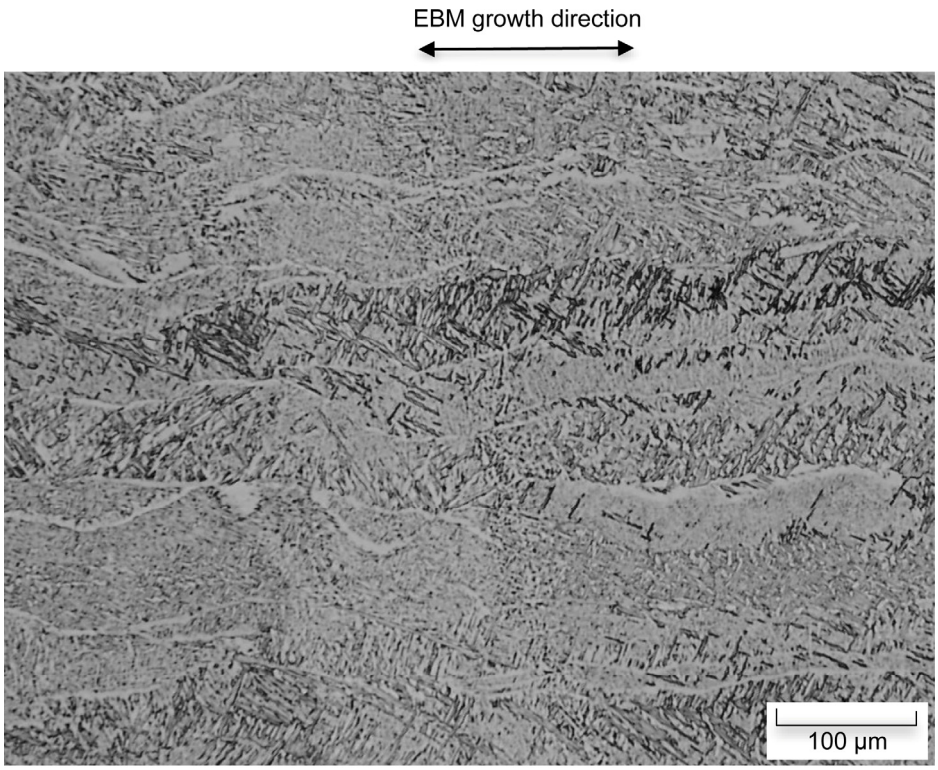

Figure 11.—Optical image of longitudinal section showing prior beta grain boundaries parallel to growth direction.

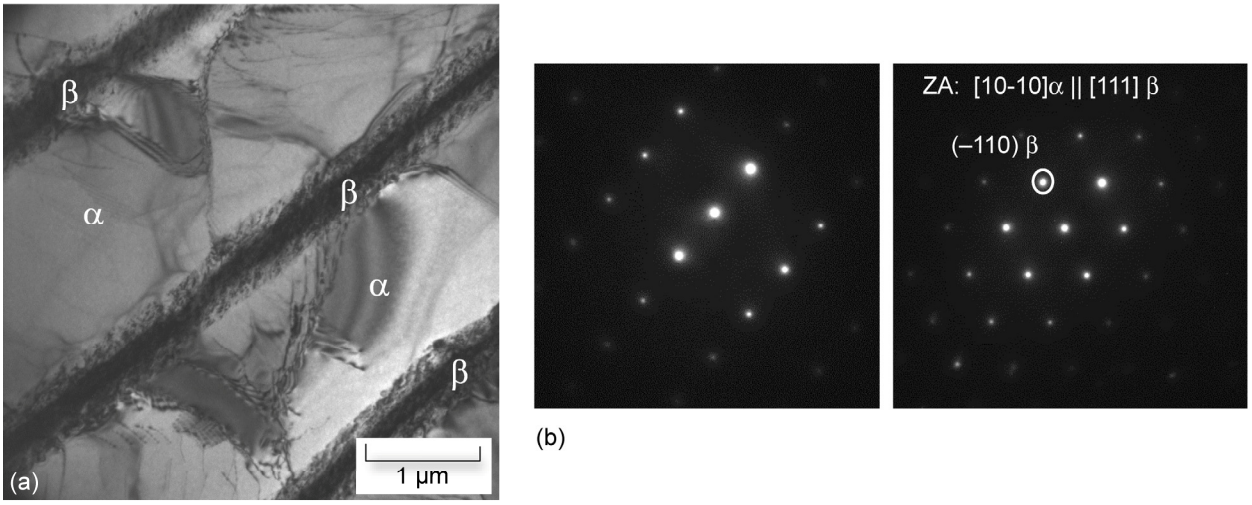

Figure 12.—(a) Transmission electron microscope image. (b) Corresponding diffraction patterns determined orientation relationship between α and β.

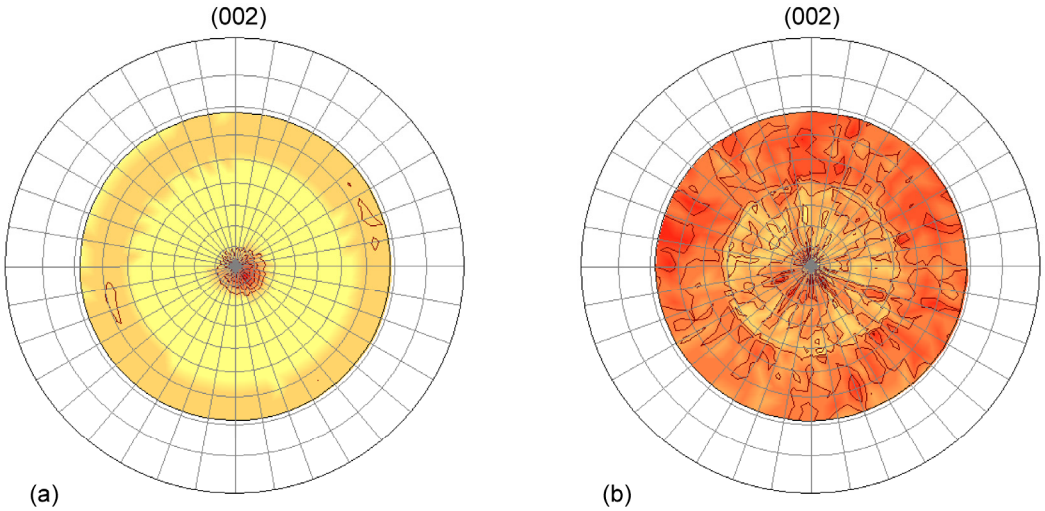

Figure 13.—(002) pole figures from (a) lot 1 showing fiber texture, (b) lot 2 showing random texture with sample surface oriented perpendicular to the build direction.

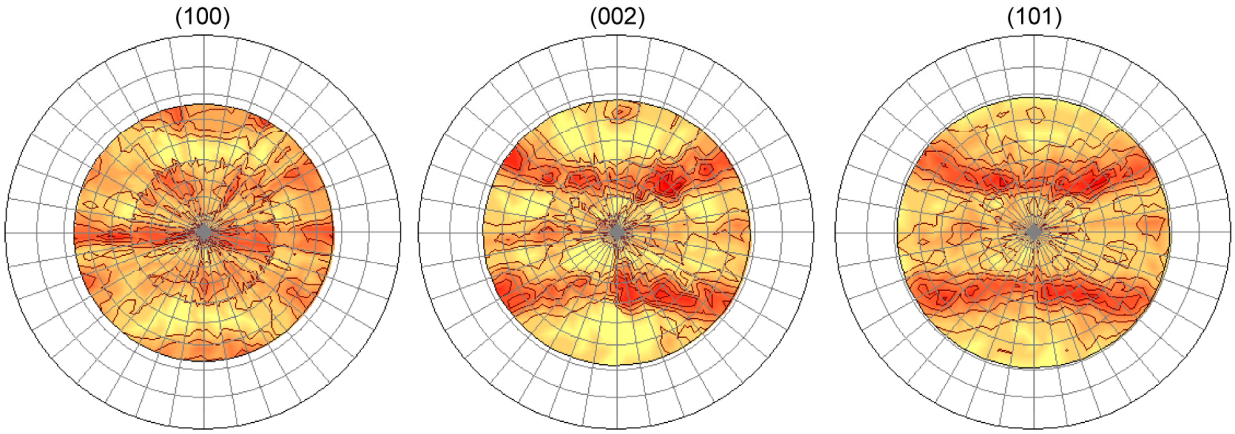

Figure 14.—(100), (002), and (101) Pole figures from a horizontal sample with the sample surface perpendicular to the growth direction. Pole figures show coexisting (100), (002), and (101) α-Ti fiber textures with all three fiber axes parallel to the build direction.

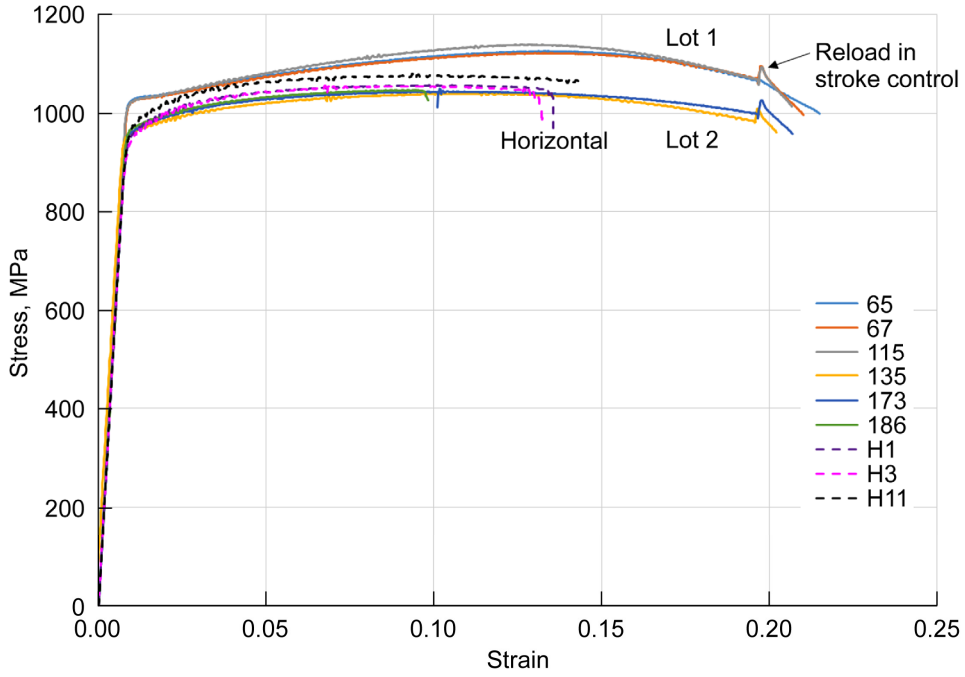

Figure 15.—Room temperature tensile at 20 °C, results for lots 1, 2, and horizontal samples.

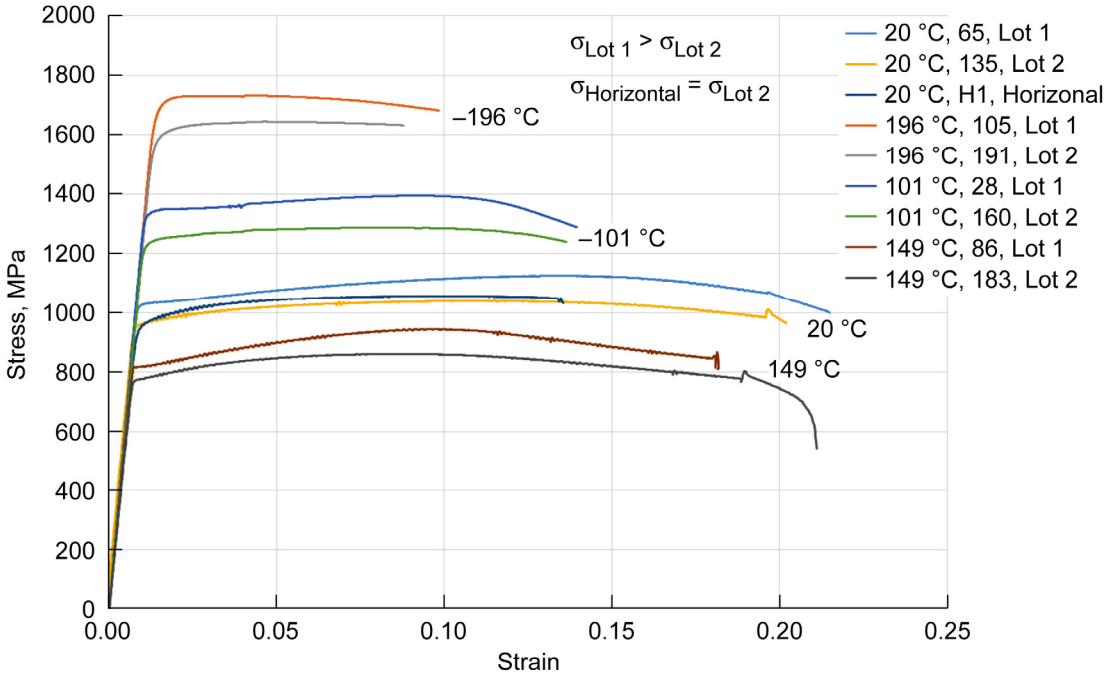

Figure 16.—Representative tensile plots at temperatures from cryogenic to elevated for lots 1 and 2. Horizontal samples were only tested at room temperature.

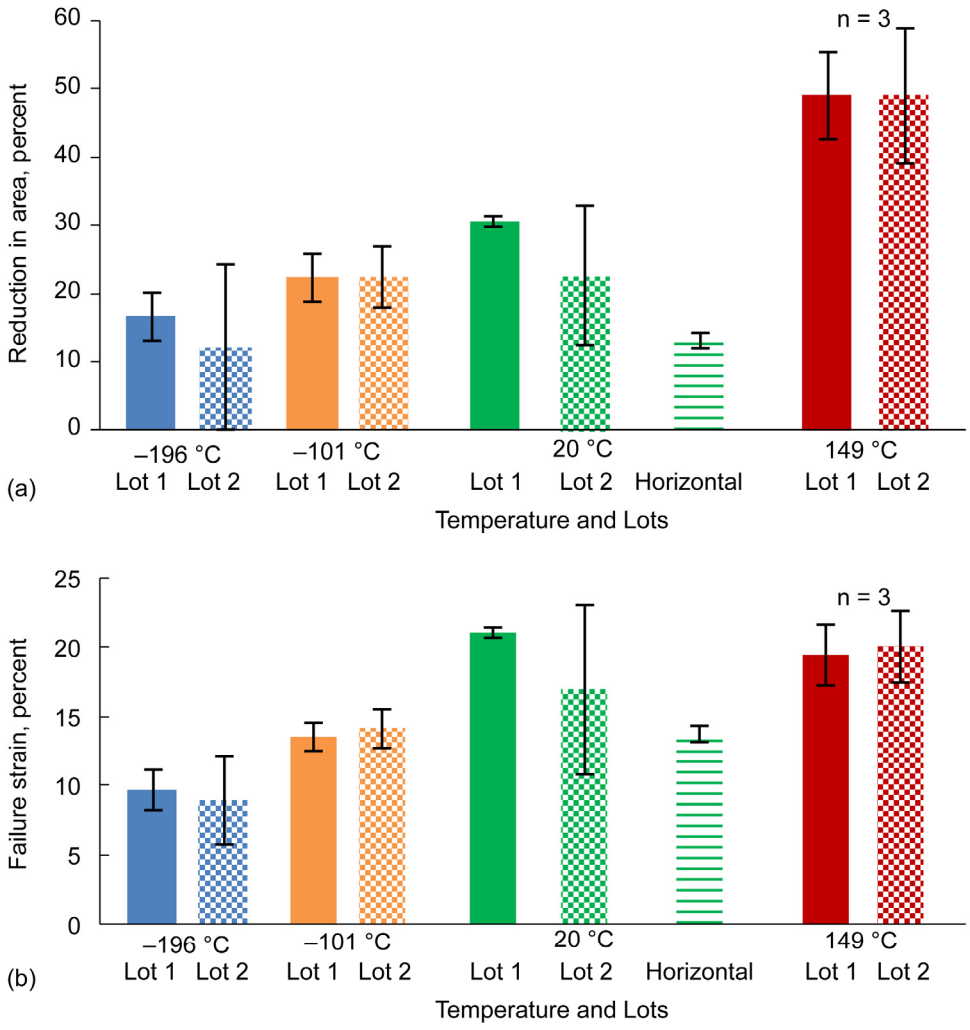

Figure 17.—Plots of (a) failure strain and (b) reduction in area as a function of temperature and sample lots. Error bars represent +/– one standard deviation.

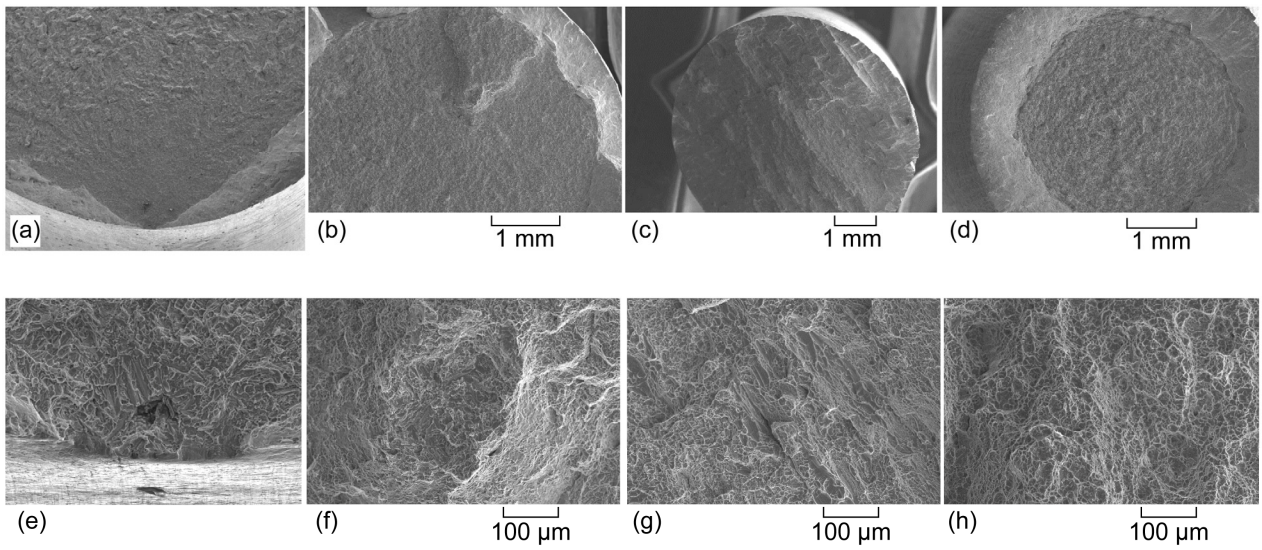

Figure 18.—Typical tensile fracture surfaces at (a,e) –101 °C, (b,f) RT, (c,g) RT horizontal sample, and (d,h) 149 °C.

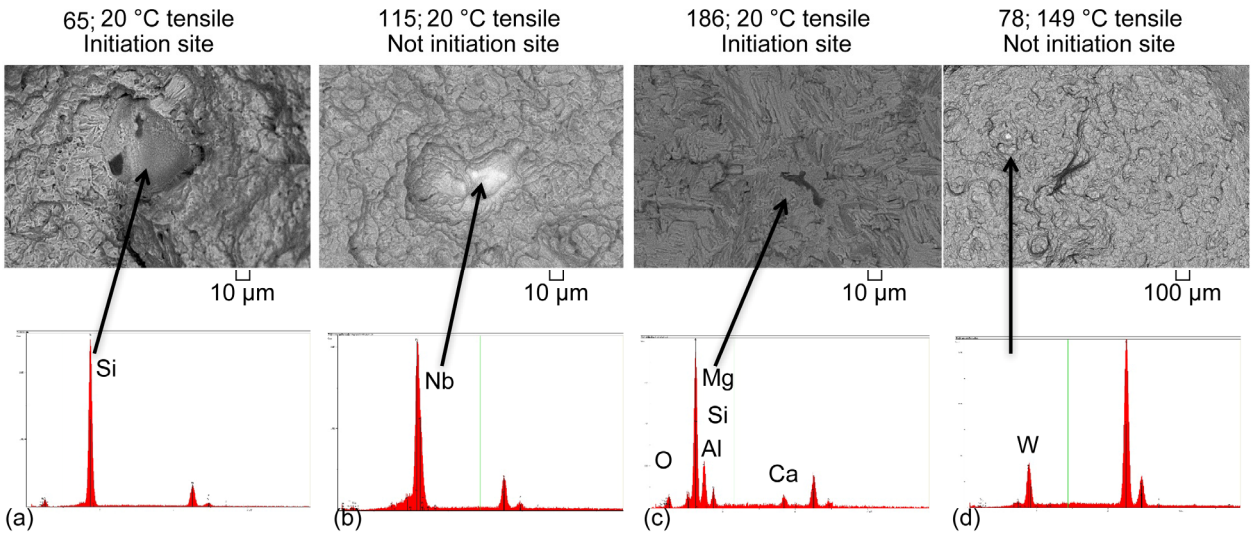

Figure 19.—Tensile fracture surfaces with unusual features. (a) 65 failure initated at a Si inclusion. (b) 115 had a Nb inclusion on the fracture surface although the fracture did not initiate at the inclusion. (c) 186 fracture initiated at a Mg, Si-rich inclusion which was surrounded by a Si-rich area. (d) a W particle was on the fracture surface of 78 but was not the initiation site.

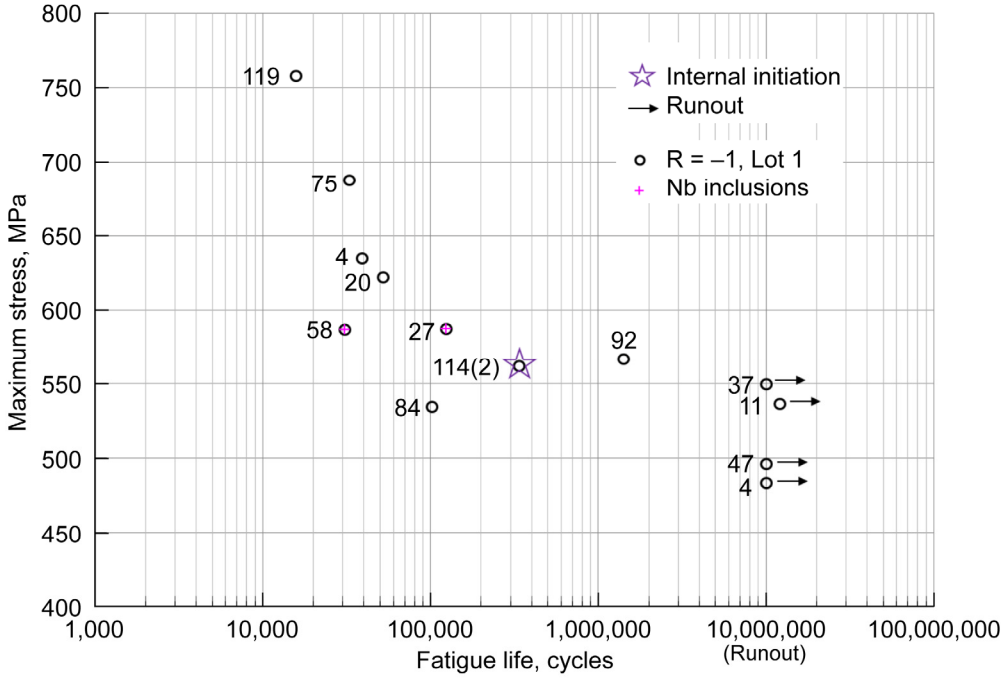

Figure 20.—HCF data for test conditions of 20 °C and R_σ = –1.

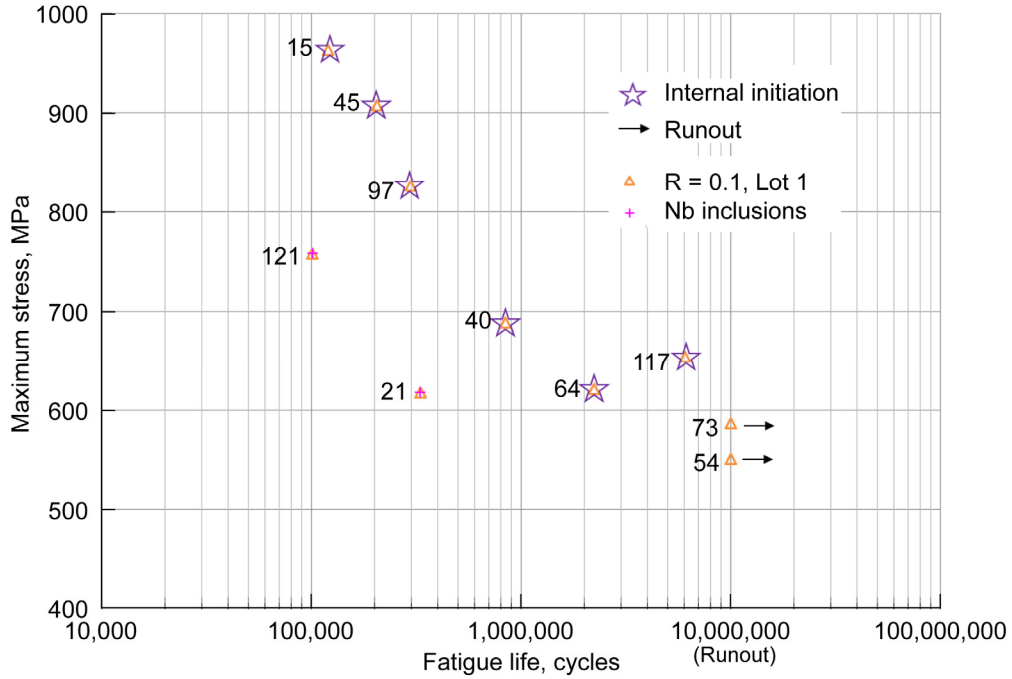

Figure 21.—HCF data for test conditions of 20 °C and R_σ = 0.1.

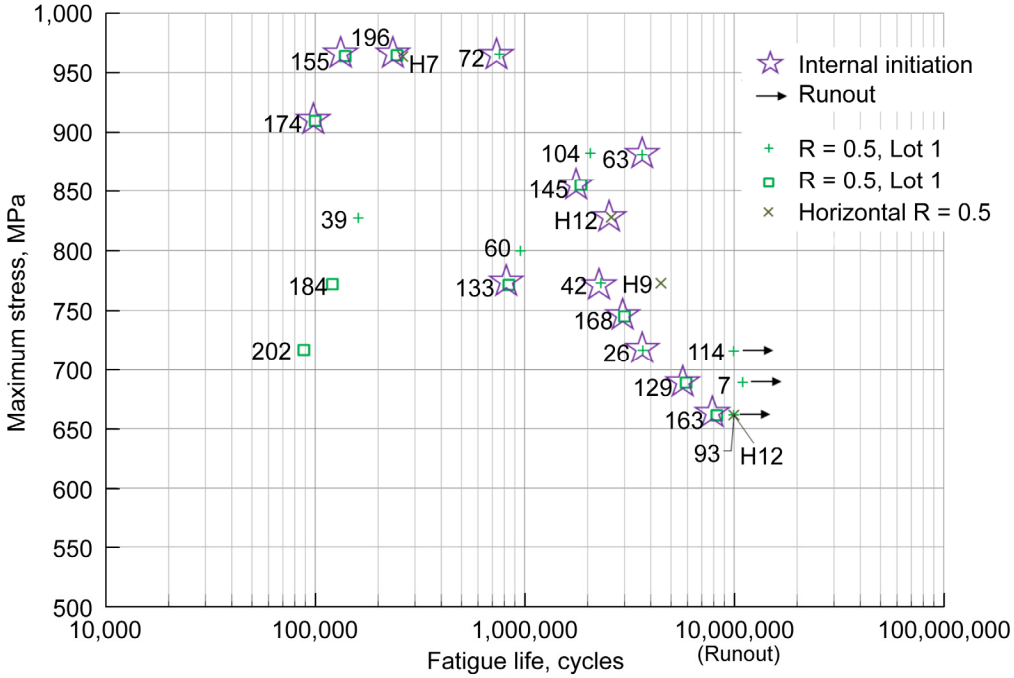

Figure 22.—HCF data for test conditions of 20 °C and R_σ = 0.5.

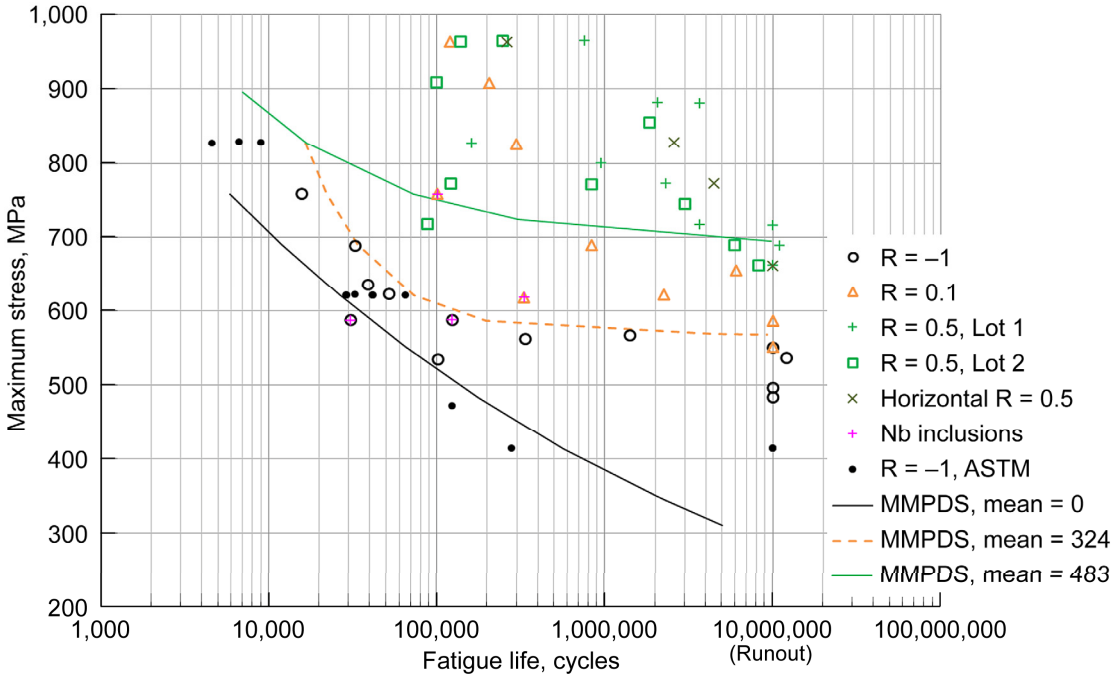

Figure 23.—HCF data for test conditions of 20 °C and various load ratios.

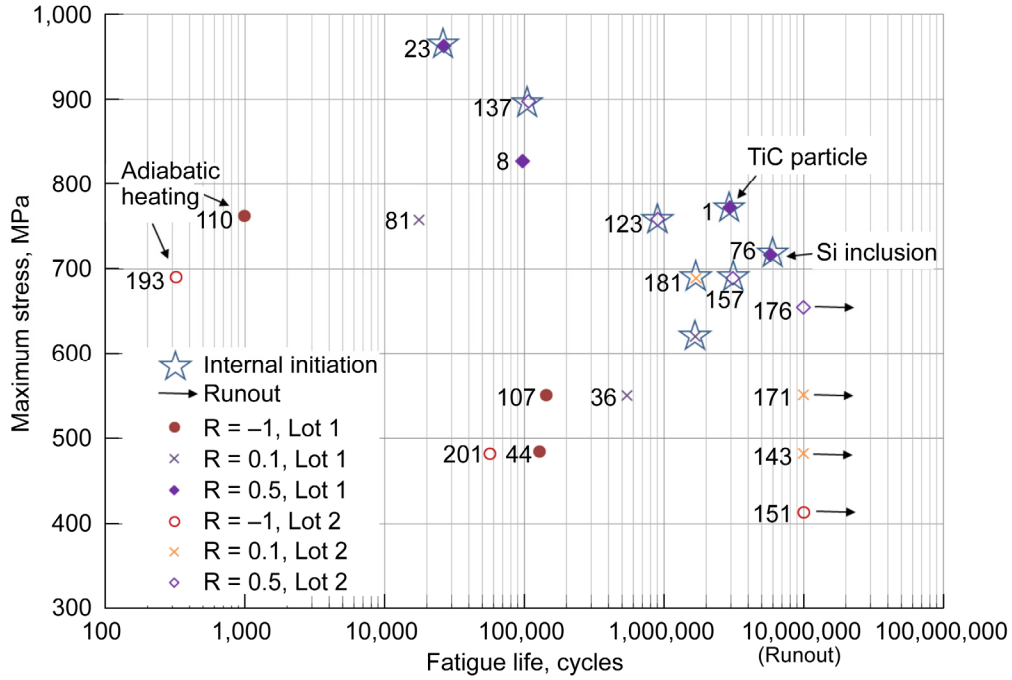

Figure 24.—HCF data for test conditions of 149 °C and various load ratios.

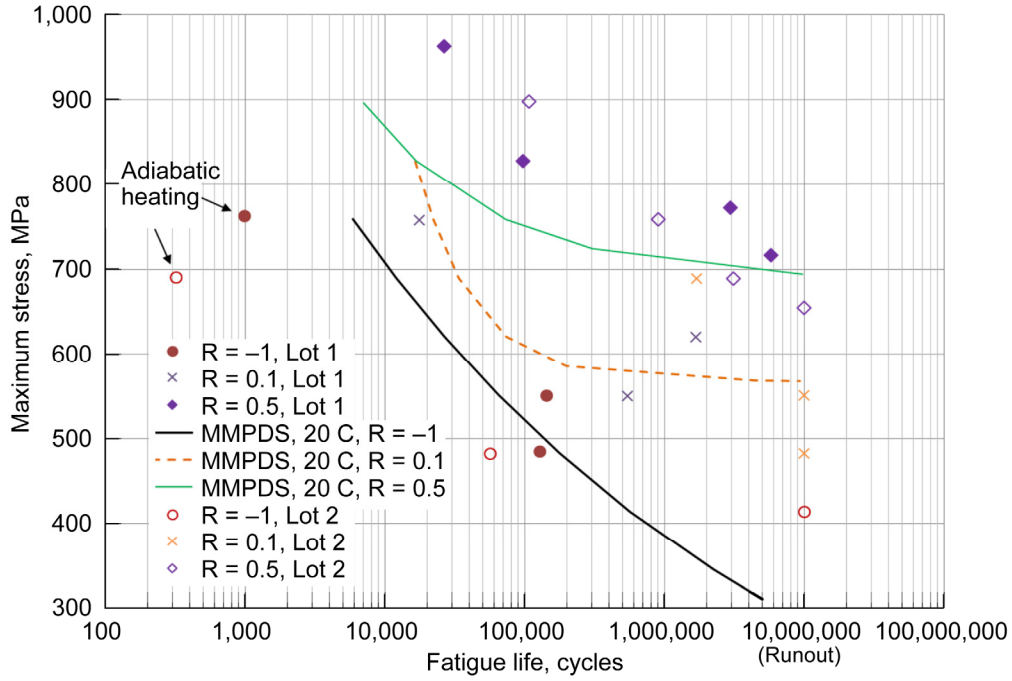

Figure 25.—HCF data for test conditions of 149 °C and various load ratios.

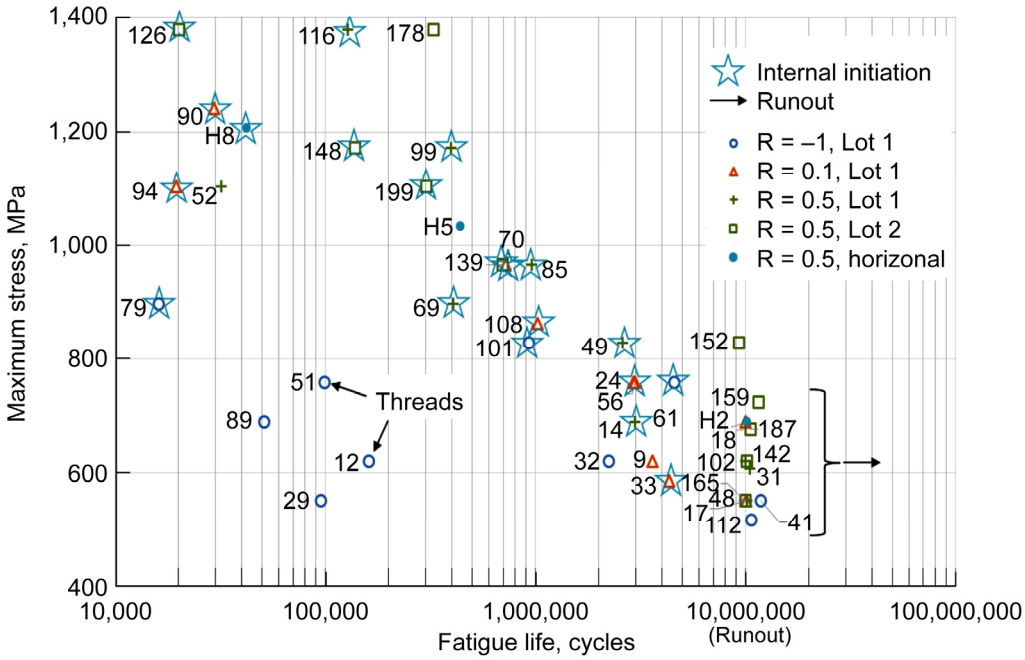

Figure 26.—HCF data for test conditions of –196 °C and various load ratios.

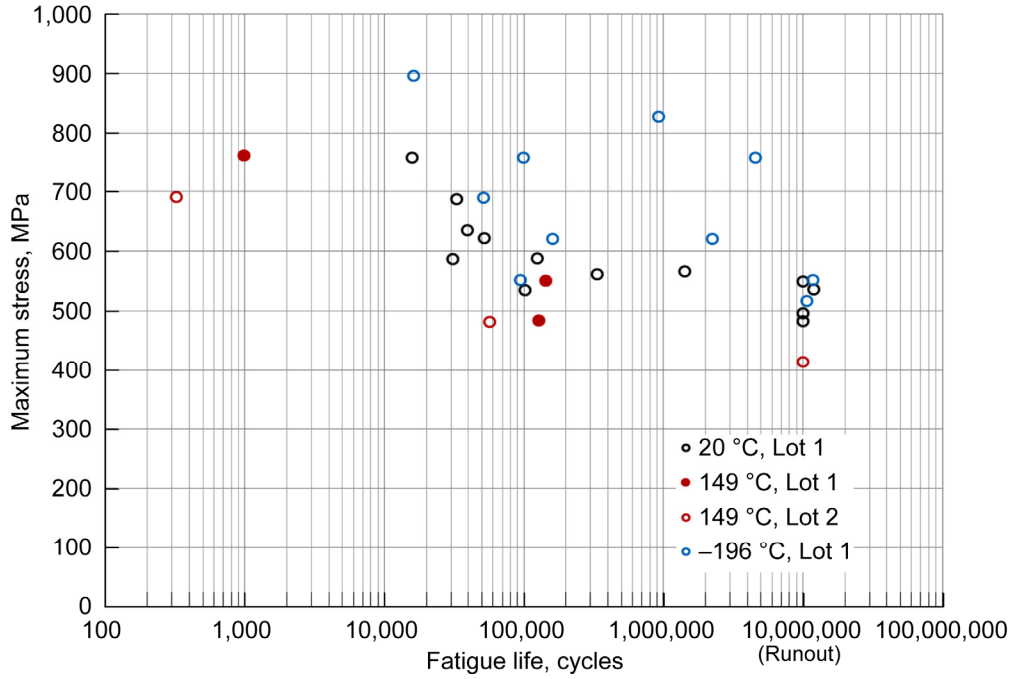

Figure 27.—HCF data for test conditions R_σ = –1 and various temperatures.

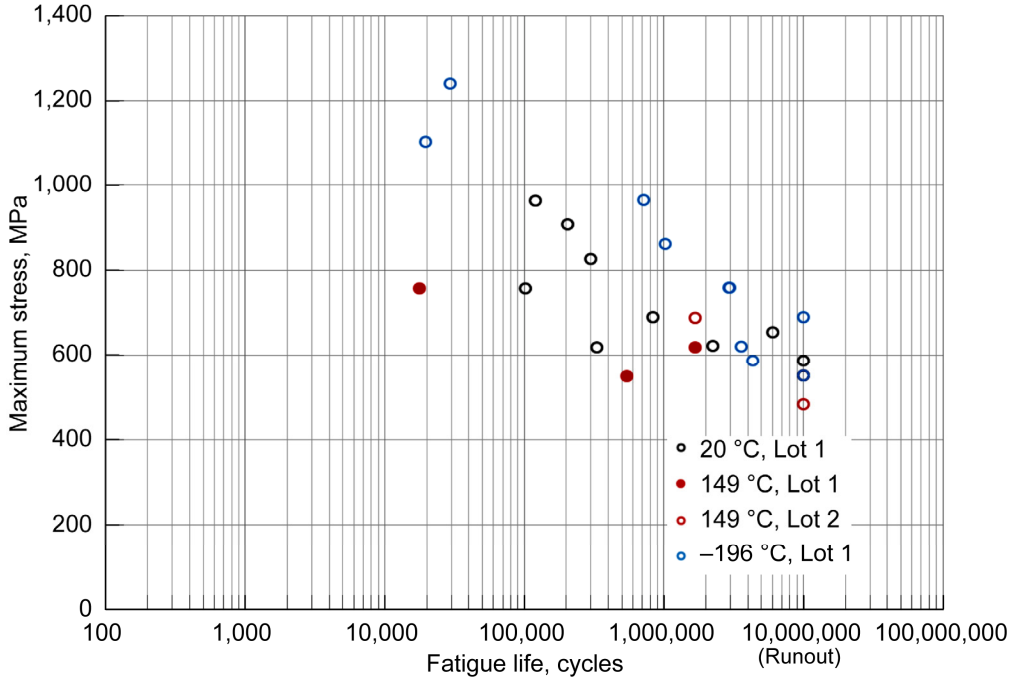

Figure 28.—HCF data for test conditions R_σ = 0.1 and various temperatures.

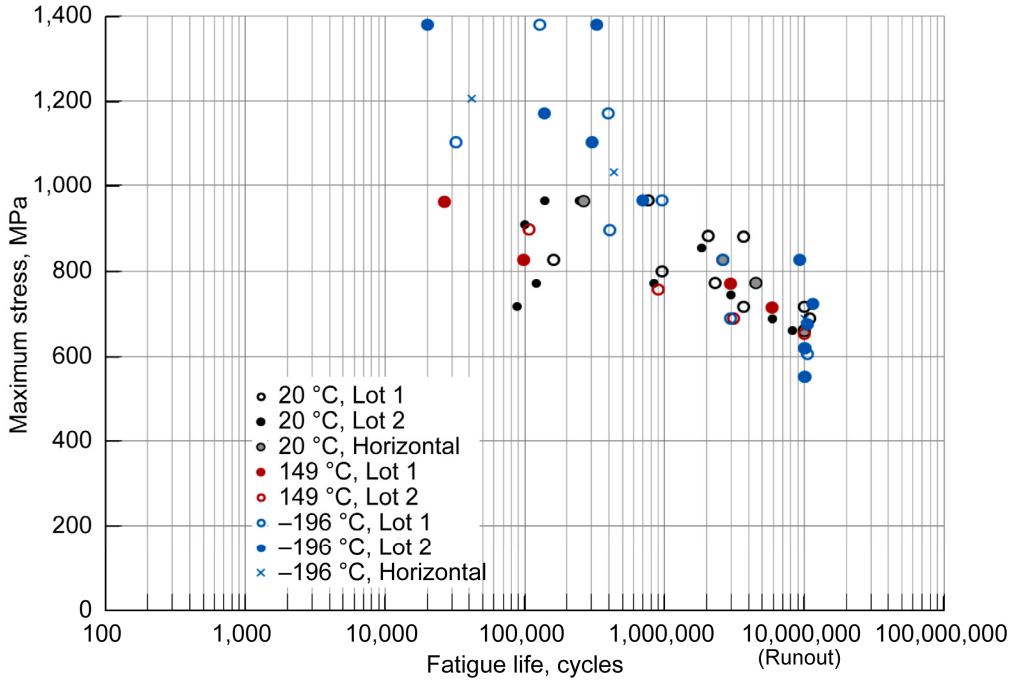

Figure 29.—HCF data for test conditions R_σ = 0.5 and various temperatures.

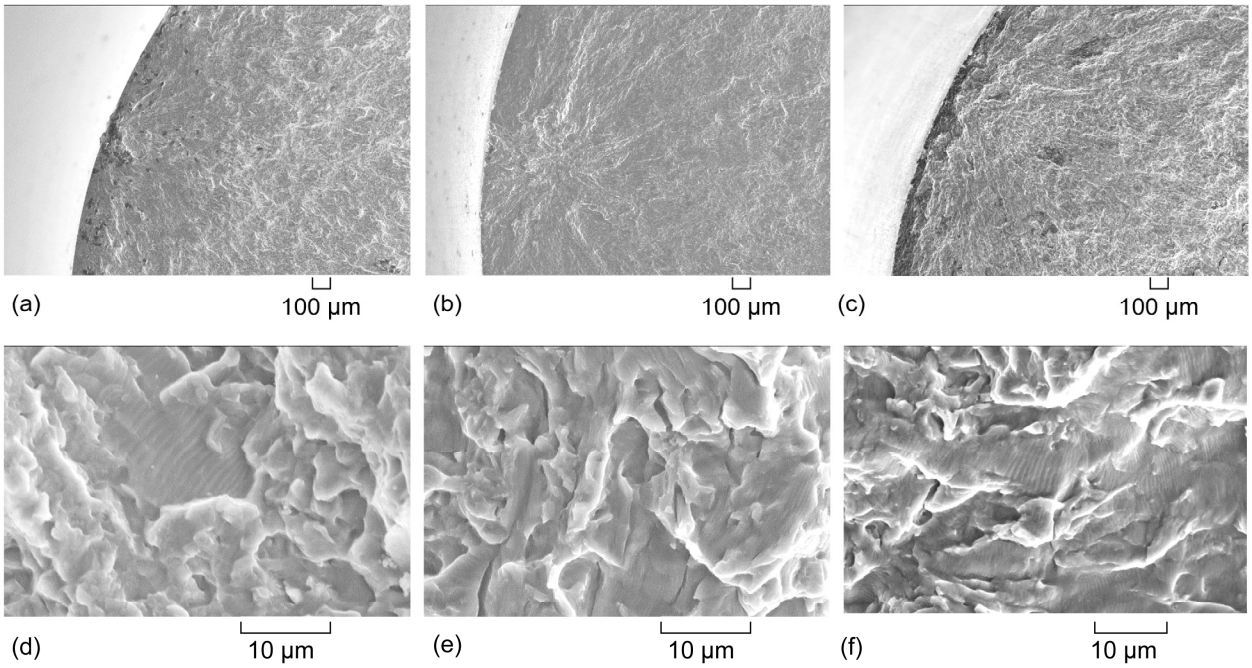

Figure 30.—Typical HCF fracture surfaces at (a,d) –196 °C, surface initiation, (b,e) 20 °C, internal initiation, and (c,f) 149 °C, surface initiation.

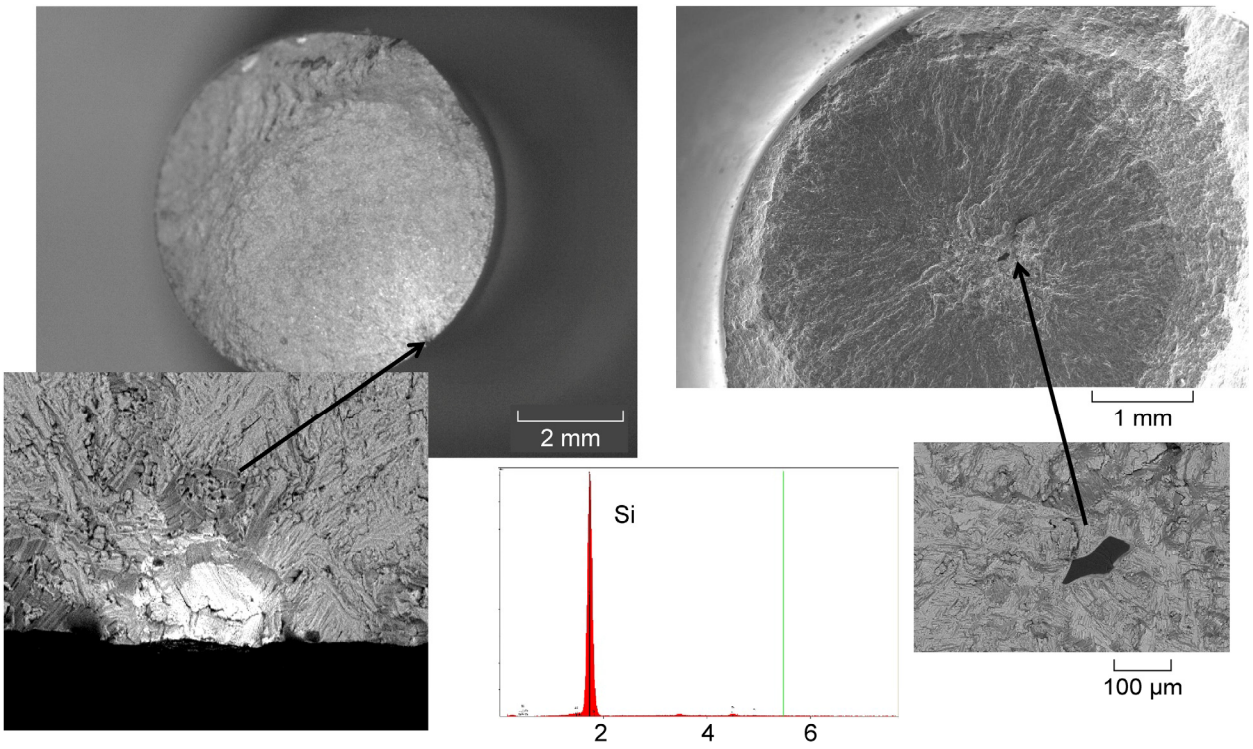

Figure 31.—Unusual HCF fracture surfaces. (a) Sample 121, tested at 20 °C, failed at a Nb inclusion that happened to be at the sample surface. (b) Sample 76, tested at 149 °C, failed at an internal Si-rich inclusion.

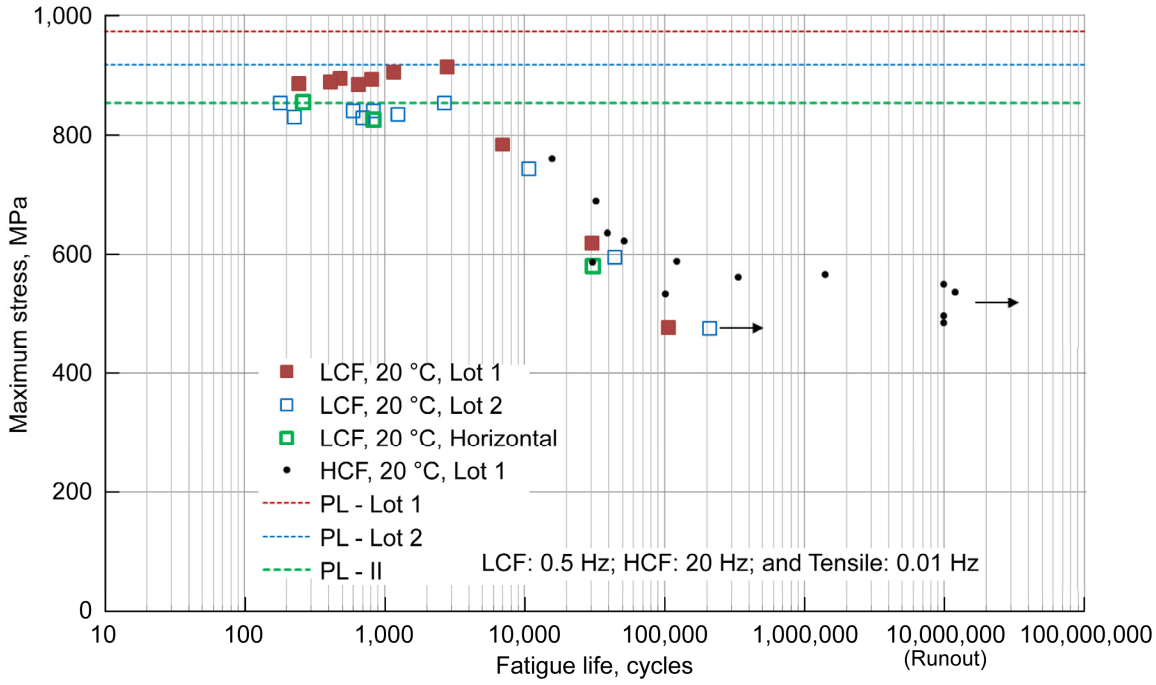

Figure 32.—Fatigue at conditions of 20 °C and fully-reversed loading.

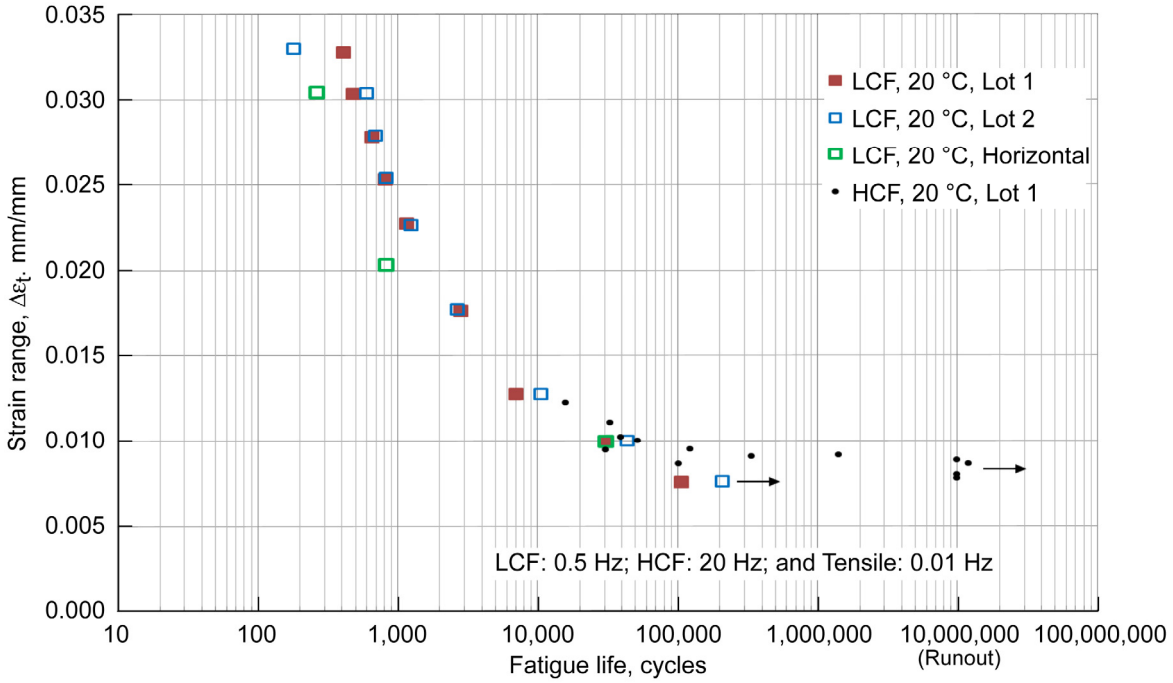

Figure 33.—Fatigue at conditions of 20 °C, R_σ = –1, and fully-reversed loading.

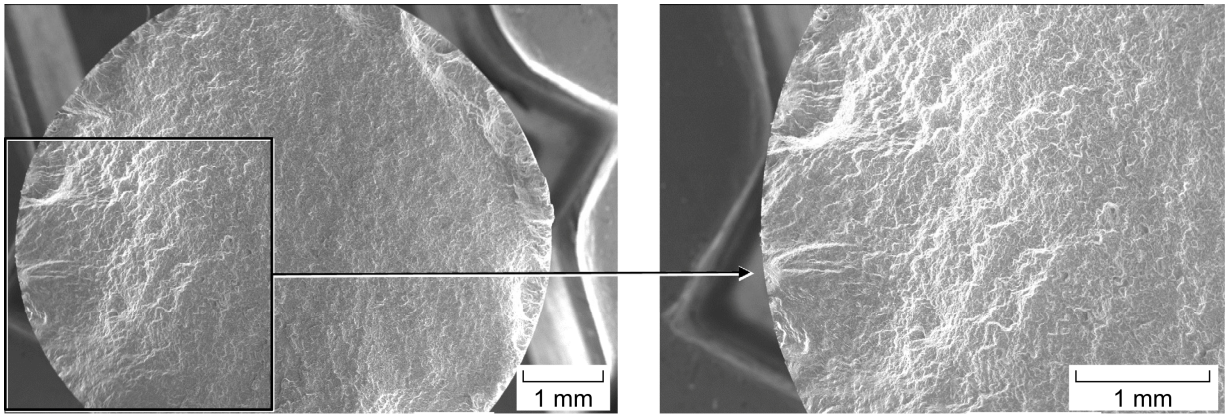

Figure 34.—Surface initiation at multiple sites on sample 106 tested at 20 °C.

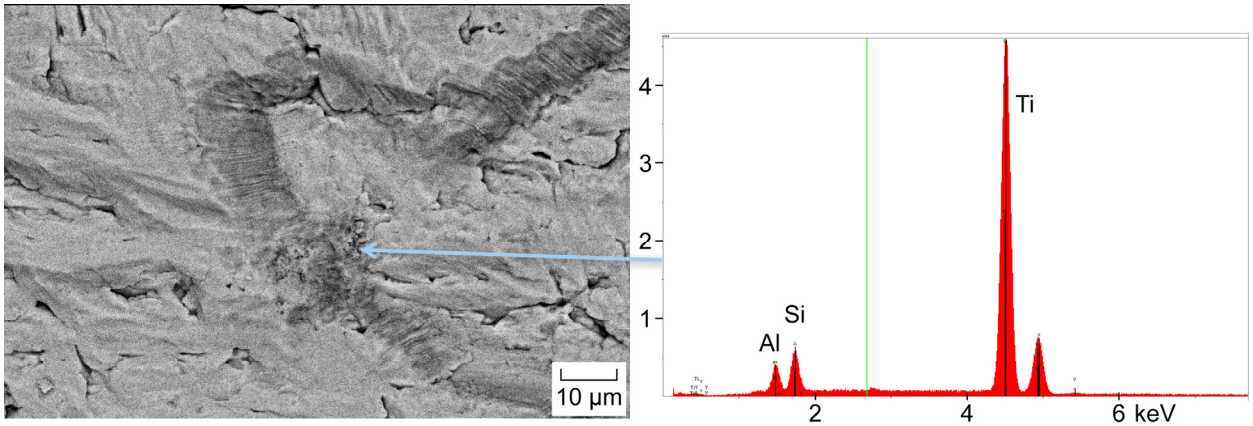

Figure 35.—Initiated failure at an internal site where Si was detected in the microstructure, 20 °C sample 162.

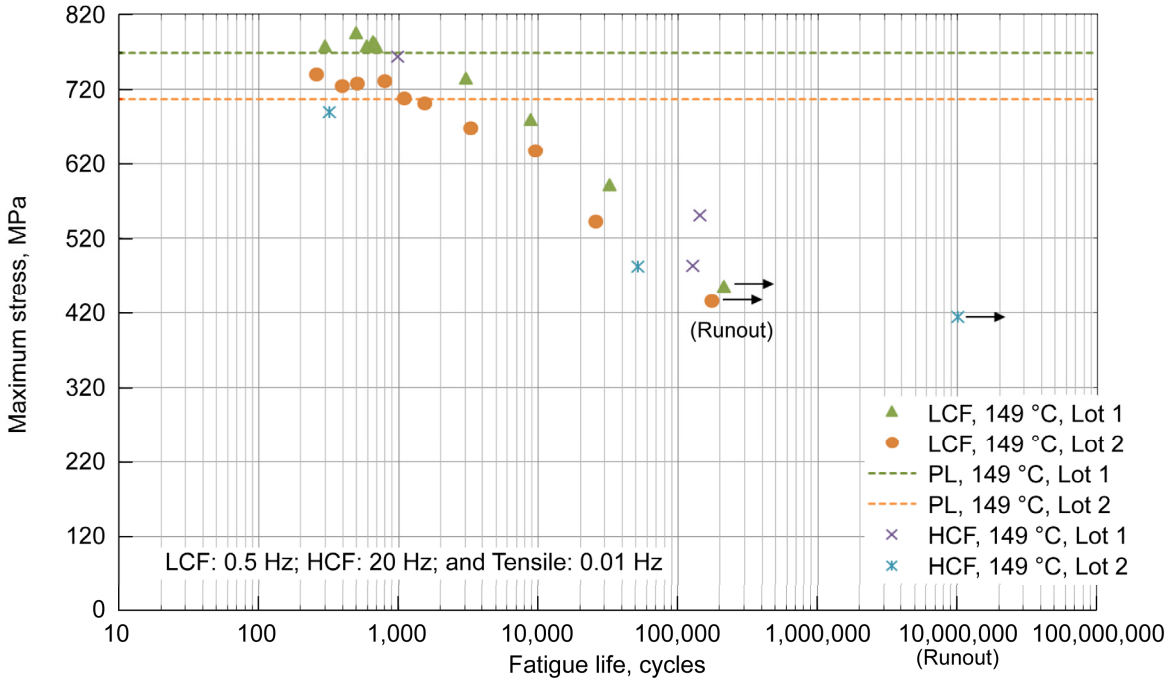

Figure 36.—Fatigue at conditions of 149 °C and fully-reversed loading.

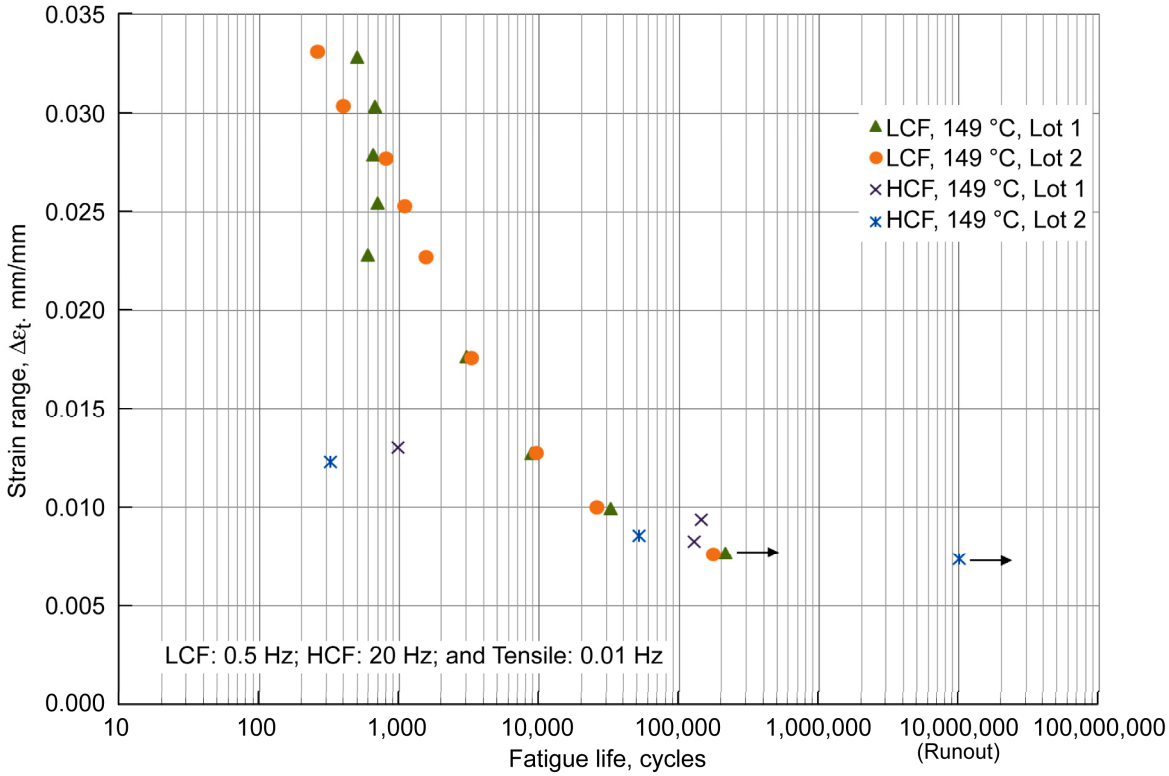

Figure 37.—Fatigue at 149 °C, R_σ = –1, and fully-reversed loading.

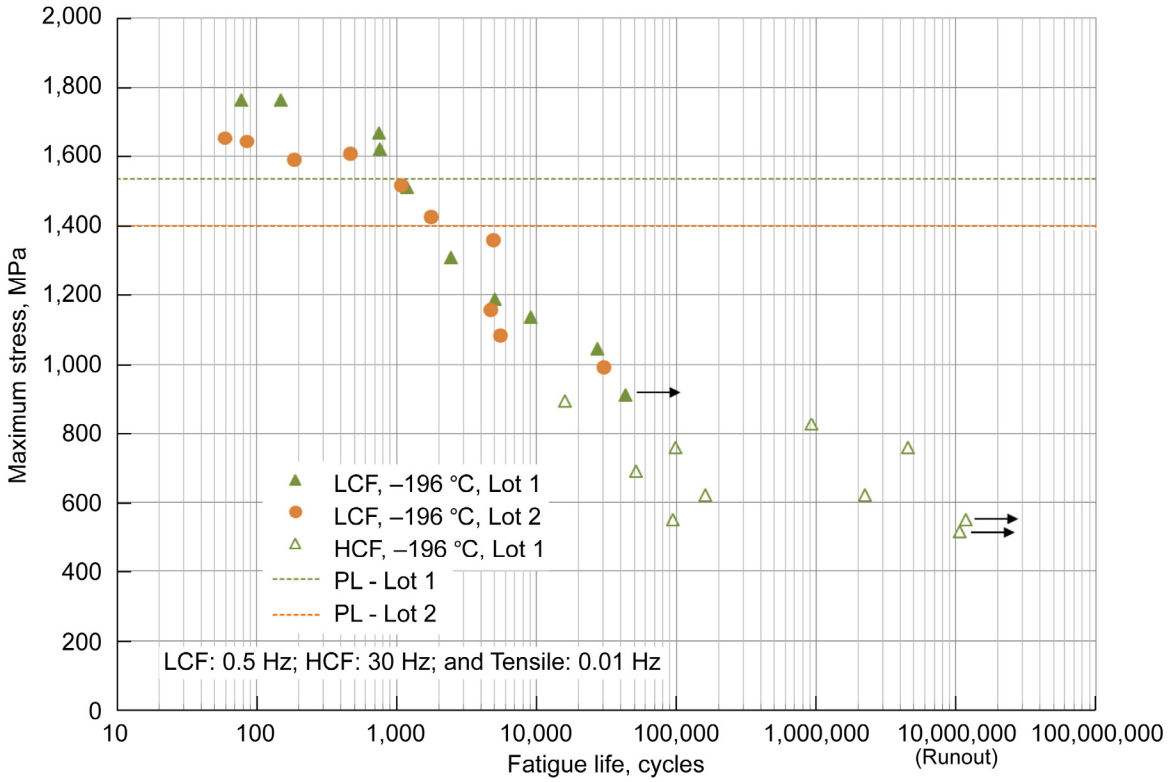

Figure 38.—Fatigue at –196 °C, R_σ = –1, and fully-reversed loading.

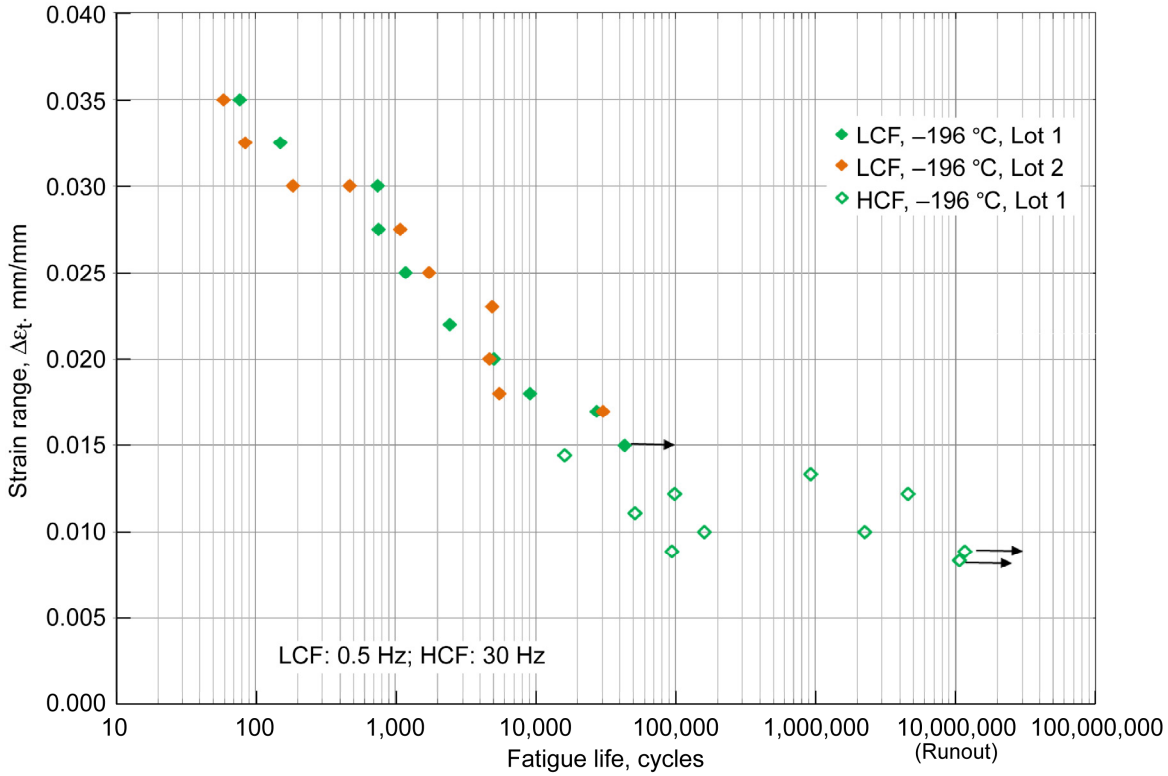

Figure 39.—Fatigue at –196 °C, R_σ = –1, and fully-reversed loading.

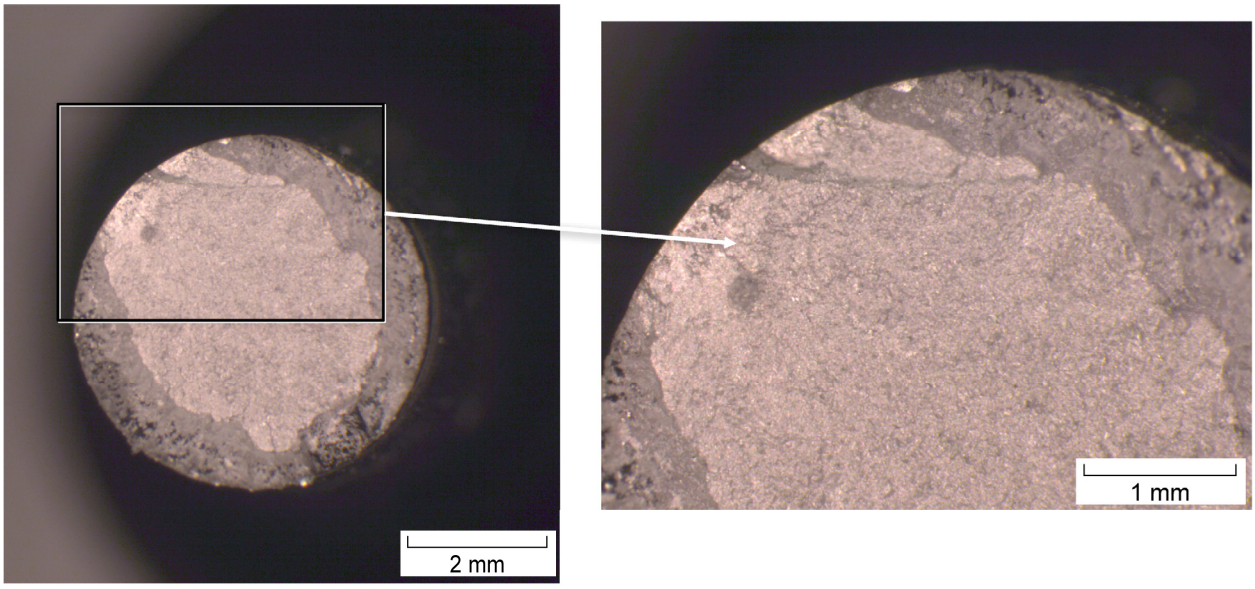

Figure 40.—Optical fractographs of sample 103 tested at –196 °C.

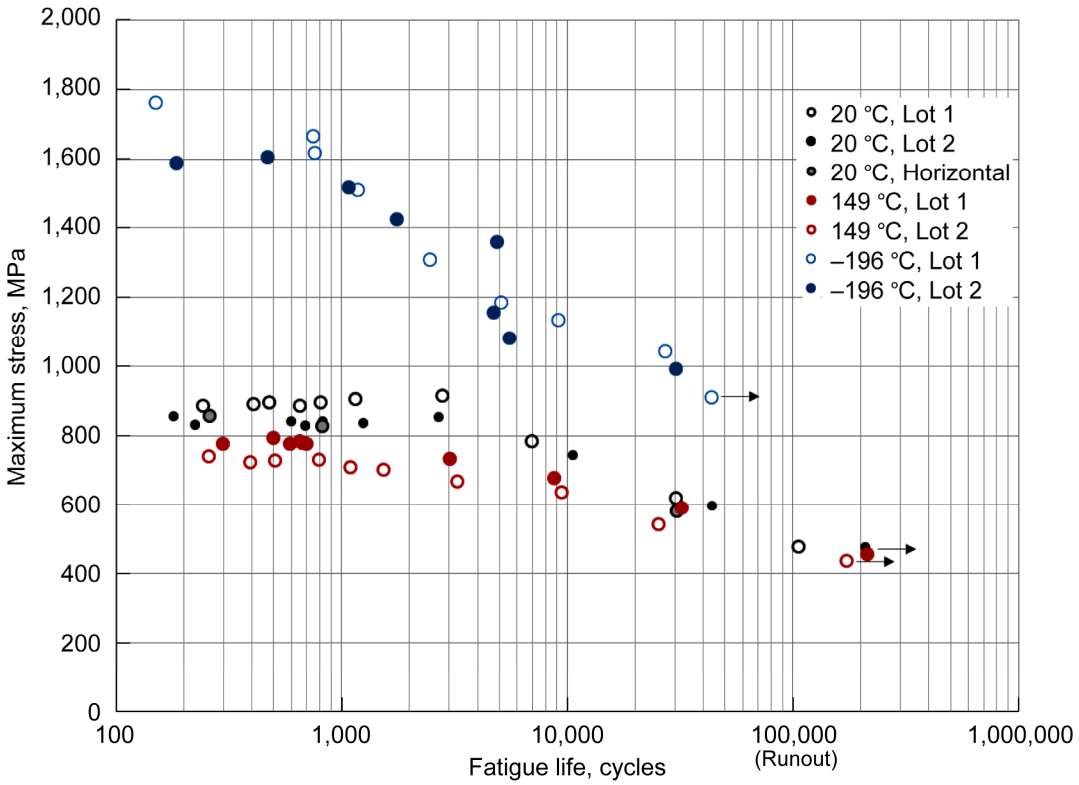

Figure 41.—Fatigue at various temperatures under conditions, R_σ = –1, of fully-reversed loading.

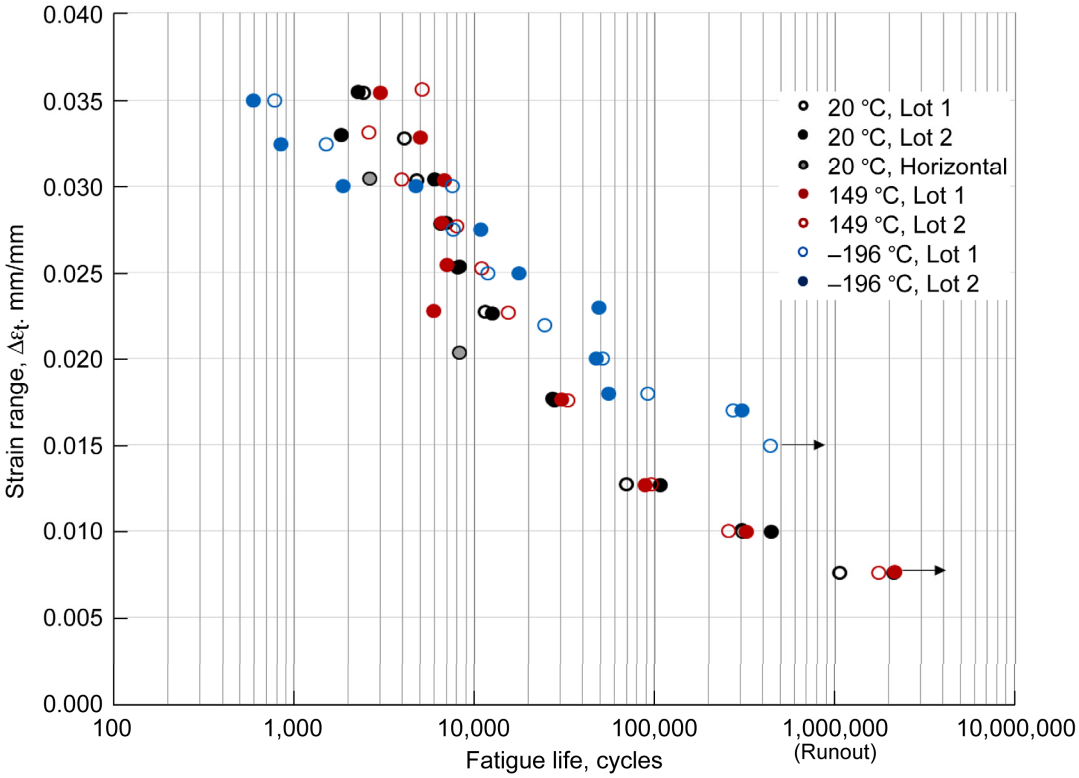

Figure 42.—Fatigue at various temperatures under conditions R_σ = –1 of fully-reversed loading.

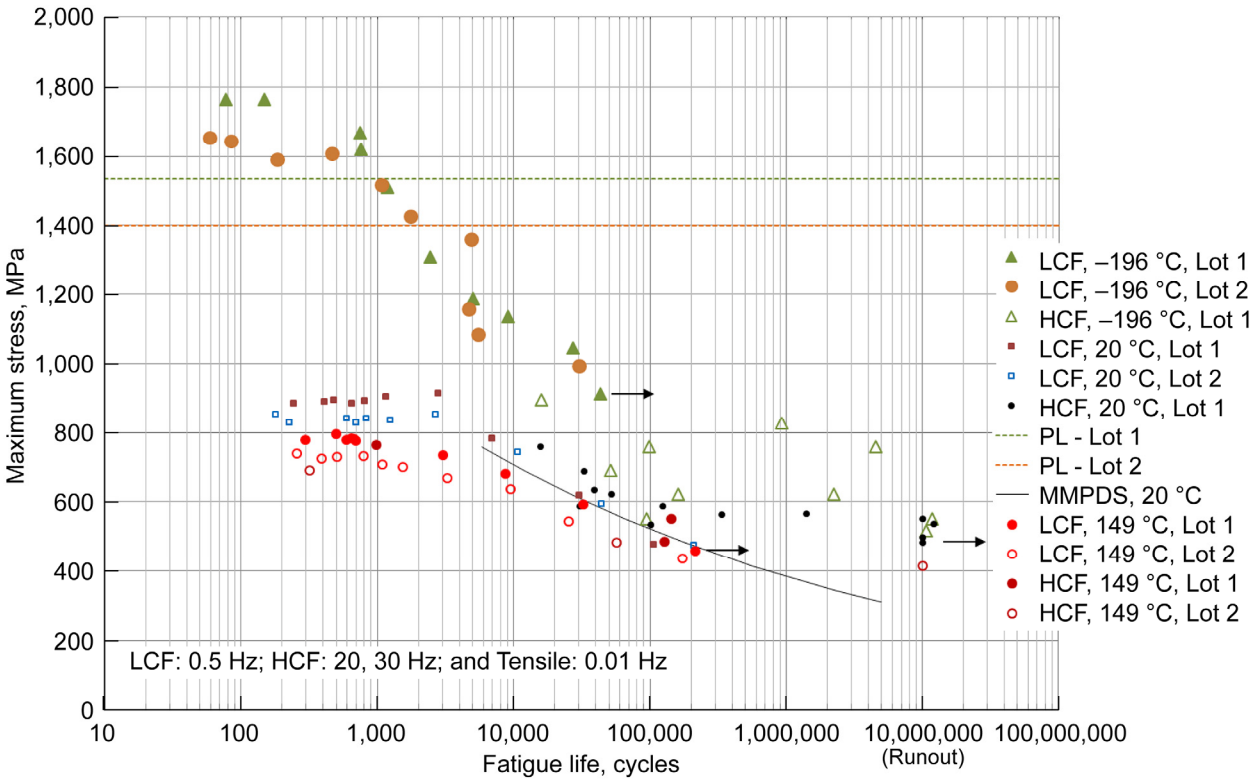

Figure 43.—Fatigue summary at various temperatures under conditions of R_σ = –1 and fully-reversed loading.

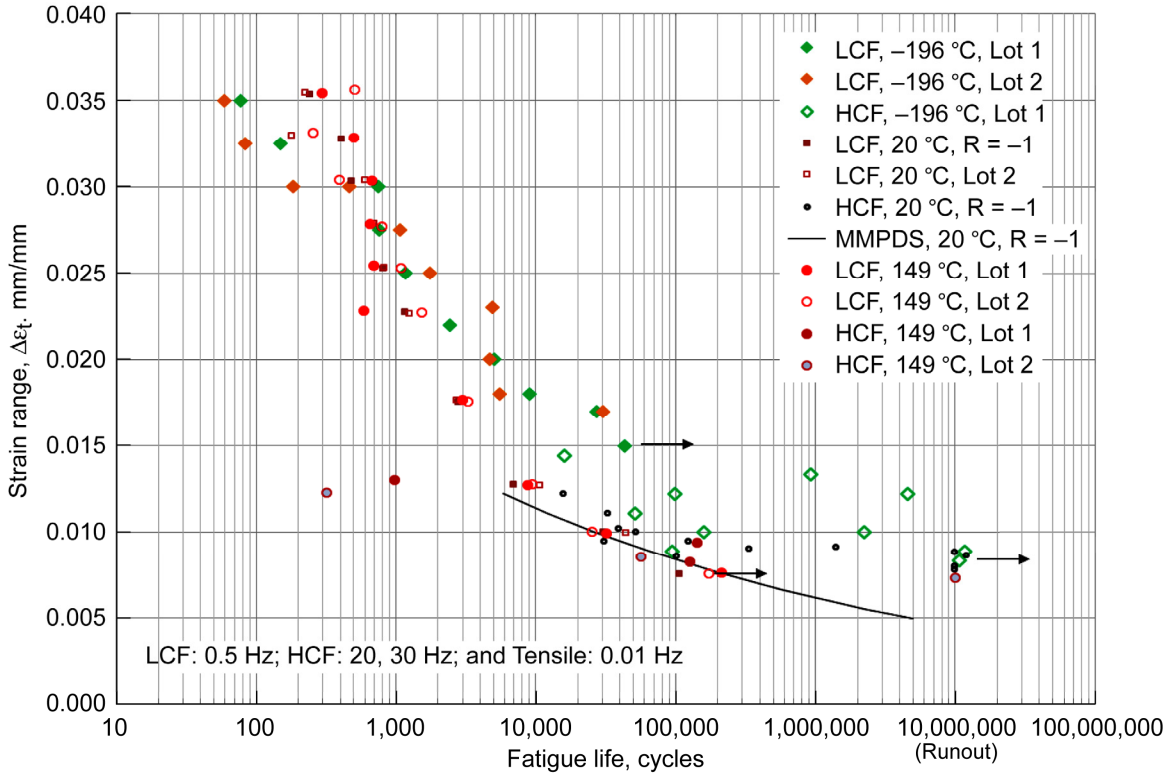

Figure 44.—Fatigue at various temperatures under conditions R_σ = –1 of fully-reversed loading.

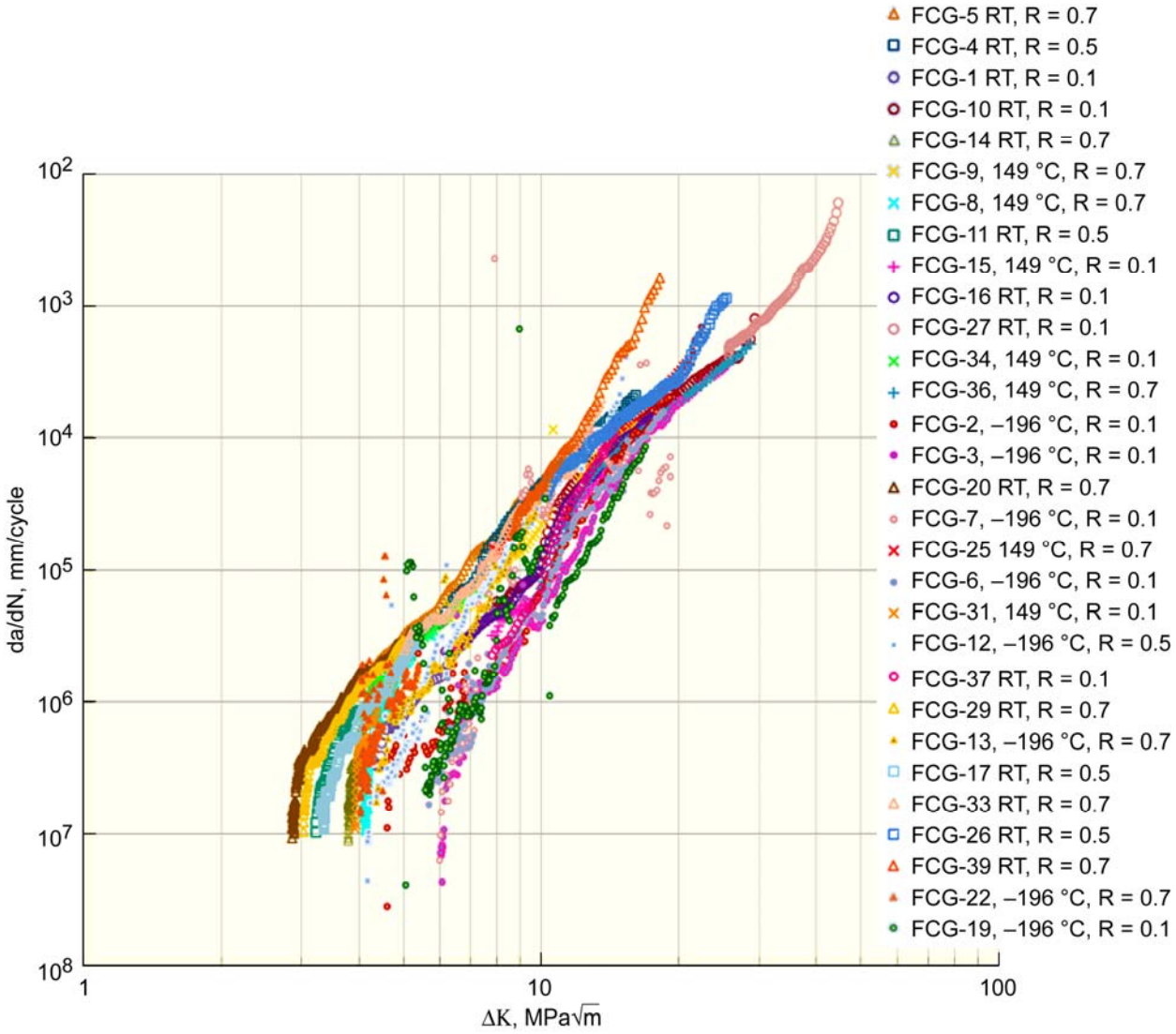

Figure 45.—Fatigue crack growth test results for all test conditions.

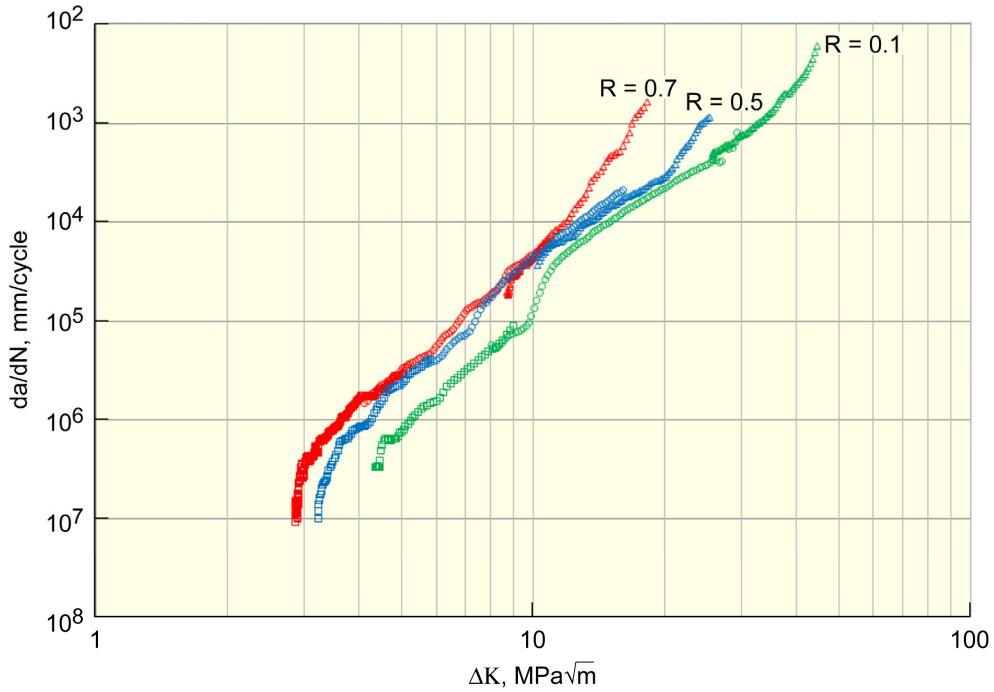

Figure 46.—Fatigue crack growth rates at room temperature at load ratios of 0.1, 0.5, and 0.7.

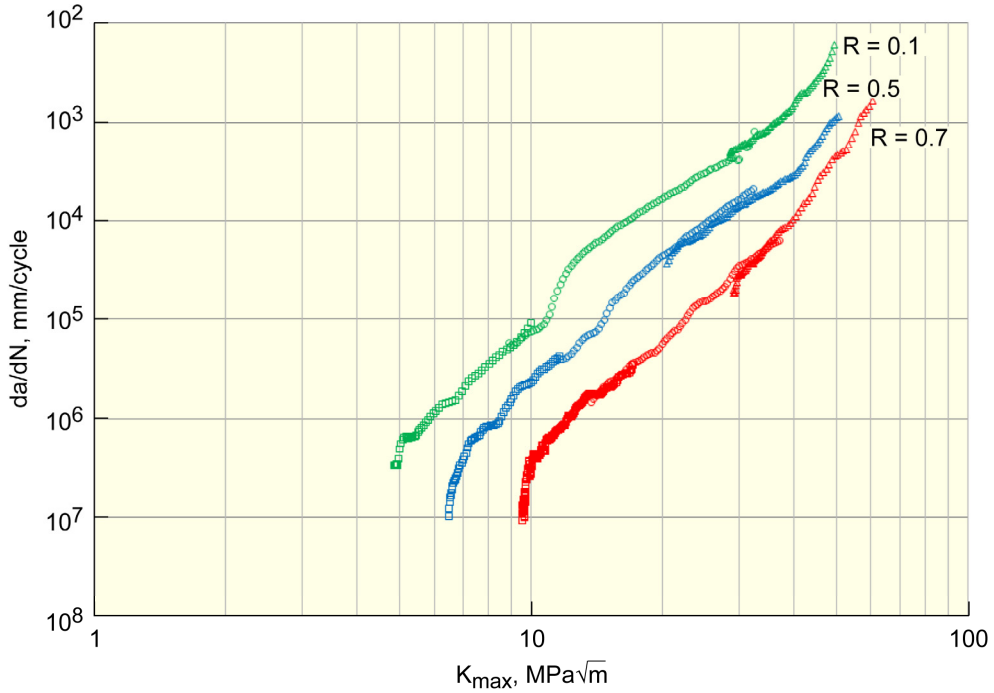

Figure 47.—Room temperature FCG data plotted in terms of the K_{max} stress intensity parameter.

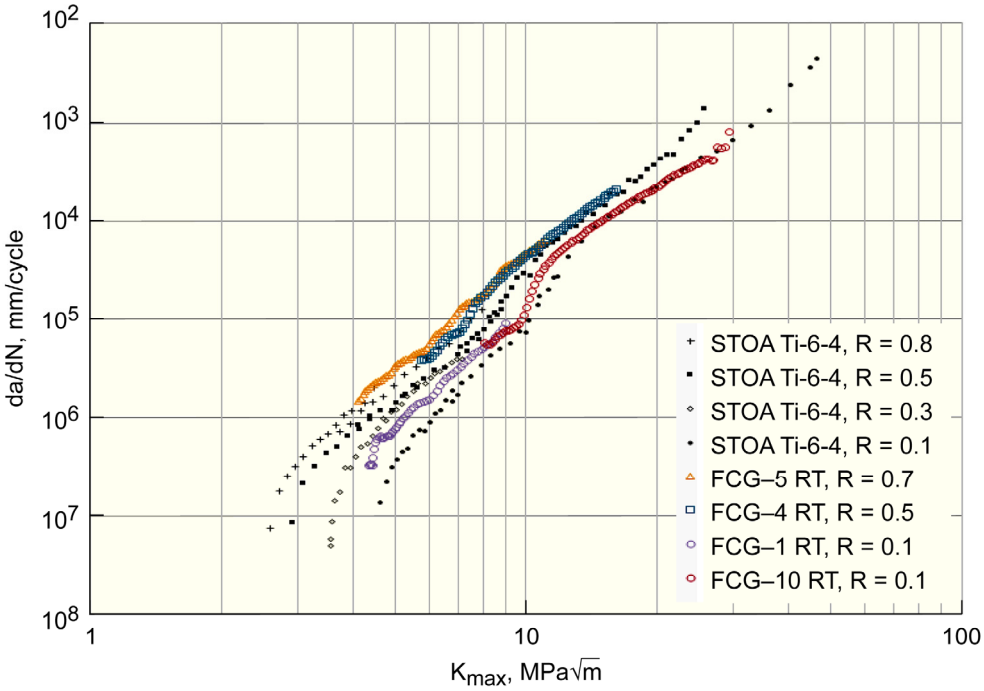

Figure 48.—Comparison of room temperature FCG behavior between AM Ti-6-4 and conventionally produced solution treated and over aged Ti-6-4 at various R ratios (Ref. 17).

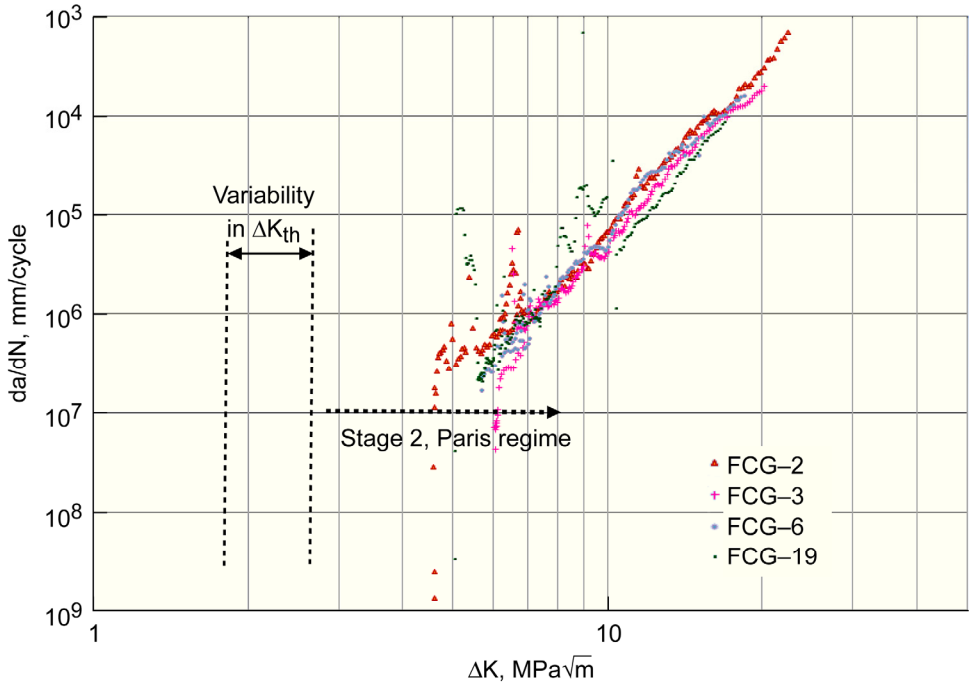

Figure 49.—Cryogenic fatigue crack growth results at R = 0.1, –196 °C.

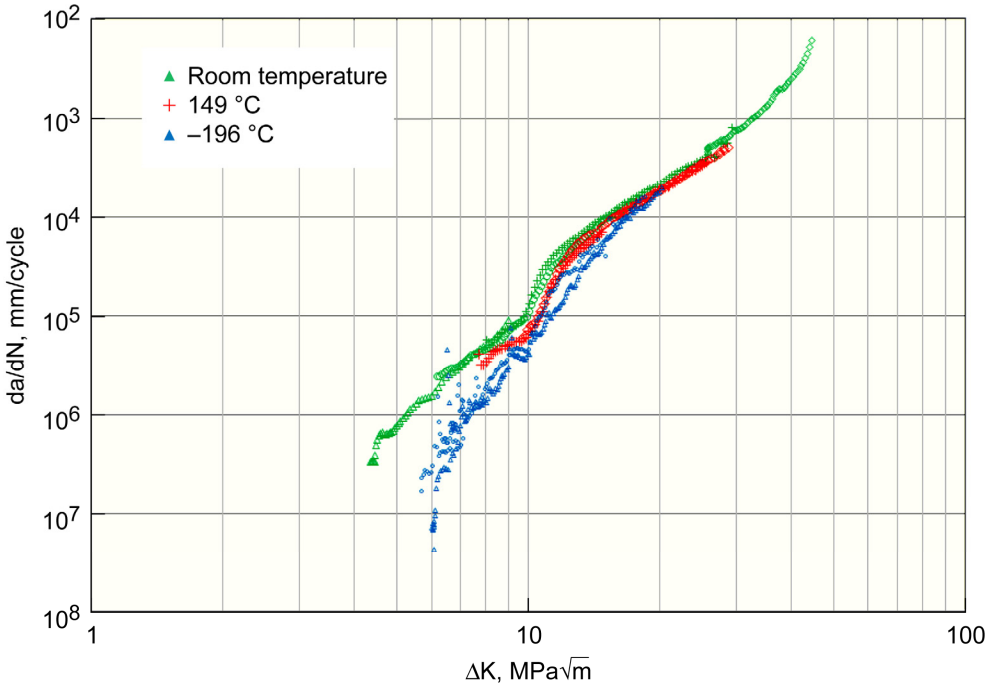

Figure 50.—Fatigue crack growth rates at load ratio R = 0.1 at –196, –20, and 149 °C.

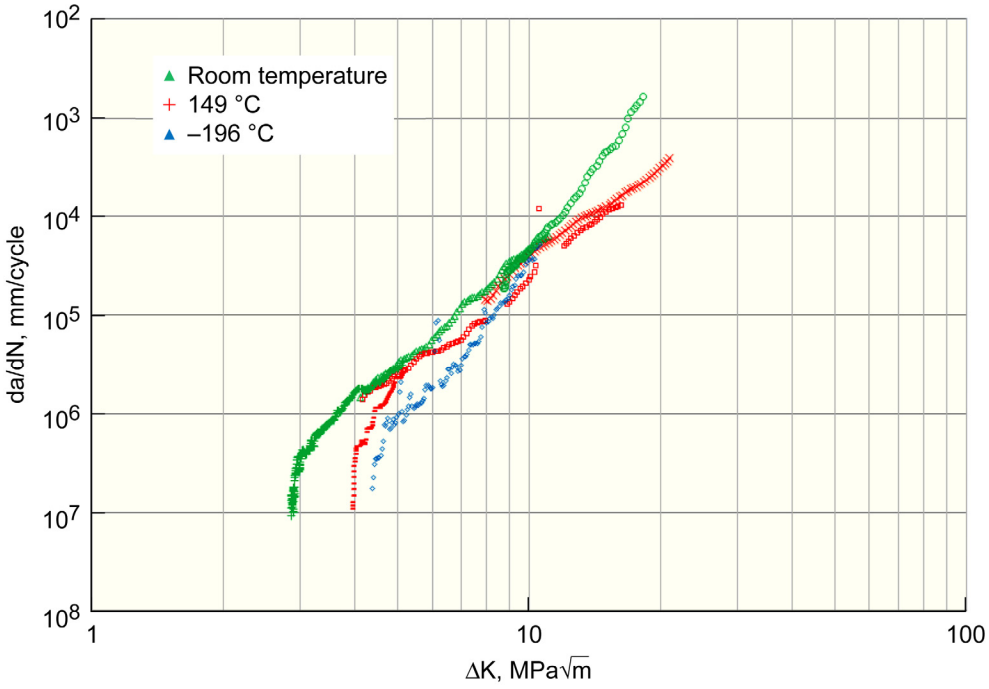

Figure 51.—Fatigue crack growth rates at load ratio R = 0.7 at –196, –20, and 149 °C.

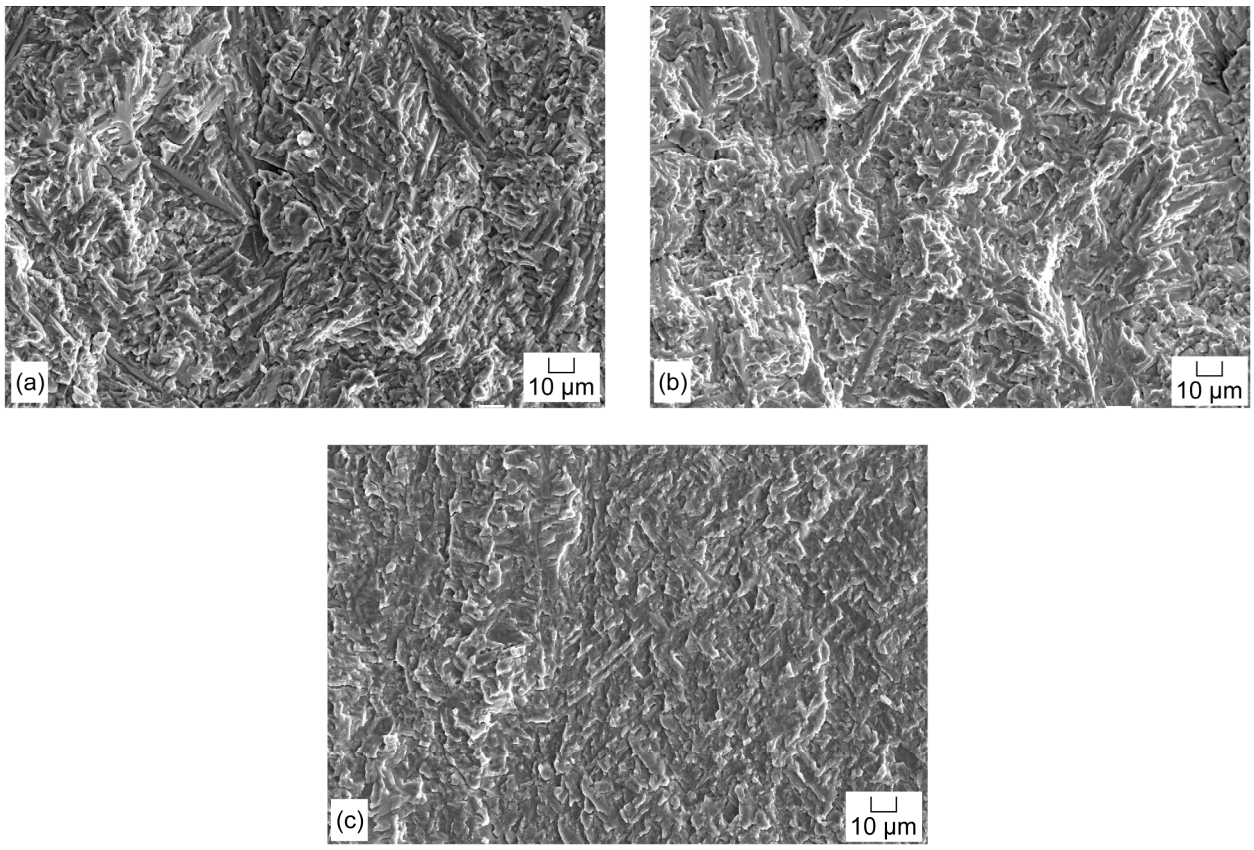

Figure 52.—Representative images of the failure mode at R = 0.1. (a) –196 °C. (b) 20 °C. (c) 149 °C.

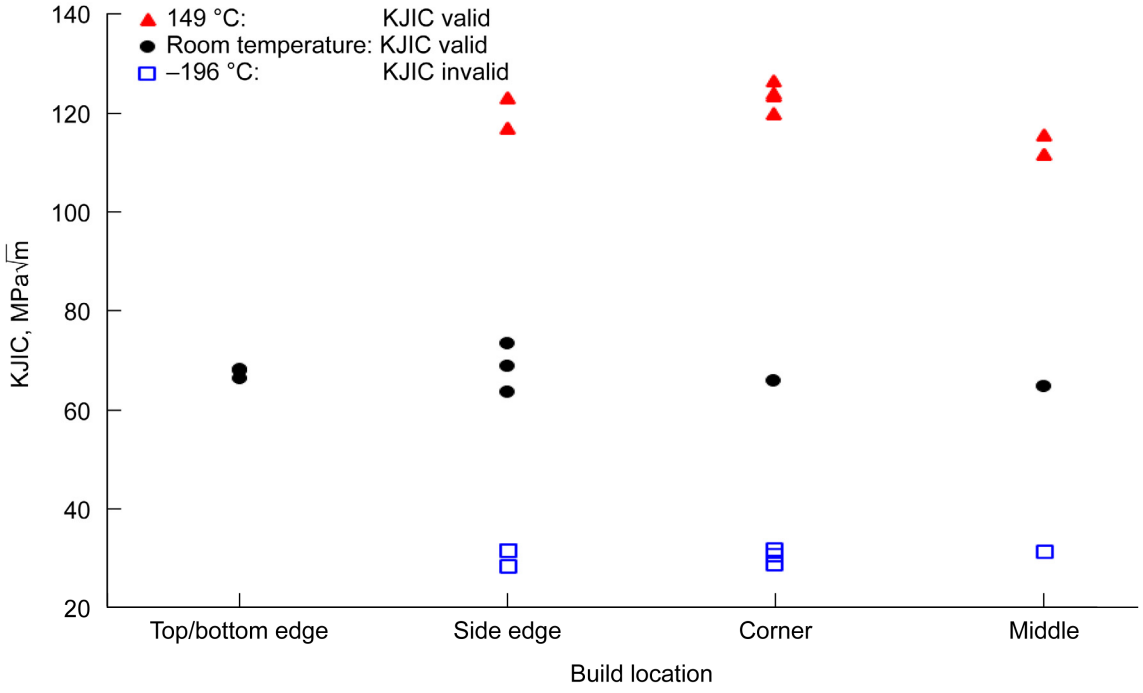

Figure 53.—Distribution of KJIC by manufactured location on the build table as a function of test temperature.

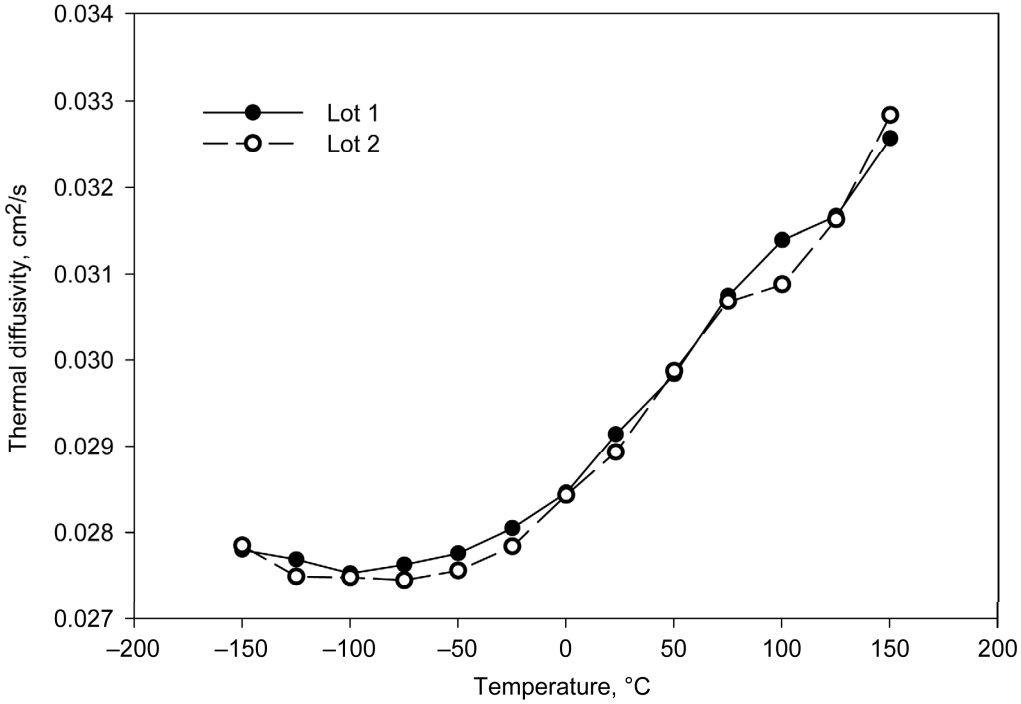

Figure 54.—Thermal diffusivity as a function of temperature for both lots of EBM Ti-6Al-4V.

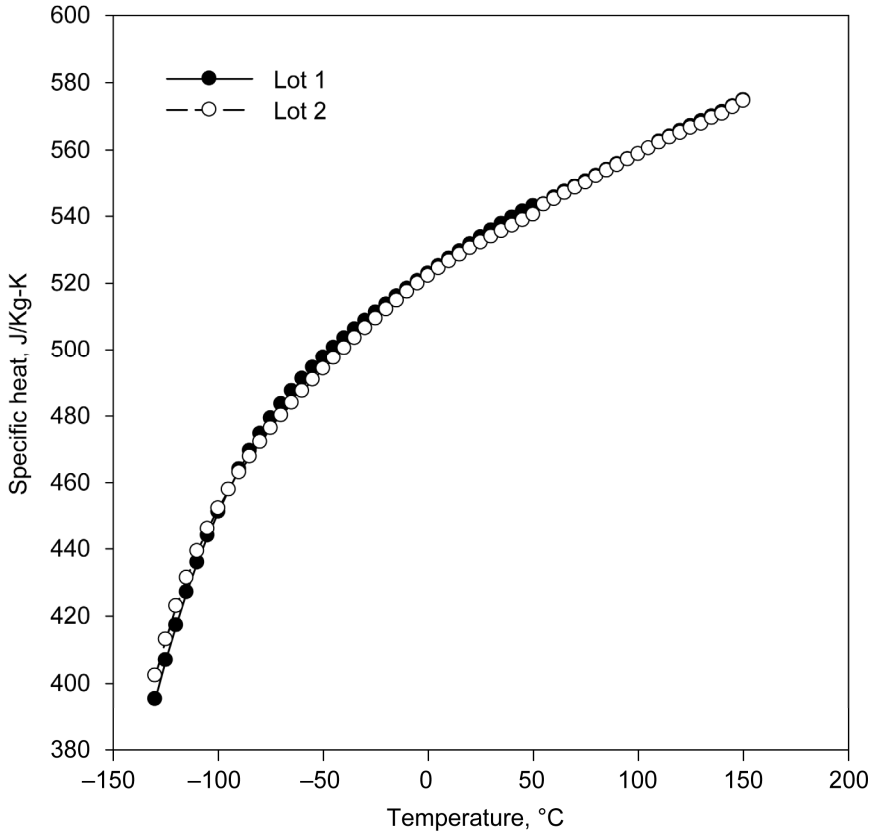

Figure 55.—Specific heat as a function of temperature for both lots of EBM Ti-6Al-4V.

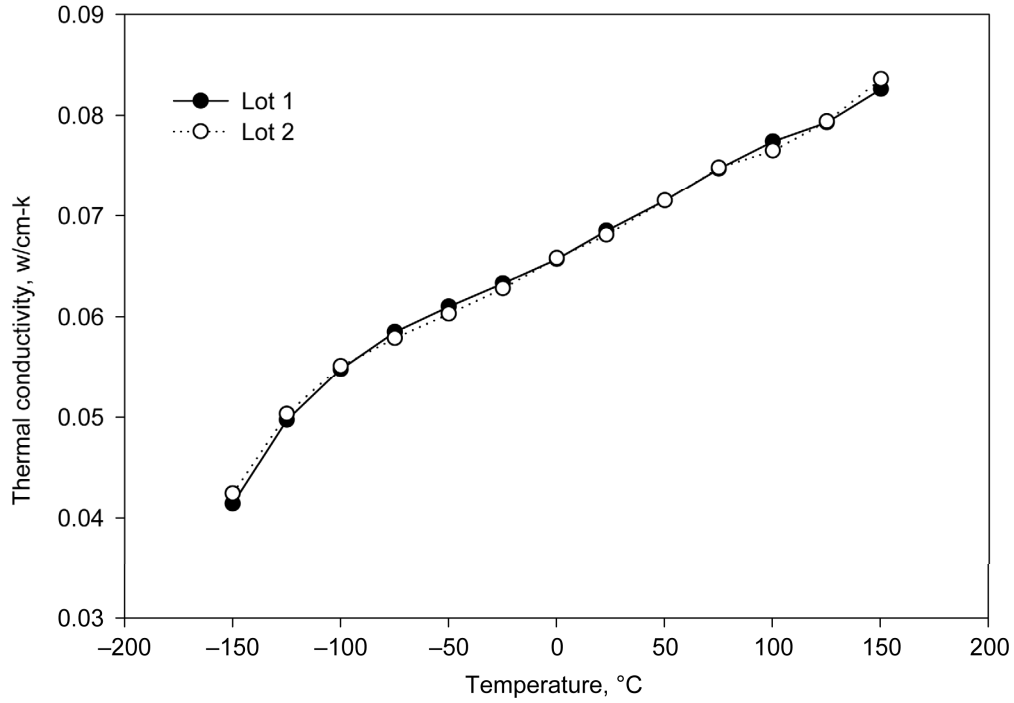

Figure 56.—Thermal conductivity as a function of temperature for both lots of EBM Ti-6Al-4V.

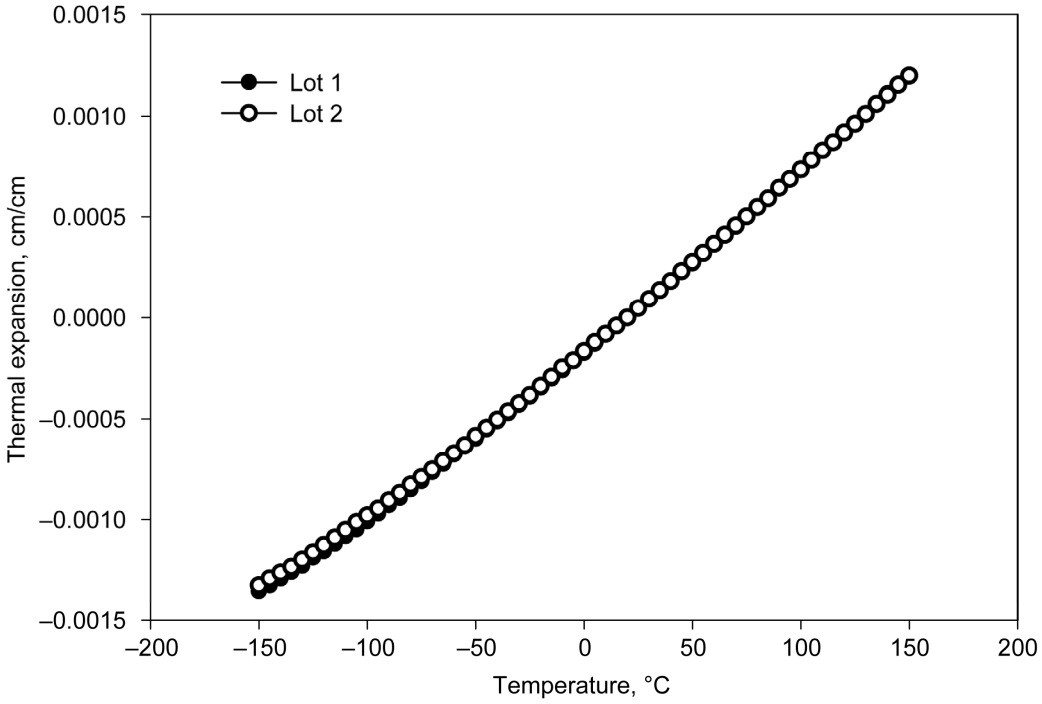

Figure 57.—Thermal expansion as a function of temperature for both lots of EBM Ti-6Al-4V.

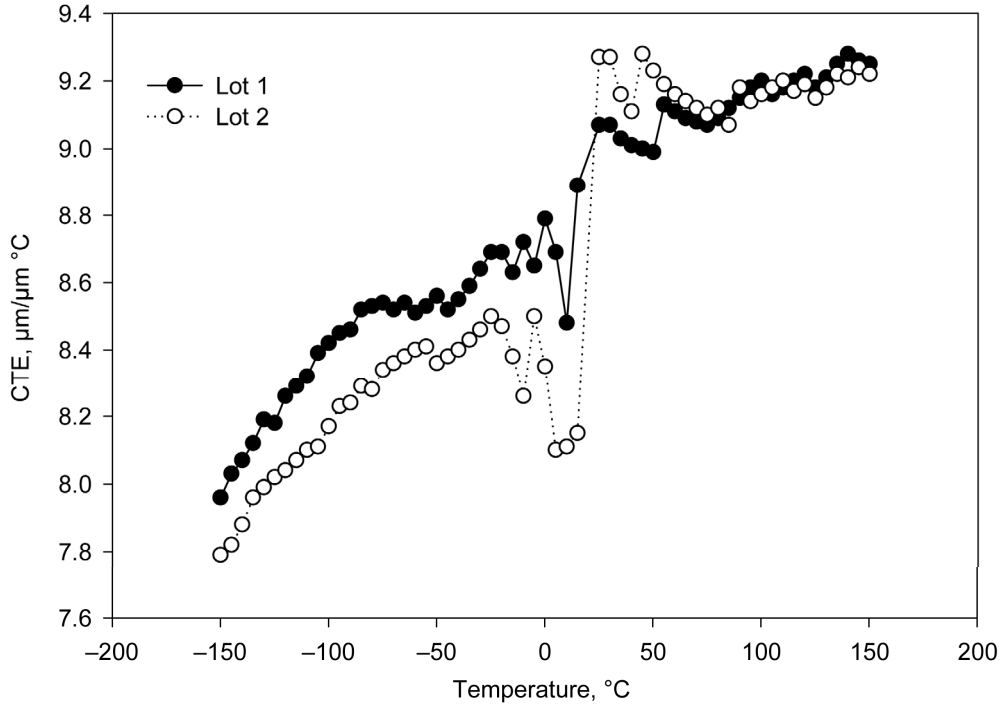

Figure 58.—Mean coefficient of thermal expansion as a function of temperature.